

# Measurement of inclusive jet and dijet cross sections in proton-proton collisions at 7 TeV centre-of-mass energy with the ATLAS detector

The ATLAS Collaboration\*

CERN, 1211 Geneva 23, Switzerland

Received: 29 September 2010 / Revised: 29 October 2010

© CERN for the benefit of the ATLAS collaboration 2011. This article is published with open access at Springerlink.com

**Abstract** Jet cross sections have been measured for the first time in proton-proton collisions at a centre-of-mass energy of 7 TeV using the ATLAS detector. The measurement uses an integrated luminosity of  $17 \text{ nb}^{-1}$  recorded at the Large Hadron Collider. The anti- $k_r$  algorithm is used to identify jets, with two jet resolution parameters,  $R = 0.4$  and  $0.6$ . The dominant uncertainty comes from the jet energy scale, which is determined to within 7% for central jets above 60 GeV transverse momentum. Inclusive single-jet differential cross sections are presented as functions of jet transverse momentum and rapidity. Dijet cross sections are presented as functions of dijet mass and the angular variable  $\chi$ . The results are compared to expectations based on next-to-leading-order QCD, which agree with the data, providing a validation of the theory in a new kinematic regime.

## 1 Introduction

At the Large Hadron Collider (LHC), jet production is the dominant high transverse-momentum ( $p_T$ ) process and as such gives the first glimpse of physics at the TeV scale.

Jet cross sections and properties are key observables in high-energy particle physics. They have been measured at  $e^+e^-$ ,  $ep$ ,  $p\bar{p}$ , and  $pp$  colliders, as well as in  $\gamma p$  and  $\gamma\gamma$  collisions. They have provided precise measurements of the strong coupling constant, have been used to obtain information about the structure of the proton and photon, and have become important tools for understanding the strong interaction and searching for physics beyond the Standard Model (see, for example, [1–19]). Searches for new physics using jets in 7 TeV collisions were recently published [20, 21]. In this paper, we present the first measurements of inclusive single-jet and dijet cross sections using the ATLAS detector. The measurements are performed using a data set taken

early in LHC running, from 30 March to 5 June 2010, corresponding to an integrated luminosity of  $17 \text{ nb}^{-1}$ . The measurement involves a determination of the trigger and reconstruction efficiencies of ATLAS for jets, as well as a first determination of the calorimeter response to jet energy.

The paper is organised as follows. The detector is described in the next section, followed by the definition of the cross sections to be measured (Sect. 3), a discussion of the simulations used in the measurement (Sect. 4) and the theoretical predictions to which the data are compared (Sect. 5). The evaluation of the trigger efficiency is given in Sect. 6. The following two sections (Sects. 7 and 8) describe the evaluation of the main uncertainty in the measurement, coming from the jet energy scale. The event selection and data correction are then described (Sects. 9 and 10), followed by the results and conclusions.

## 2 The ATLAS detector

The ATLAS detector covers almost the entire solid angle around the collision point with layers of tracking detectors, calorimeters, and muon chambers. For the measurements presented in this paper, the inner detector, the calorimeters, and the trigger are of particular importance. These components, and the rest of the detector, are described in detail elsewhere [22].

The inner detector has full coverage in  $\phi$  and covers the pseudorapidity<sup>1</sup> range  $|\eta| < 2.5$ . It consists of a silicon pixel

<sup>1</sup>Pseudorapidity is defined as  $\eta = -\ln(\tan(\theta/2))$ . The ATLAS reference system is a Cartesian right-handed coordinate system, with the nominal collision point at the origin. The anti-clockwise beam direction defines the positive  $z$ -axis, while the positive  $x$ -axis is defined as pointing from the collision point to the centre of the LHC ring and the positive  $y$ -axis points upwards. The azimuthal angle  $\phi$  is measured around the beam axis, and the polar angle  $\theta$  is measured with respect to the  $z$ -axis.

\* e-mail: atlas.secretariat@cern.ch

detector, a silicon microstrip detector, and a transition radiation tracker, all immersed in a 2 T magnetic field. These tracking detectors are used to reconstruct tracks and vertices, including the primary vertex.

High granularity liquid-argon (LAr) electromagnetic sampling calorimeters, with excellent energy and position resolution, cover the pseudorapidity range  $|\eta| < 3.2$  (the barrel covers  $|\eta| < 1.475$  and the two end-caps cover  $1.375 < |\eta| < 3.2$ ). The hadronic calorimetry in the range  $|\eta| < 1.7$  is provided by a scintillating-tile calorimeter, which is separated into a large barrel ( $|\eta| < 1.0$ ) and two smaller extended barrel cylinders, one on either side of the central barrel ( $0.8 < |\eta| < 1.7$ ). In the end-caps ( $|\eta| > 1.5$ ), LAr hadronic calorimeters match the outer  $|\eta|$  limits of the end-cap electromagnetic calorimeters. The LAr forward calorimeters provide both electromagnetic and hadronic energy measurements, and extend the coverage to  $|\eta| < 4.9$ .

The trigger system uses three consecutive trigger levels to select signal and reject background events. The Level-1 (L1) trigger is based on custom-built hardware to process the incoming data with a fixed latency of  $2.5 \mu\text{s}$ . This is the only trigger level used in this analysis. In order to commission the trigger software, the higher level triggers also recorded decisions on events, but these decisions were not applied to reject any data. The events in this analysis were accepted either by the system of minimum-bias trigger scintillators (MBTS) or by the calorimeter trigger.

The MBTS detector [23] consists of 32 scintillator counters that are each 2 cm thick, which are organised into two disks with one on each side of the ATLAS detector. The scintillators are installed on the inner face of the end-cap calorimeter cryostats at  $z = \pm 356$  cm such that the disk surface is perpendicular to the beam direction. This leads to a coverage of  $2.09 < |\eta| < 3.84$ . The MBTS multiplicity is calculated for each side independently, and allows events containing jets to be triggered with high efficiency and negligible bias.

The L1 calorimeter trigger uses coarse detector information to identify the position of interesting physics objects above a given energy threshold. The ATLAS jet trigger is based on the selection of jets according to their transverse energy,  $E_T$ . The L1 jet reconstruction uses so-called jet elements, which are formed from the electromagnetic and hadronic calorimeters with a granularity of  $\Delta\phi \times \Delta\eta = 0.2 \times 0.2$  for  $|\eta| < 3.2$ . The jet finding is based on a sliding window algorithm with steps of one jet element, and the jet  $E_T$  is computed in a window of configurable size around the jet.

Recorded events are fully reconstructed offline, using object-oriented analysis software running on a distributed computing grid.

### 3 Cross section definition

Jets are identified using the anti- $k_t$  jet algorithm [24] implemented in the FASTJET [25, 26] package. This algorithm constructs, for each input object (e.g. a parton, particle or energy cluster)  $i$ , the quantities  $d_{ij}$  and  $d_{iB}$  as follows:

$$d_{ij} = \min(k_{ti}^{-2}, k_{tj}^{-2}) \frac{(\Delta R)_{ij}^2}{R^2}, \quad (1)$$

$$d_{iB} = k_{ti}^{-2}, \quad (2)$$

where

$$(\Delta R)_{ij}^2 = (y_i - y_j)^2 + (\phi_i - \phi_j)^2, \quad (3)$$

$k_{ti}$  is the transverse momentum of object  $i$  with respect to the beam direction,  $\phi_i$  is its azimuthal angle, and  $y_i$  is its rapidity, defined as  $y = \frac{1}{2} \ln[(E + p_z)/(E - p_z)]$ , where  $E$  denotes the energy and  $p_z$  is the component of the momentum along the  $z$ -axis. A list containing all the  $d_{ij}$  and  $d_{iB}$  values is compiled. If the smallest entry is a  $d_{ij}$ , objects  $i$  and  $j$  are combined (their four-vectors are added) and the list is updated. If the smallest entry is a  $d_{iB}$ , this object is considered a complete ‘‘jet’’ and is removed from the list. As defined above,  $d_{ij}$  is a distance measure between two objects, and  $d_{iB}$  is a similar distance between the object and the beam. Thus the variable  $R$  is a resolution parameter which sets the relative distance at which jets are resolved from each other as compared to the beam. In this analysis, two different values for the  $R$  parameter are chosen:  $R = 0.4$  and  $R = 0.6$ ; using two values allows comparison to QCD calculations subject to rather different soft (non-perturbative) QCD corrections. The anti- $k_t$  algorithm is well-motivated since it can be implemented in next-to-leading-order (NLO) perturbative QCD (pQCD) calculations, is infrared-safe to all orders, and produces geometrically well-defined (‘‘cone-like’’) jets.

The jet cross section measurements are corrected for all experimental effects, and so refer to the ideal ‘‘truth’’ final-state of a proton-proton collision (see, for example [27]), where jets are built from stable particles, i.e. those with a proper lifetime longer than 10 ps. This definition includes muons and neutrinos from decaying hadrons.

Inclusive single-jet double-differential cross sections are measured as a function of jet  $p_T$  and  $y$  for all jets in the kinematic region  $p_T > 60$  GeV,  $|y| < 2.8$ . This ensures that jets lie well within the high efficiency plateau region for the triggers used, as described in Sect. 6, and that the jets are in a region where the jet energy scale is well understood, as described in Sect. 7.

The dijet double-differential cross section is measured as a function of the invariant mass of the dijet system,  $m_{12}$ , binned in the maximum rapidity of the two leading (i.e.

highest  $p_T$ ) jets,  $|y|_{\max} = \max(|y_1|, |y_2|)$ . It is also measured as a function of the angular variable

$$\chi = \exp(|y_1 - y_2|) \approx \frac{1 + \cos \theta^*}{1 - \cos \theta^*} \quad (4)$$

binned in the dijet mass  $m_{12}$ . Here the subscripts 1, 2 label the highest and second highest  $p_T$  jet in the event within  $|y| < 2.8$ , respectively, and  $\theta^*$  is the polar scattering angle of the outgoing jets in the dijet centre-of-mass frame. The approximation in the expression is exact for massless jets perfectly balanced in  $p_T$ . The leading jet is required to lie in the  $p_T, |y|$  kinematic region defined above. The subleading jet is required to lie in the same rapidity region and to have  $p_T > 30$  GeV, which ensures that both the jet reconstruction efficiency and purity<sup>2</sup> are above 99% in all bins. This cut is also important to limit misidentification of the subleading jet due to less precise jet energy resolution for  $p_T < 30$  GeV (see Sect. 10). Allowing for some imbalance in the  $p_T$  of the two jets improves the stability of the NLO calculation [28].

The dijet mass is plotted in the allowed rapidity region only above the minimum mass where it is no longer biased by the  $p_T$  and rapidity cuts on the two leading jets. The minimum unbiased mass depends on the  $|y|_{\max}$  bin, which determines the maximum opening angle in rapidity allowed. The biased spectrum below this mass is not measured due to its particular sensitivity to the jet energy scale uncertainty through the jet  $p_T$  cut.

The variable  $\chi$  is plotted up to a maximum of 30, restricting the angular separation in rapidity to  $|y_1 - y_2| < \ln(30)$ . In the rotated coordinate system ( $y^*, y_{\text{boost}}$ ), where  $y^* = 0.5 \cdot (y_1 - y_2)$ , and  $y_{\text{boost}} = 0.5 \cdot (y_1 + y_2)$  is the boost of the dijet system with respect to the laboratory frame, this restricts the acceptance to  $|y^*| < 0.5 \ln(30)$ . An orthogonal acceptance cut  $|y_{\text{boost}}| < 1.1$  is then made on the  $\chi$  distribution in order to reject events in which both jets are boosted into the forward or backward direction. This reduces the sensitivity to parton density function (PDF) uncertainties at low  $x$ , where  $x$  is the fraction of the momentum of the proton carried by the parton participating in the hard scattering, and in turn enhances sensitivity to differences that could arise from deviations from the matrix element predictions of pQCD. The  $\chi$  spectrum is plotted only in mass bins above the minimum unbiased mass.

The kinematic constraints mean that the region of  $x$  probed by these measurements varies in the approximate range  $5 \times 10^{-4} < x < 0.4$  for the inclusive jet measurements, and  $1.4 \times 10^{-2} < x < 0.3$  for the dijet measurements.

<sup>2</sup>The efficiency and purity were determined using Monte Carlo with a requirement that truth and reconstructed jets match to within  $\Delta R = 0.3$ .

## 4 Monte Carlo samples

Samples of simulated jet events in proton-proton collisions at  $\sqrt{s} = 7$  TeV were produced using several Monte Carlo (MC) generators. The PYTHIA 6.421 [29] event generator is used for the baseline comparisons and corrections. It implements leading-order (LO) pQCD matrix elements for  $2 \rightarrow 2$  processes,  $p_T$ -ordered parton showers calculated in a leading-logarithmic approximation, an underlying event<sup>3</sup> simulation using multiple-parton interactions, and uses the Lund string model for hadronisation. For studies of systematic uncertainties, jet samples were produced using the HERWIG 6 [30] generator, which also employs LO pQCD matrix elements, but uses an angle-ordered parton shower model and a cluster hadronisation model. The underlying event for the HERWIG 6 samples is generated using the JIMMY [31] package using multiple-parton interactions. The HERWIG++ [32], ALPGEN [33], and SHERPA [34] programmes were also used for various cross-checks. The samples are QCD  $2 \rightarrow 2$  scattering samples created using the MRST2007LO\* [35, 36] modified leading-order PDFs. The HERWIG 6 and PYTHIA 6 samples use tuned sets of parameters denoted as MC09 [37], unless stated otherwise.

The generated samples are passed through a full simulation [38] of the ATLAS detector and trigger based on GEANT4 [39]. The Quark Gluon String model [40] was used for the fragmentation of the nucleus, and the Bertini cascade model [41] for the description of the interactions of the hadrons in the medium of the nucleus. The parameters used in GEANT4 are described in more detail elsewhere [42]. Test-beam measurements for single pions have shown that these simulation settings best describe the response and resolution in the barrel [43, 44] and end-cap [45, 46] calorimeters.

Finally, the events are reconstructed and selected using the same analysis chain as for the data with the same trigger, event selection, and jet selection criteria.

## 5 Theoretical predictions

Several NLO pQCD calculations are available for jet production in proton-proton collisions. NLOJET++ 4.1.2 [47] was used to calculate the QCD  $2 \rightarrow 2$  scattering process at NLO for comparison with data. JETRAD [48] was used for cross-checks. The CTEQ 6.6 [49] NLO parton densities were used for the central value and uncertainties, and the MSTW 2008 [35], NNPDF 2.0 [50] and HERAPDF 1.0 [51] parton density sets were used as cross-checks. The default

<sup>3</sup>The term underlying event is used to mean particles produced in the same proton-proton collision, but not originating from the primary hard partonic scatter or its products.

renormalisation and factorisation scales ( $\mu_R$  and  $\mu_F$  respectively) were defined to be equal to the  $p_T$  of the leading jet in the event. To estimate the potential impact of higher order terms not included in the calculation,  $\mu_R$  was varied from half to twice the default scale. To estimate the impact of the choice of the scale at which the PDF evolution is separated from the matrix element,  $\mu_F$  was similarly varied. These two scales were varied independently apart from a constraint that the ratio of the two scales be between 1/2 and 2, applied to avoid introducing large logarithms of the ratio of the scales. In addition, the effect of the uncertainty in the strong coupling constant,  $\alpha_s(M_Z)$ , was estimated by calculating the cross section using  $\alpha_s(M_Z)$  values within the uncertainty range, and using PDFs fitted using these values. To efficiently calculate all these uncertainties, the APPLGRID [52] program was used.

The NLO calculations predict partonic cross sections, which are unmeasurable. For comparison with data at the particle level, soft (non-perturbative) corrections must be applied. This was done using leading-logarithmic parton shower Monte Carlo programs, by evaluating the ratio of the cross section before and after hadronisation and underlying event simulation and dividing the NLO theory distributions by this factor. The PYTHIA 6 and HERWIG 6 models described above were used, as well as a variety of alternative tunes of PYTHIA 6 [53, 54] as a cross-check. The central value used is that from the PYTHIA 6 MC09 sample, and the uncertainty is estimated as the maximum spread of the other models investigated. To calculate the particle and parton-level theory distributions, the RIVET [55] package was used. The soft QCD corrections depend significantly on the value of  $R$  (0.4 or 0.6), since wider jets are affected more by the underlying event, whereas narrower jets are more likely to lose particles due to hadronisation. The size of these effects, and their dependence on jet size, increases with decreasing  $p_T$ . The corrections are within 5% of unity over most of the kinematic region, but for  $p_T = 30$  GeV they drop to  $-10\%$  for jets with  $R = 0.4$ , and rise to about 15% for the lowest  $p_T$  jets with  $R = 0.6$ .

## 6 Trigger efficiency

The MBTS\_1 trigger, which requires one MBTS counter over threshold, was operational in the early data-taking period. It was used to trigger approximately 2% of the integrated luminosity of the data sample analysed. It has negligible inefficiency (as measured in randomly triggered events [23]) for the events considered in this analysis, which all contain several charged tracks. As the instantaneous luminosity increased, this trigger had a large prescale factor applied. Consequently subsequent events—comprising approximately 98% of the data sample studied—were triggered by the jet trigger.

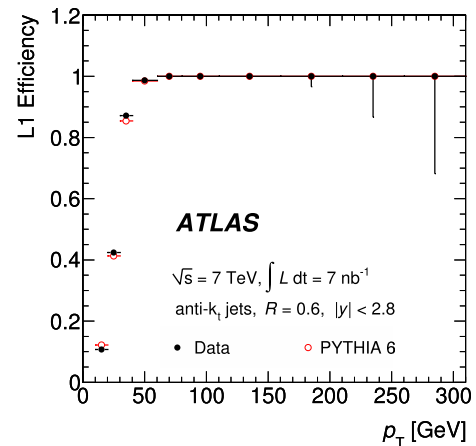
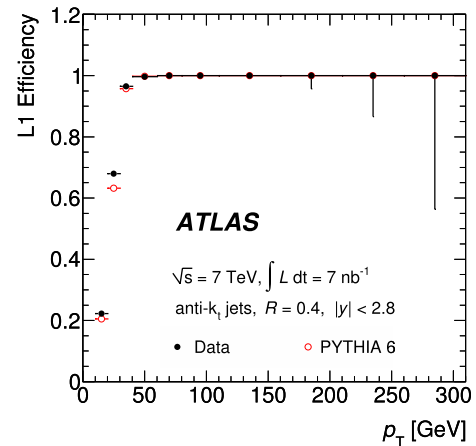


**Fig. 1** Inclusive-jet L1 trigger efficiency as a function of reconstructed jet  $p_T$  for jets identified using the anti- $k_t$  algorithm with (*upper*)  $R = 0.4$  and (*lower*)  $R = 0.6$

The lowest threshold L1 jet trigger, which is used in this analysis, employs a  $0.4 \times 0.4$  window size in  $\eta - \phi$  and requires a jet with  $p_T > 5$  GeV at the electromagnetic scale (see Sect. 7). The inclusive jet trigger efficiency was measured with respect to the MBTS\_1 trigger, which provides an unbiased reference as described above. Its efficiency is shown as a function of the final reconstructed  $p_T$  for single jets ( $R = 0.4$  and  $0.6$ ) in Fig. 1. The efficiency is compared to that predicted from MC simulation, demonstrating that the modelling of the trigger efficiency curve is good. The trigger efficiency for jets with  $p_T > 60$  GeV and  $|y| < 2.8$  is above 99%. All events considered here contain at least one jet in this region.

## 7 Jet energy scale calibration

The input objects to the jet algorithm in the data and in the detector-level simulation are topological energy clusters in the calorimeter. These clusters are seeded by calorimeter cells with energy  $|E_{\text{cell}}| > 4\sigma$  above the noise, where

$\sigma$  is the RMS of the noise. All directly neighbouring cells are added, then neighbours of neighbours are iteratively added for all cells with signals above a secondary threshold  $|E_{\text{cell}}| > 2\sigma$ . Finally the energy in all further immediate neighbours is added. Clusters are split or merged based on the position of local minima and maxima. The cell energies are summed to give the cluster energy, and the clusters are treated as massless. The baseline calibration for these clusters corrects their energy to the electromagnetic (EM) scale. The EM scale is established using test-beam measurements for electrons and muons in the electromagnetic and hadronic calorimeters [56, 57]. It provides a good estimate of the energy deposited in the calorimeter by photons and electrons, but does not correct for detector effects on the calorimeter measurement, including:

- calorimeter non-compensation (the ATLAS calorimeters’ response to hadrons is lower than their response to electrons of the same energy),
- energy losses in inactive regions of the detector (“dead material”),
- particles for which the shower is not totally contained in the calorimeter.

In addition, the baseline calibration does not correct for:

- particles that are clustered into the truth jet but for which the corresponding cluster is not in the reconstructed jet,
- inefficiencies in energy clustering and jet reconstruction.

After a jet is identified, its energy is calibrated to account for these effects, as follows.

The jet energy calibration is carried out in 45 bins of  $\eta$  as a function of  $p_T$  and is based upon MC simulation. The simulation has been validated using test-beam and collision data. Jets with pseudorapidity up to 1.2 are considered central, while jets with  $1.2 < |\eta| < 2.8$  belong to the end-cap region.<sup>4</sup>

The jet energy scale (JES) is obtained using reconstructed calorimeter jets matched to MC particle jets (truth jets, but excluding muons and neutrinos) within a cone of  $\Delta R = 0.3$ . Each jet is required to be isolated, such that there are no other jets with  $p_T > 7$  GeV within a cone of  $2.5 \times R$  around the jet axis. The distribution of the response of the calorimeter jets matched with MC particle-level jets, in bins of particle-level jet  $p_T$  and  $\eta$ , is used to determine the average jet energy response as the mean value of a Gaussian fit.

The correction is obtained by evaluating the transfer function between the energy of the particle-level and EM scale jets, inverting it, and refitting the resulting distribution in bins of reconstructed  $p_T$  to obtain a correction which

<sup>4</sup>The end-cap region includes the transition in the ATLAS detector between the barrel and the end-cap, which needs special treatment because of its geometry and material composition.

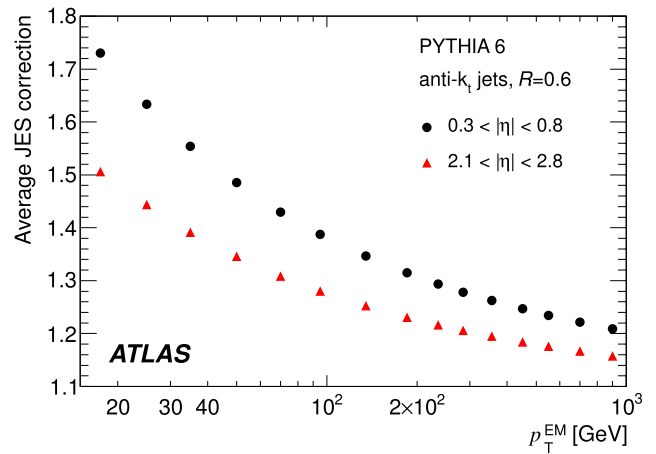


**Fig. 2** Average jet energy scale correction, evaluated using PYTHIA 6, for jets in the central barrel (circles) and end-cap (triangles) regions, shown in EM scale  $p_T$  bins and  $\eta$  regions

can be applied in such bins. The JES correction is shown in Fig. 2 as a function of the jet  $p_T$  at the EM scale, for anti- $k_T$  jets with  $R = 0.6$ , for two of the rapidity bins. The size of the overall correction to the  $p_T$  of the jets is below 75%, and for central jets with  $p_T > 60$  GeV it is below 50%.

### 8 Uncertainty on the jet energy scale

The JES systematic uncertainty is derived combining information from test-beam data, LHC collision data and MC simulations.

The pseudorapidity bins used for the estimate of the jet energy scale uncertainty divide the detector in five  $|\eta|$  regions with boundaries at 0.0, 0.3, 0.8, 1.2, 2.1 and 2.8. This binning closely matches the binning in  $y$  used in the final cross section measurement, which follows the calorimeter geometry.<sup>5</sup>

Only jets with a particle-level jet  $p_T > 20$  GeV, and a measured  $p_T > 10$  GeV after calibration, are considered. No isolation requirement is imposed in the evaluation of the uncertainty in the JES.

#### 8.1 Experimental conditions and calibration method

Several sources of uncertainty related to the detector and experimental conditions have been considered:

- **Material and Geometry** The effect of additional dead material on the jet energy scale has been evaluated with a dedicated geometry model in the simulation, which includes the presence of additional material in front of the barrel calorimeters. Test-beam measurements [58] and

<sup>5</sup>For massless objects, rapidity and pseudorapidity are identical.

comparisons of 900 GeV data to simulations [59] have been used to conservatively estimate the largest possible change in the amount of material. The contribution to the JES uncertainty from this source is around 2% of the jet energy.

- **Noise Thresholds** The uncertainty on the JES due to possible discrepancies between data and the description of the calorimeter electronic noise in the Monte Carlo was evaluated using MC simulation samples reconstructed with signal-to-noise thresholds for topological cluster seeds and cell neighbours modified to be 10% higher and 10% lower than their nominal values. The stability observed in the noise in special monitoring runs where calorimeter signals were studied in the absence of genuine signals, and the comparison of the noise distribution between data and MC simulation, indicate that this 10% variation provides a conservative estimate of the uncertainty on the noise description. The maximum contribution to the JES from this source occurs at low jet  $p_T$  values, where it is around 3% of the jet energy.
- **Beamspot** The jet reconstruction for the JES calibration uses  $(x, y, z) = (0, 0, 0)$  as a reference to calculate the direction and  $p_T$  of the input jet constituents. If the beamspot is shifted with respect to this position, and if this shift is not correctly modelled, the jet  $p_T$  could be biased. The variation of the JES from differences in the beamspot position between data and MC simulation is evaluated using a sample generated with a shifted beamspot of  $(x, y, z) = (1.5, 2.5, -9)$  mm. This shift covers the shift in the current average coordinates observed from data collected by ATLAS from LHC collisions:  $(x, y, z) = (-0.4, 0.62, -1.3)$  mm. The contribution to the JES uncertainty is below 1% of the jet energy.
- **EM scale** For the LAr calorimeters, the EM scale has been measured in test-beam studies, translating into a 3% uncertainty in the scale for in situ operation of the calorimeter [56, 58, 60].

For the tile calorimeter, the EM scale uncertainty of 4% is obtained by comparing test-beam muons, cosmic-ray muons and simulation [57].

These uncertainties are scaled according to the average fraction of jet energy deposited, respectively, in the electromagnetic and hadronic calorimeter as a function of  $p_T$ , and combined to form the uncertainty on the EM scale.

- **Closure test of the JES calibration** Any deviation from unity (non-closure) in  $p_T$  and energy response with respect to the particle jet after the application of the JES corrections to the nominal MC sample implies that the kinematics of the calibrated calorimeter jet are not restored to that of the corresponding particle jets. This can be caused by, for example, the fact that the JES calibration is derived using isolated jets, while the systematic uncertainty is estimated for inclusive jets.

The systematic uncertainty due to the non-closure of the calibration procedure in any given bin is taken as the largest deviation of the response from unity seen either in energy or  $p_T$  in that bin. The contribution to the uncertainty from this source is below 2% of the jet energy.

- **JES uncertainty from dijet balance studies** The JES uncertainty for the higher rapidity regions of the barrel and for the end-cap region is determined using the JES uncertainty for the central barrel region ( $0.3 < |\eta| < 0.8$ ) as a baseline, and adding a contribution from the calibration of the jets with respect to it. This contribution is evaluated by measuring the relative  $p_T$  balance of forward jets in dijet events against reference central jets. The  $\eta$  intercalibration uncertainty is determined for jets where the average  $p_T$  ( $p_T^{\text{avg}}$ ) of the two leading jets is between 50 GeV and 110 GeV and the resulting uncertainty is applied to all  $p_T$ . Since the main sources of uncertainty have been shown to decrease for higher  $p_T$  and energy values than those considered in the jet  $\eta$ -intercalibration study, this leads to a conservative estimate of the uncertainty in the end-cap region for most of the jets considered.

The ratio of the calorimeter response between the reference jet (lying in the region  $0 < |\eta| < 0.8$ ) and the probe jet, as a function of the probe jet  $\eta$ , is shown in Fig. 3 for both data and simulation. Two contributions to the uncertainty are derived—that due to the difference between data and simulation, and that due to the deviation from unity in the data. The combined contribution to the JES uncertainty from these sources is below 3% of the jet energy.

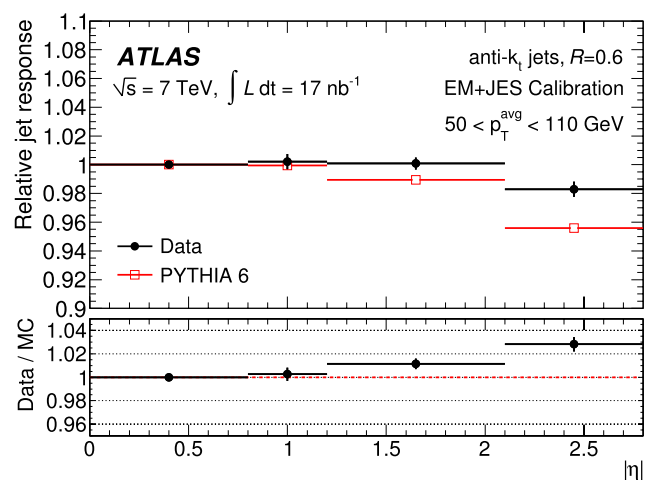


**Fig. 3** Jet  $p_T$  response ( $p_T^{\text{jet,probe}}/p_T^{\text{jet,reference}}$ ) after the EM scale plus JES (EM+JES) calibration against jets in the central reference region ( $0 < |\eta| < 0.8$ ), obtained by exploiting the  $p_T$  balance as a function of  $\eta$  in data and simulation. The lower plot indicates the ratio of the data to the simulation result

## 8.2 Hadronic shower model

The contributions to the JES uncertainty from the hadronic shower model are evaluated using two MC samples, one in which the Bertini nucleon cascade is not used, and one in which the Fritiof model [61] is used instead of the Quark Gluon String fragmentation model.

ATLAS test-beam data for single pions with energies ranging from 2 to 180 GeV have been compared to simulations using these two sets of parameters. The measured mean single pion response was shown to lie between these two descriptions over the whole  $p_T$  range of particles in jets. These models lead to variations of within  $\pm 4\%$  in the calorimeter response to hadrons. This is confirmed by studies in collision data at both 900 GeV and 7 TeV, where the ratio of the energy measured in the calorimeter to the momentum measured in the inner detector is evaluated for single isolated hadrons and compared to the MC simulation.

## 8.3 Event generator models

The contributions to the JES uncertainty from the fragmentation and underlying event models and parameters of the MC event generator are obtained using samples generated with ALPGEN + HERWIG + JIMMY (which has a different matrix element, parton shower, hadronisation model and underlying event compared to the nominal sample), the PYTHIA 6 MC09 tune modified to use Perugia0 fragmentation (which has a different underlying-event model with respect to the nominal sample [53]) and the PYTHIA 6 MC09 tune modified to use parameters tuned to LEP data using the PROFESSOR [54] software.

The observed deviations of the response from unity are smaller than 4%.

## 8.4 Pile-up

In data-taking periods with higher instantaneous luminosity, the effect of pile-up (multiple proton-proton interactions in the same bunch crossing) was small, but not negligible. The size of the effect was estimated by studying the dependence of the average energy density deposited in the calorimeters as a function of the number of reconstructed vertices per event. No correction is applied for this effect, but it is accounted for in the JES uncertainty. For jets with  $20 < p_T < 50$  GeV, the pile-up fractional systematic uncertainty is about 1% in the barrel and 1–2% in the end-caps. For  $p_T > 50$  GeV, the pile-up uncertainty is only significant for  $|\eta| > 2.1$ , and is smaller than 1%.

## 8.5 Effect of decorrelated JES uncertainty on dijet observables

Dijet observables, which in a single event can span the entire range in rapidity, with one jet in the central region and

one in the end-cap region, are sensitive to decorrelations in the JES uncertainty as well as to its value at any given bin in rapidity. Based on results from dijet balance, a 3% positive shift in the jet energy scale was taken at  $|y| = 2.8$  compared to that at  $|y| = 0$ , varying linearly in between and assumed to be symmetric in rapidity. This shift is interpreted as a 3% relative JES uncertainty and is added in quadrature to the other (absolute) sources of uncertainty for the dijet cross sections.

## 8.6 Combination of JES uncertainties

Given that the JES uncertainty is applied to all components of the jet four-momentum, the largest deviation from unity in each bin derived from energy or  $p_T$  response is considered as the contribution to the final JES systematic uncertainty for each specific systematic effect.

All individual uncertainties are added in quadrature except that from the closure test, which is conservatively treated as fully correlated and added linearly.

Figure 4 shows the final fractional JES systematic uncertainty as a function of jet  $p_T$  for an example central  $\eta$  region. Figure 5 shows the forward region, where the contribution from intercalibration with the central region is also included. Both the total systematic uncertainty and the individual contributions are shown, with statistical errors from the fitting procedure if applicable. The pile-up uncertainty (see Sect. 8.4) and the dijet-specific relative uncertainty (see Sect. 8.5) are not included in these plots.

The maximum JES uncertainty in the central region amounts to approximately 9% for jets with  $30 \text{ GeV} < p_T < 60 \text{ GeV}$ , and 7% for  $p_T > 60 \text{ GeV}$ . The uncertainty is increased to up to 10% and 8% respectively for  $30 \text{ GeV} < p_T < 60 \text{ GeV}$  and  $p_T > 60 \text{ GeV}$  in the end-cap region, where the central uncertainty is taken as a baseline and the uncertainty due to the intercalibration is added.

The dominant contributions to the uncertainty come from the hadronic shower model, the EM scale uncertainty, the detector material description, and the noise description.

The same study has been repeated for anti- $k_t$  jets with resolution parameter  $R = 0.4$ , and the estimate of the JES uncertainty is comparable to anti- $k_t$  jets with  $R = 0.6$ , albeit slightly smaller because of the reduced effect of the dead material variation and the change in the noise contribution due to the smaller jet radius. The JES uncertainty for anti- $k_t$  jets with  $R = 0.4$  is between  $\approx 8\%$  (9%) at low jet  $p_T$  and  $\approx 6\%$  (7%) for jets with  $p_T > 60 \text{ GeV}$  in the central (end-cap) region.

The overall JES uncertainty is consistent with the results of detailed comparisons between collision data and simulation.

**Fig. 4** Fractional jet energy scale systematic uncertainty as a function of  $p_T$  for jets in the pseudorapidity region  $0.3 < |\eta| < 0.8$  in the barrel calorimeter. The total systematic uncertainty is shown as well as the individual sources, with statistical errors if applicable

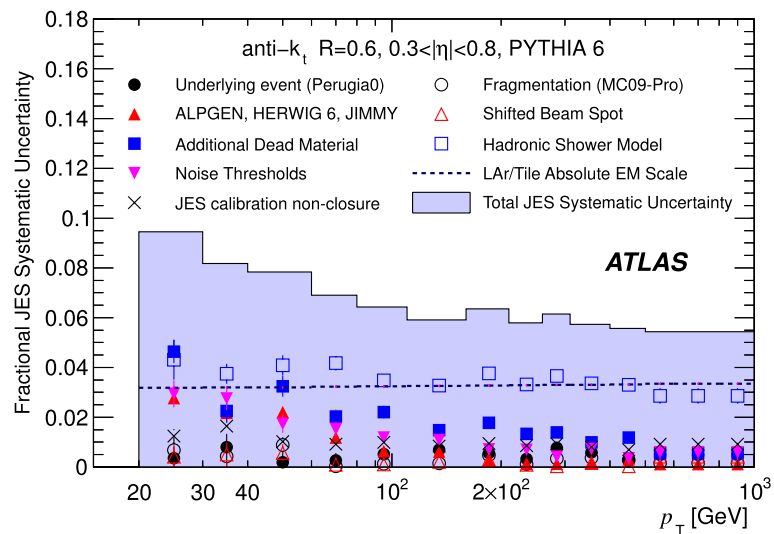
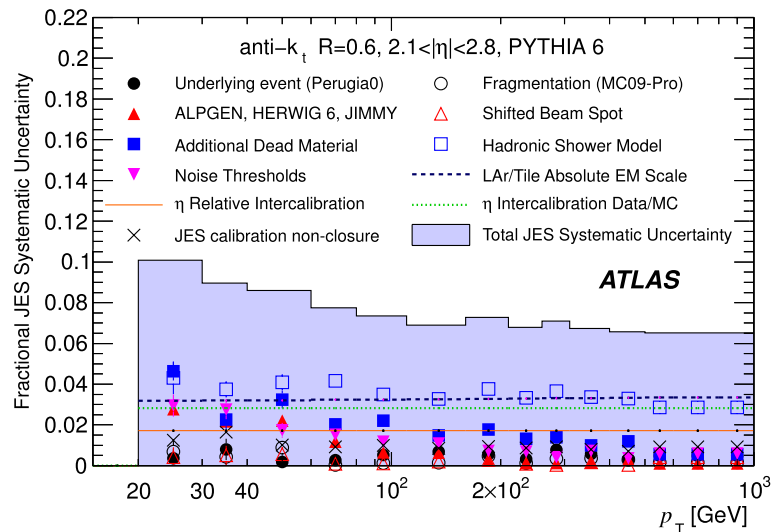


**Fig. 5** Fractional jet energy scale systematic uncertainty as a function of  $p_T$  for jets in the pseudorapidity region  $2.1 < |\eta| < 2.8$ . The JES uncertainty for the end-cap is extrapolated from the barrel uncertainty using dijet balance, with the contributions from the deviation from unity in the data ( $\eta$  relative intercalibration) and the deviation between data and simulation ( $\eta$  intercalibration Data/MC) shown separately. The other individual sources are also shown, with statistical errors if applicable



## 9 Event selection

The jet algorithm is run on energy clusters assuming that the event vertex is at the origin. The jet momenta are then corrected for the beamspot position. After calibration, all events are required to have at least one jet within the kinematic region  $p_T > 60$  GeV,  $|y| < 2.8$ . Additional quality criteria are also applied to ensure that jets are not produced by noisy calorimeter cells or poorly-calibrated detector regions. Events are required to have at least one vertex with at least five reconstructed tracks connected, within 10 cm in  $z$  of the beamspot. Simulated events are reweighted so that the  $z$  vertex distribution agrees with the data. Of the events passing the kinematic selection, 2.6% have more than one vertex. The overall efficiency of these selection cuts, evaluated in simulation using triggered events with truth jets in the kinematic region of the measurement, is above 99%, and has a

small dependence on the kinematic variables. Background contributions from non- $pp$ -collision sources were evaluated using unpaired and empty bunches and found to be negligible.

After this selection, 56 535 (77 716) events remain, for  $R = 0.4$  (0.6), with at least one jet passing the inclusive jet selection. Of these, 45 621 (65 739) events also pass the dijet selection.

## 10 Data correction

The correction for trigger and detector efficiencies and resolutions, other than the energy scale correction already applied, is performed in a single step using a bin-by-bin unfolding method evaluated using the MC samples. For each measured distribution, the corresponding MC cross section



using truth jets (including muons and neutrinos) is evaluated in the relevant bins, along with the equivalent distributions after the detector simulation and analysis cuts. The ratio of the true to the simulated distributions provides a correction factor which is then applied to the data. PYTHIA 6 is used for the central correction. The uncertainty is estimated from the spread of the correction for the different generators, and also from artificially changing the shape of the simulated distributions by reweighting the MC samples within reasonable limits to account for possible biases caused by the input distribution.

This procedure is justified by the good modelling of the trigger efficiencies (Fig. 1) and the fact that the  $p_T$  and  $y$  distributions of the jets are reasonably well described by the simulation [62]. It is also important that the energy flow around the jet core is well understood, both as a validation of the QCD description contained in the event generators and as a cross check of the calibration studies previously discussed, most of which are sensitive to the distribution of energy amongst particles, and within different angular regions, within the jet. The energy and momentum flow within jets can be expressed in terms of the differential jet shape, defined as the fraction,  $\rho(r) = p_T^r/p_T^R$ , where  $p_T^R$  is the transverse momentum within a radius  $R$  of the jet centre, and  $p_T^r$  is the transverse momentum contained within a ring of thickness  $\Delta r = 0.1$  at a radius  $r = \sqrt{(\Delta y)^2 + (\Delta\phi)^2}$  around the jet centre, divided by  $\Delta r$ . The jet shapes evaluated (without any correction for detector effects) using energy clusters and tracks are shown separately in Fig. 6 for anti- $k_t$  jets with  $R = 0.6$ . The jets simulated by PYTHIA 6 are slightly narrower than the jets in the data, while the HERWIG 6 + JIMMY and HERWIG++ simulations provide a somewhat better description. Overall the distribution of energy within the jets is reasonably well simulated. A similar level of agreement has been demonstrated for  $R = 0.4$  jets. This gives further confidence in the calibrations and corrections applied.

The resolutions in  $y$ ,  $p_T$ , dijet mass  $m_{12}$ , and dijet  $\chi$  for anti- $k_t$  jets with  $R = 0.6$  within  $|y| < 2.8$ , as obtained using PYTHIA 6, are shown in Fig. 7. The present JES calibration procedure applies an average correction to restore the jet response and does not attempt to optimise the jet energy resolution, which can be improved with more sophisticated calibration techniques. From dijet balance and  $E/p$  studies of single hadrons, the  $p_T$  resolution has been verified to within a fractional uncertainty of  $\approx 14\%$ , though at a lower  $p_T$  than most of the jets considered here. The effect of varying the nominal  $p_T$  resolution by up to 15% of its nominal value is included in the systematic uncertainty on the unfolding correction factors. The uncertainties due to the jet energy scale are also propagated to the final cross section through this unfolding procedure, by applying variations to

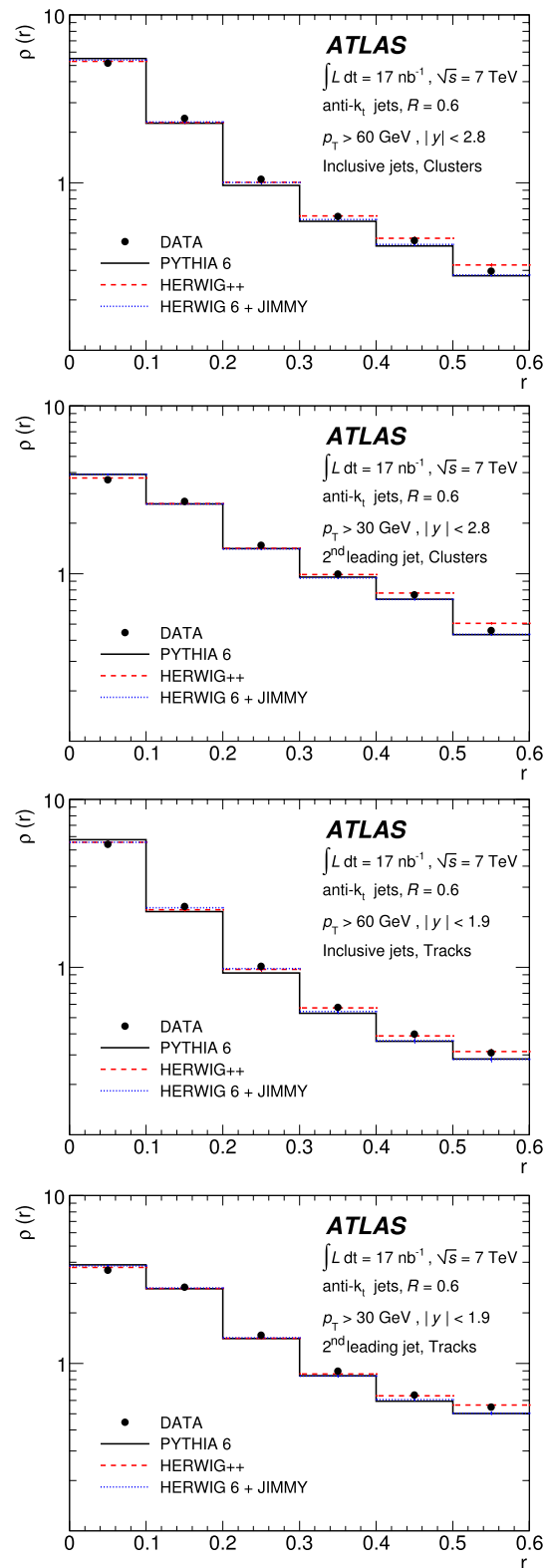


**Fig. 6** The uncorrected jet shape measured using energy clusters (*first two plots*) and tracks (*third and fourth plots*) for anti- $k_t$  jets with  $R = 0.6$ , compared to simulation, as a function of the radial distance to the jet axis,  $r$ . The *first and third figures* show the jet shapes for all jets with  $p_T > 60$  GeV, and the *second and fourth* show the shape for the second highest  $p_T$  jet in dijet events

**Fig. 7** The upper two plots show the absolute (fractional) resolution and bias in jet  $y$  ( $p_T$ ) as a function of true  $p_T$ . The bottom two plots show the fractional resolution and bias in dijet mass  $m_{12}$  and angular variable  $\chi$  as a function of truth  $m_{12}$  computed from the two leading truth jets. These are shown for all jets identified using the anti- $k_t$  algorithm with  $R = 0.6$  in events passing the final kinematic selection, as predicted by PYTHIA 6. The error bar indicates the resolution and the central value indicates the bias

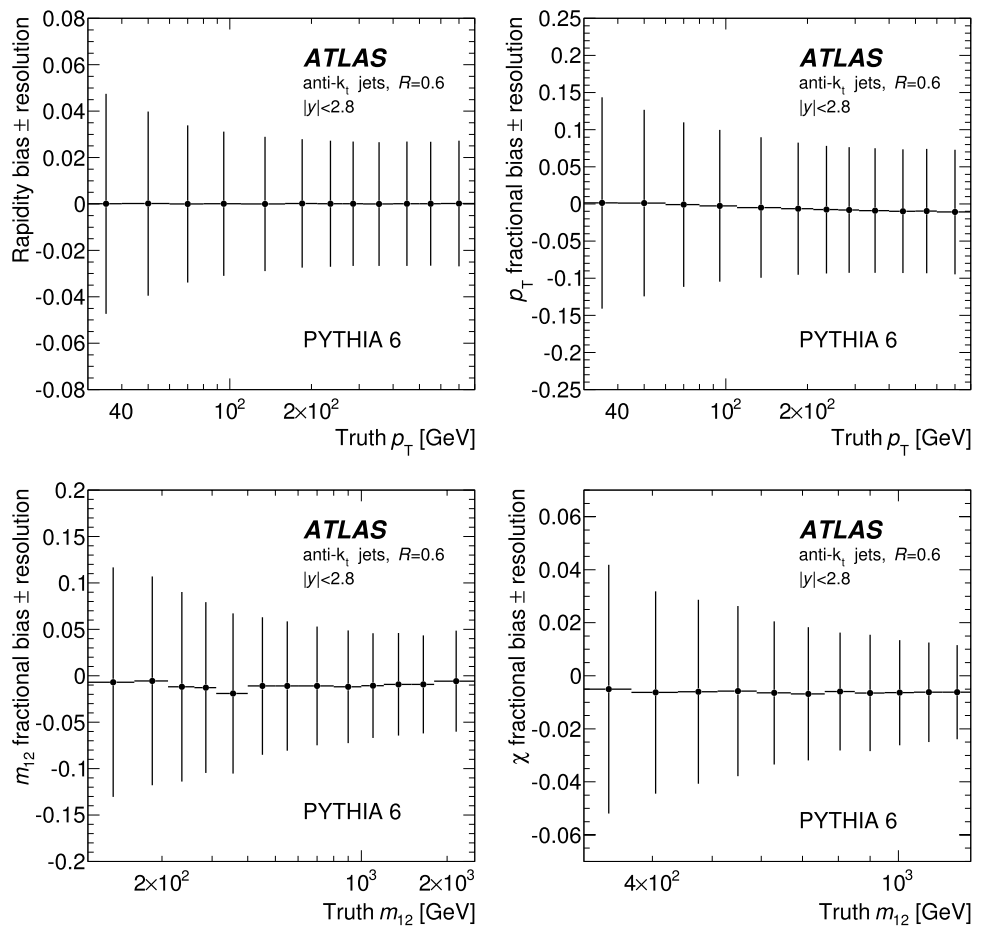
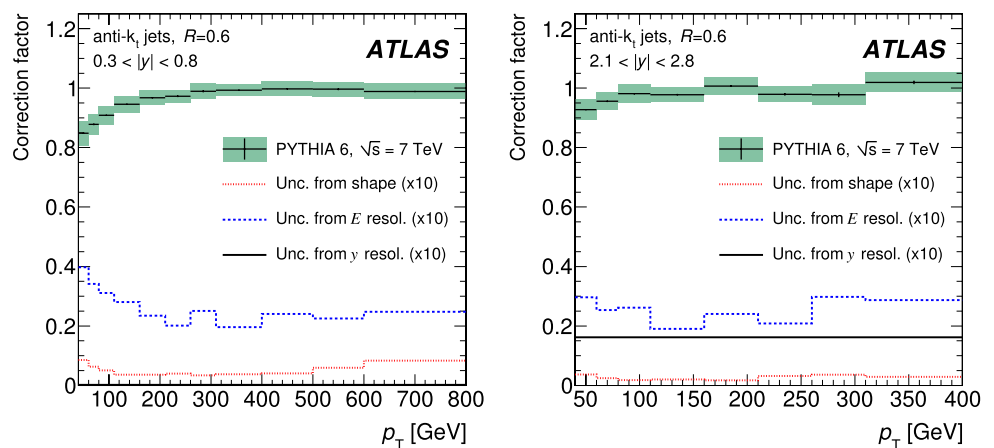


**Fig. 8** Correction factors for the inclusive jet  $p_T$  spectrum in the rapidity bins  $0.3 < |y| < 0.8$  (left) and  $2.1 < |y| < 2.8$  (right), along with systematic uncertainties due to uncertainties in the jet  $p_T$  spectrum shape, jet energy resolution, and jet angular resolution. The band on the correction factor indicates the total systematic uncertainty on the correction



simulated samples. A fit is used to reduce statistical fluctuations in the systematic uncertainties from the jet energy scale for the dijet mass spectrum.

The overall correction factor for the  $p_T$  spectrum is below 20% throughout the kinematic region, and below 10% for central jets with  $p_T > 60$  GeV. As an example, the correction factors for the  $p_T$  spectrum with  $R = 0.6$  are shown along with their systematic uncertainties in Fig. 8 for two

rapidity regions. For the dijet mass spectrum, the correction factors are generally within 15% while for  $\chi$  they are less than 5%.

The integrated luminosities are calculated during runs<sup>6</sup> by measuring interaction rates using several ATLAS devices

<sup>6</sup>An ATLAS run is a period of continuous data-taking during an LHC proton fill.

at small angles to the beam direction, with the absolute calibration obtained from van der Meer scans. The uncertainty in the luminosity is estimated to be 11% [63].

The final systematic uncertainty in the cross section measurements is dominated by the jet energy scale uncertainty.

## 11 Results and discussion

The cross sections from the parton-shower MC generators considered here are not reliable, since these calculations are performed at leading-order. However, many important kinematic terms are included in these calculations, and, unlike the NLO pQCD calculations, the predictions are made at the particle level. A comparison of the shapes of the distributions is therefore valuable. The expectations for the corrected  $p_T$  and  $\chi$  distributions from two different PYTHIA 6 parameter tunes, as well as for HERWIG 6 + JIMMY programs are compared to the data in Figs. 9–12. The normalisation of the simulation is to the inclusive jet cross section separately for each  $R$  value, and requires the factors shown in the legend.<sup>7</sup> In general the simulations agree with the shapes of the data distributions.

The differential inclusive jet cross section in 7 TeV proton-proton collisions is shown in Figs. 13 and 14, as a function of jet  $p_T$ , for anti- $k_t$  jets with  $R = 0.4$  and  $R = 0.6$  respectively. The cross section extends from  $p_T = 60$  GeV up to around  $p_T = 600$  GeV, and falls by more than four orders of magnitude over this range. The data are compared to NLO pQCD calculations corrected for non-perturbative effects. For both  $R = 0.4$  and  $R = 0.6$ , data and theory are consistent.

Figures 15 and 16 show the double-differential cross section as a function of jet  $p_T$  in several different regions of rapidity. Tables 1–3 and 4–6 detail the same data. A selection of the same cross sections expressed as a function of rapidity in different  $p_T$  ranges is shown in Figs. 17 and 18. In Figs. 19 and 20 the ratio of the measurement to the theoretical prediction is shown for the double-differential distribution in jet  $p_T$  for  $R = 0.4$  and  $R = 0.6$  respectively. The data are again compared to NLO pQCD predictions to which soft corrections have been applied, where the predictions are also given in the tables. In all regions, the theory is consistent with the data.

In Figs. 21 and 23, the double-differential dijet cross section is shown as a function of the dijet mass, for different bins in  $|y|_{\max}$ . The cross section falls rapidly with mass, and extends up to masses of nearly 2 TeV. Figures 22 and 24 show the cross section as a function of the dijet angular variable  $\chi$  for different ranges of the dijet mass  $m_{12}$ . The data

are compared to NLO pQCD calculations corrected for non-perturbative effects. The theory is consistent with the data. The dijet mass measurements and the theory predictions are also given in Tables 7–11 and 12–16 for  $R = 0.4$  and  $R = 0.6$  respectively. Those for  $\chi$  are given in Tables 17–19 and 20–22.

In Figs. 25 and 26 the ratio of the measurement to the theoretical prediction is shown for the double-differential dijet cross sections for  $R = 0.4$  and  $R = 0.6$  respectively. The data are again compared to NLO pQCD predictions to which soft corrections have been applied, also included in the tables. In all regions, the theory is consistent with the data.

## 12 Conclusion

Inclusive and dijet cross sections have been measured for the first time in proton-proton collisions with the ATLAS detector, at a centre-of-mass energy of 7 TeV, using an integrated luminosity of  $17 \text{ nb}^{-1}$ .

The cross sections have been measured with the anti- $k_t$  algorithm using two different  $R$  parameters, with different sensitivity to soft QCD corrections. This is the first cross section measurement in hadron-hadron collisions using this jet algorithm.

The cross sections extend into previously unmeasured kinematic regimes. For inclusive jets, the double-differential cross section has been measured for jets with  $|y| < 2.8$  and  $p_T > 60$  GeV. The  $p_T$  distribution extends up to 600 GeV. For dijet events, containing a jet with  $p_T > 30$  GeV in the same rapidity region, the cross section has been measured as a function of the dijet mass and of the angular variable  $\chi$ . The dijet mass distribution extends up to nearly 2 TeV.

The dominant systematic uncertainty in these measurements comes from the jet energy response of the calorimeter. This scale uncertainty has been determined to be below 10% over the whole kinematic range of these measurements, and to be below 7% for central jets with  $p_T > 60$  GeV, leading to a systematic uncertainty in the cross sections of around 40%.

The measurements use only  $17 \text{ nb}^{-1}$  of integrated luminosity, but the statistical errors are not the dominant contribution to the uncertainty below around 300 GeV in transverse momentum. Data already recorded by ATLAS will extend the reach of subsequent measurements and their precision at high transverse momenta.

Leading-logarithmic parton-shower MC generators provide a reasonable description of the energy flow around the jets, and of the shapes of the measured distributions.

The differential cross sections have been compared to NLO pQCD calculations corrected for non-perturbative effects. The inclusive jet measurements are sensitive to the combination of the QCD matrix element and parton densities within the proton, evolved from determinations made using measurements from previous experiments at lower en-

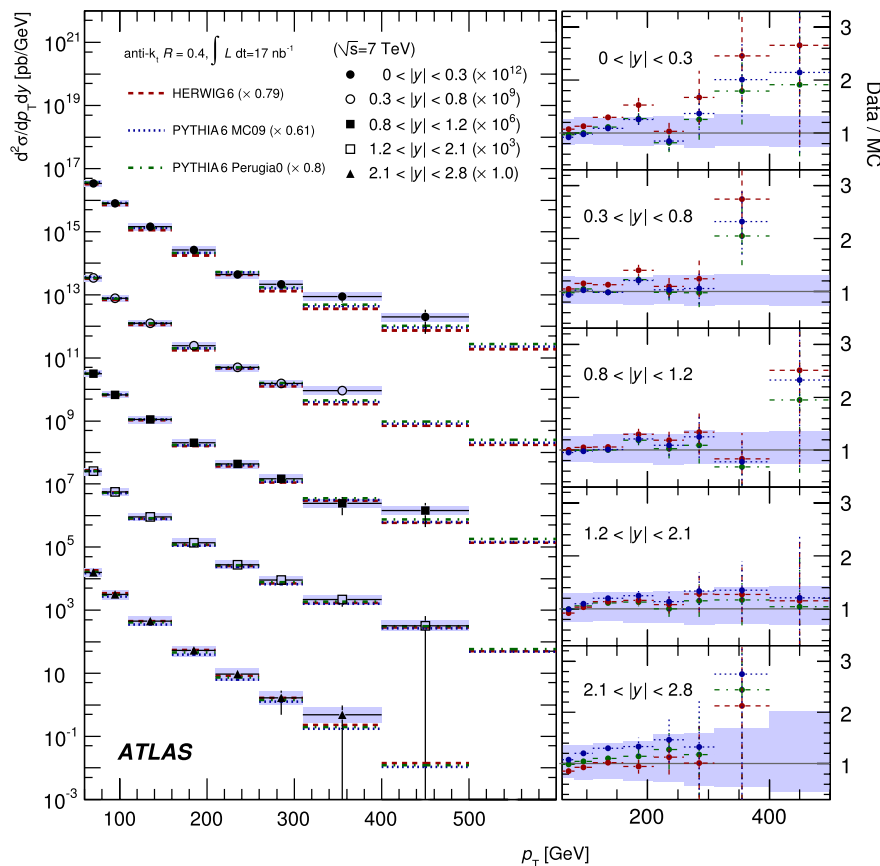
<sup>7</sup>If the  $R = 0.4$  and  $R = 0.6$  measurements are fitted simultaneously, the factors are 0.91, 0.92 and 0.69 for HERWIG + JIMMY, PYTHIA 6 Perugia0 tune and PYTHIA 6 MC09 respectively.

ergy scales. The dijet measurements have been made in a region where the sensitivity to the parton distributions is reduced, and thus primarily test the structure of the QCD matrix element. The comparison is made for two different  $R$  parameters, showing that the level of agreement is robust under different soft corrections, as well as under the evolution of the perturbative cross section with  $R$ . For both inclusive and dijet measurements, the theory agrees well with the data, validating this perturbative QCD approach in a new kinematic regime.

**Acknowledgements** We deeply thank everybody at CERN involved in operating the LHC in such a superb way during this initial high-energy data-taking period. We acknowledge equally warmly all the technical and administrative staff in the collaborating institutions without whom ATLAS could not be operated so efficiently.

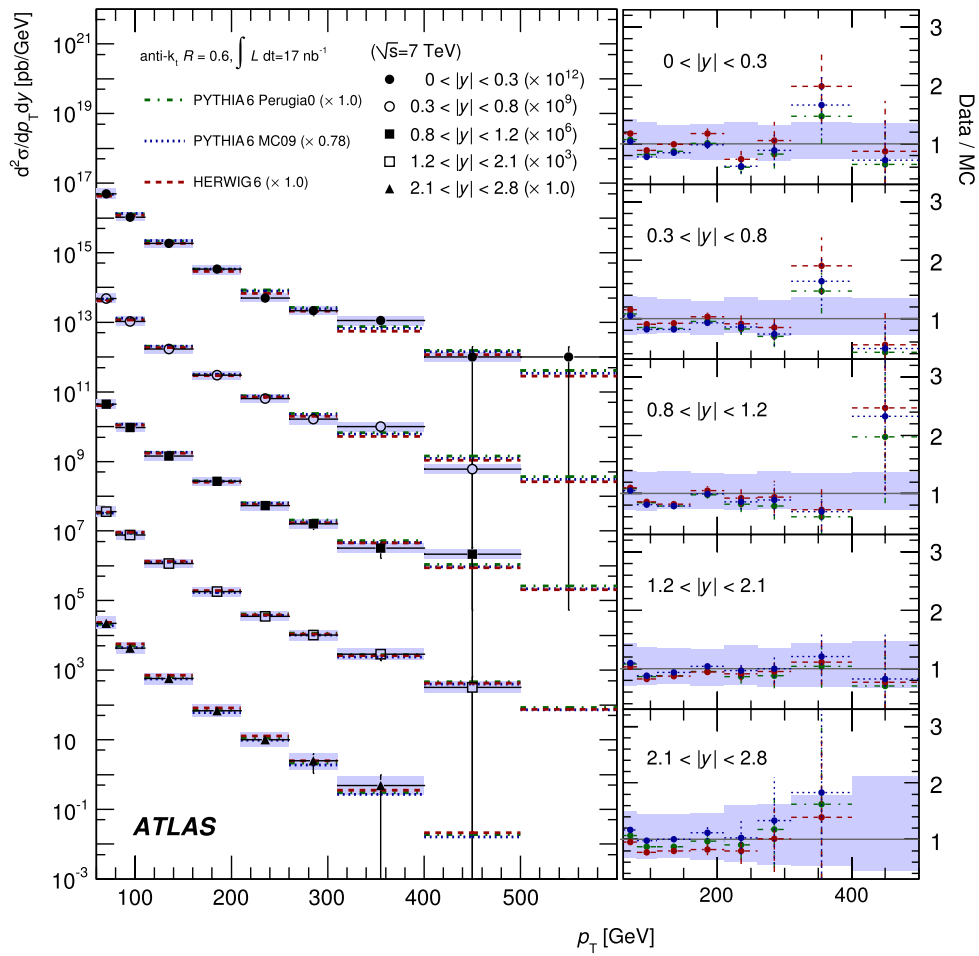
We acknowledge the support of ANPCyT, Argentina; Yerevan Physics Institute, Armenia; ARC and DEST, Australia; Bundesministerium für Wissenschaft und Forschung, Austria; National Academy of Sciences of Azerbaijan; State Committee on Science & Technologies of the Republic of Belarus; CNPq and FINEP, Brazil; NSERC, NRC, and CFI, Canada; CERN; CONICYT, Chile; NSFC, China; COL-

CIENCIAS, Colombia; Ministry of Education, Youth and Sports of the Czech Republic, Ministry of Industry and Trade of the Czech Republic, and Committee for Collaboration of the Czech Republic with CERN; DNRF, DNSRC and the Lundbeck Foundation, Denmark; European Commission, through the ARTEMIS Research Training Network; IN2P3-CNRS and CEA-DSM/IRFU, France; Georgian Academy of Sciences; BMBF, DFG, HGF and MPG, Germany; Ministry of Education and Religion, through the EPEAEK program PYTHAGORAS II and GSRT, Greece; ISF, MINERVA, GIF, DIP, and Benoziyo Center, Israel; INFN, Italy; MEXT, Japan; CNRST, Morocco; FOM and NWO, Netherlands; The Research Council of Norway; Ministry of Science and Higher Education, Poland; GRICES and FCT, Portugal; Ministry of Education and Research, Romania; Ministry of Education and Science of the Russian Federation and State Atomic Energy Corporation ROSATOM; JINR; Ministry of Science, Serbia; Department of International Science and Technology Cooperation, Ministry of Education of the Slovak Republic; Slovenian Research Agency, Ministry of Higher Education, Science and Technology, Slovenia; Ministerio de Educación y Ciencia, Spain; The Swedish Research Council, The Knut and Alice Wallenberg Foundation, Sweden; State Secretariat for Education and Science, Swiss National Science Foundation, and Cantons of Bern & Geneva, Switzerland; National Science Council, Taiwan; TAEK, Turkey; The STFC, the Royal Society and The Leverhulme Trust, United Kingdom; DOE and NSF, United States of America.



**Fig. 9** Inclusive jet double-differential cross section as a function of  $p_T$ , for different bins of rapidity  $|y|$ . The results are shown for jets identified using the anti- $k_r$  algorithm with  $R = 0.4$ . The data are compared to leading-logarithmic parton-shower MC simulations, normalised to the measured cross section by the factors shown in the legend, fixed to give the best normalisation to the inclusive jet measurements. The

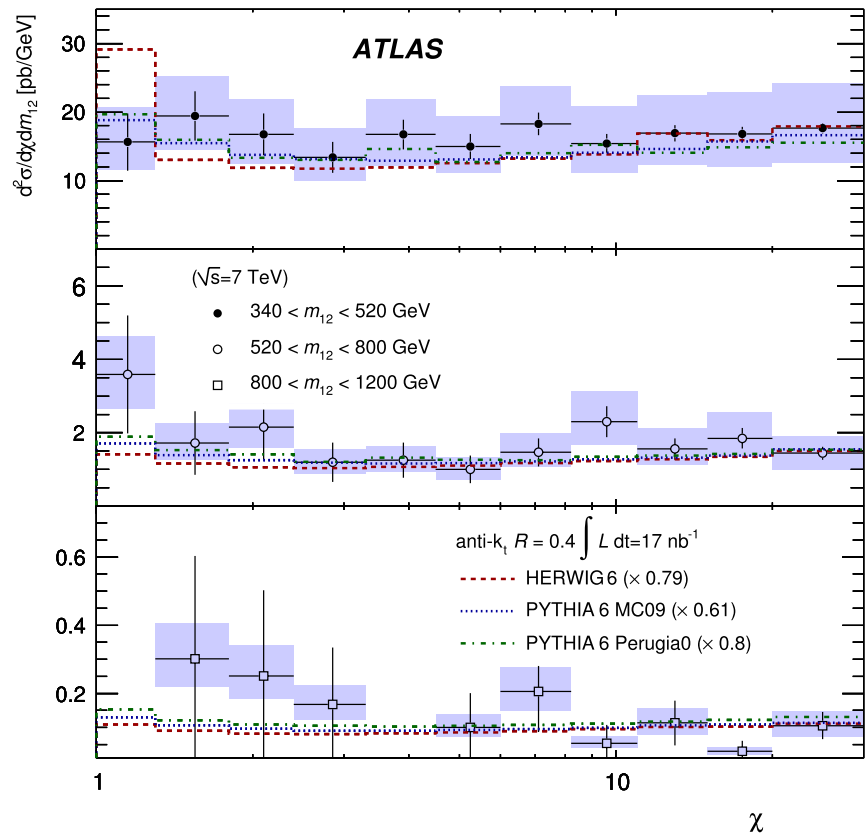
bands indicate the total systematic uncertainty on the data. The error bars indicate the statistical uncertainty, which is calculated as  $1/\sqrt{N}$ , where  $N$  is the number of entries in a given bin. The *insets along the right-hand side* show the ratio of the data to the various MC simulations



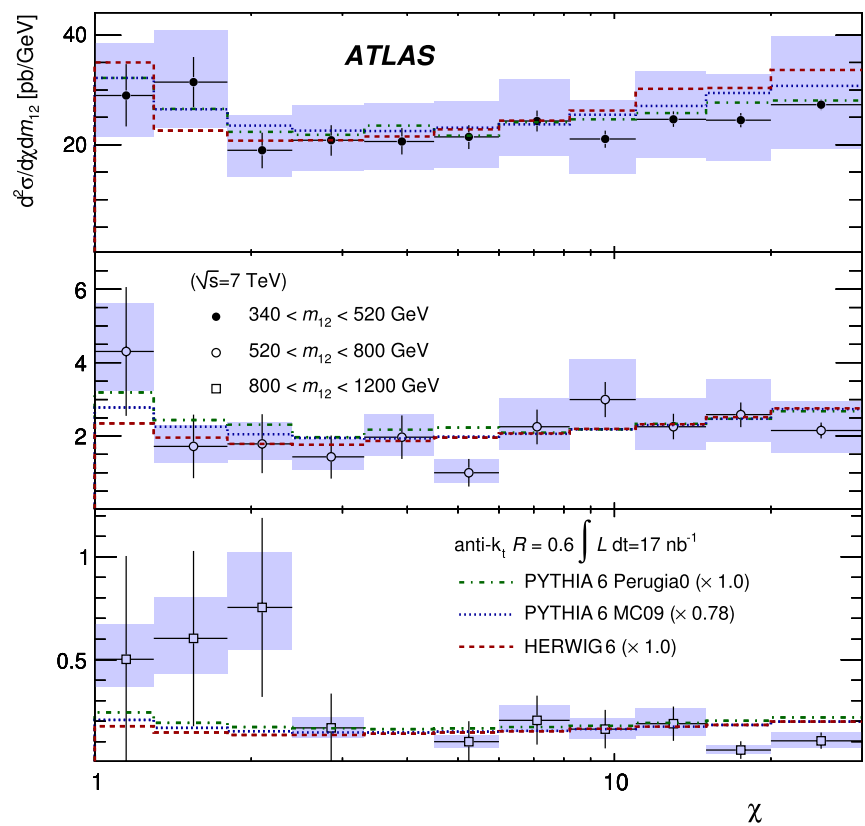
**Fig. 10** Inclusive jet double-differential cross section as a function of  $p_T$ , for different bins of rapidity  $|y|$ . The results are shown for jets identified using the anti- $k_r$  algorithm with  $R = 0.6$ . The data are compared to leading-logarithmic parton-shower MC simulations, normalised to the measured cross section by the factors shown in the legend, fixed to give the best normalisation to the inclusive jet measurements. The

bands indicate the total systematic uncertainty on the data. The error bars indicate the statistical uncertainty, which is calculated as  $1/\sqrt{N}$ , where  $N$  is the number of entries in a given bin. The insets along the right-hand side show the ratio of the data to the various MC simulations

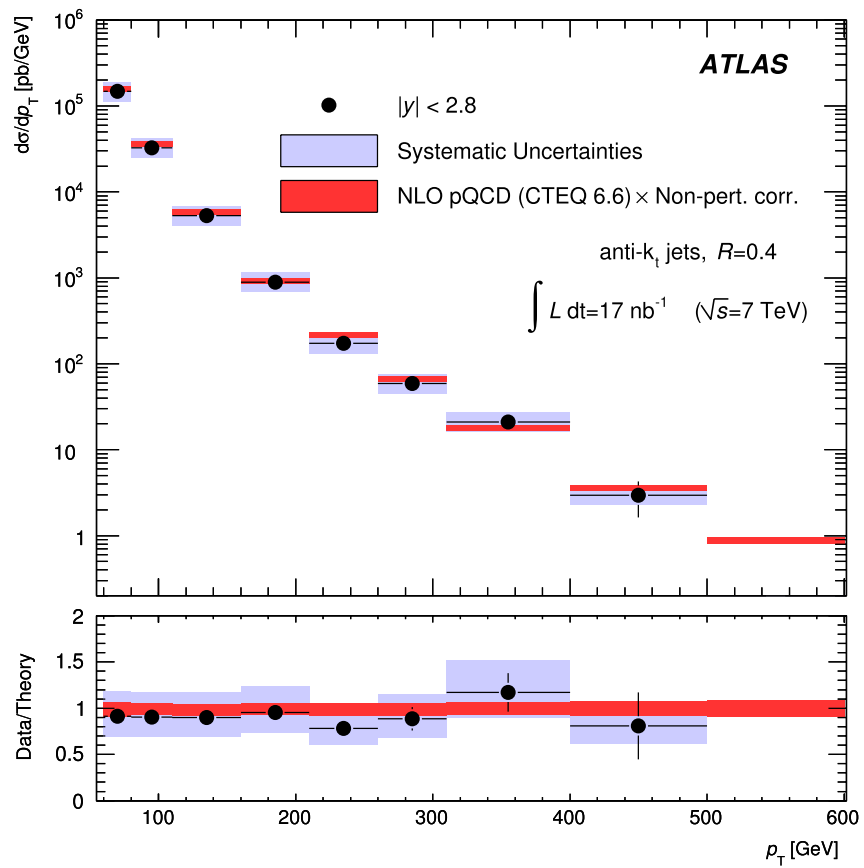
**Fig. 11** Dijet double-differential cross section as a function of angular variable  $\chi$  in different regions of dijet mass  $m_{12}$ , for jets identified using the anti- $k_r$  algorithm with  $R = 0.4$ . The data are compared to leading-logarithmic parton-shower MC simulations, normalised to the measured cross section by the factors shown in the legend, fixed to give the best normalisation to the inclusive jet measurements. The bands indicate the total systematic uncertainty on the data. The error bars indicate the statistical uncertainty, which is calculated as  $1/\sqrt{N}$ , where  $N$  is the number of entries in a given bin



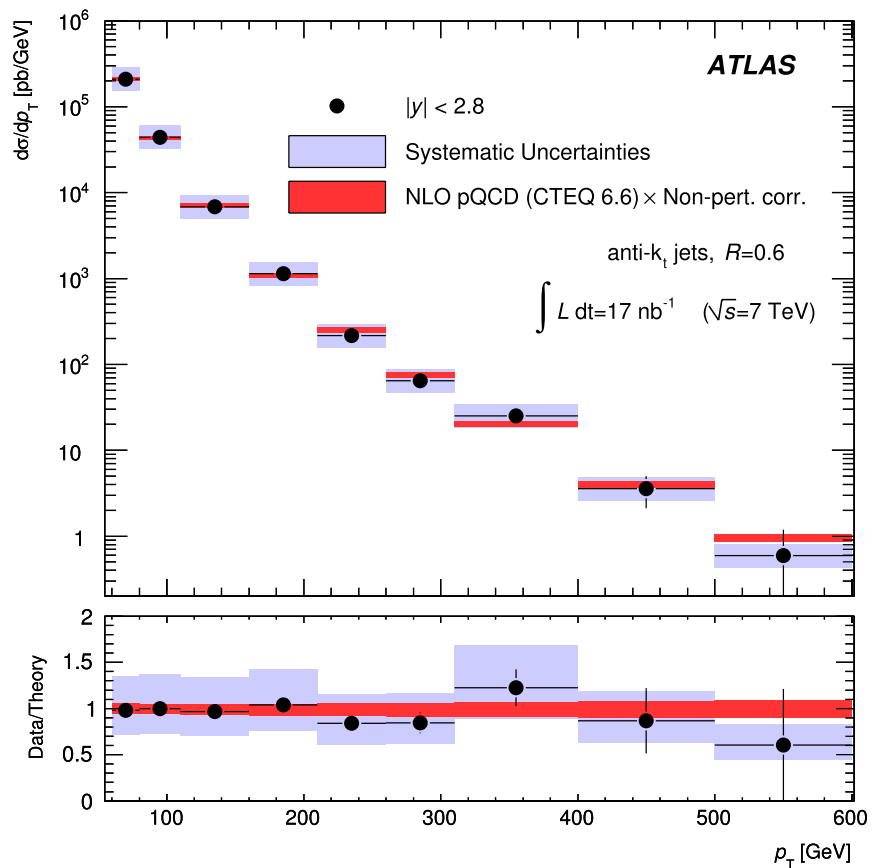
**Fig. 12** Dijet double-differential cross section as a function of angular variable  $\chi$  in different regions of dijet mass  $m_{12}$ , for jets identified using the anti- $k_r$  algorithm with  $R = 0.6$ . The data are compared to leading-logarithmic parton-shower MC simulations, normalised to the measured cross section by the factors shown in the legend, fixed to give the best normalisation to the inclusive jet measurements. The bands indicate the total systematic uncertainty on the data. The error bars indicate the statistical uncertainty, which is calculated as  $1/\sqrt{N}$ , where  $N$  is the number of entries in a given bin



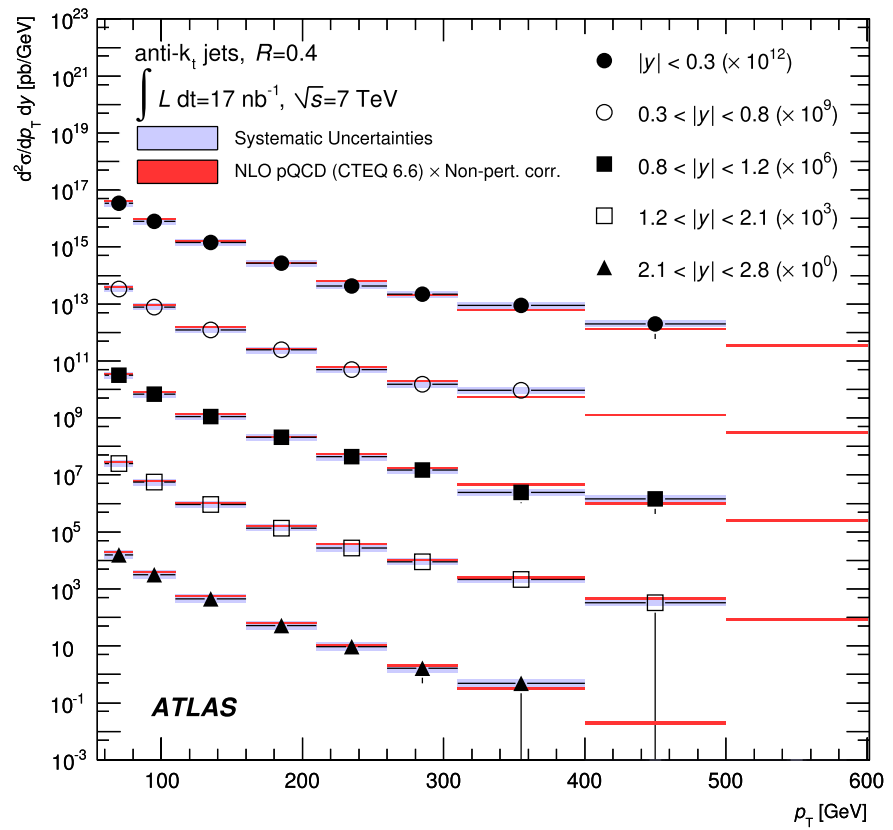
**Fig. 13** Inclusive jet differential cross section as a function of jet  $p_T$  integrated over the full region  $|y| < 2.8$  for jets identified using the anti- $k_t$  algorithm with  $R = 0.4$ . The data are compared to NLO pQCD calculations to which soft QCD corrections have been applied. The error bars indicate the statistical uncertainty on the measurement, and the shaded bands indicate the quadratic sum of the systematic uncertainties, dominated by the jet energy scale uncertainty. The statistical uncertainty is calculated as  $1/\sqrt{N}$ , where  $N$  is the number of entries in a given bin. There is an additional overall uncertainty of 11% due to the luminosity measurement that is not shown. The theory uncertainty shown is the quadratic sum of uncertainties from the choice of renormalisation and factorisation scales, parton distribution functions,  $\alpha_s(M_Z)$ , and the modelling of soft QCD effects, as described in the text



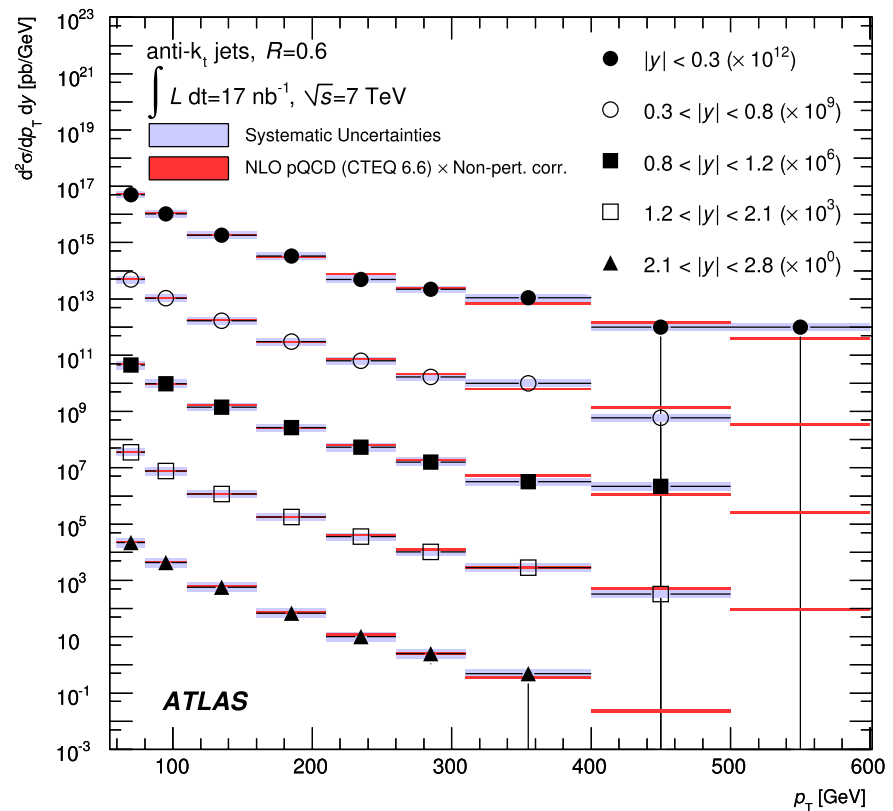
**Fig. 14** Inclusive jet differential cross section as a function of jet  $p_T$  integrated over the full region  $|y| < 2.8$  for jets identified using the anti- $k_t$  algorithm with  $R = 0.6$ . The data are compared to NLO pQCD calculations to which soft QCD corrections have been applied. The uncertainties on the data and theory are shown as described in Fig. 13



**Fig. 15** Inclusive jet double-differential cross section as a function of jet  $p_T$  in different regions of  $|y|$  for jets identified using the anti- $k_t$  algorithm with  $R = 0.4$ . The data are compared to NLO pQCD calculations to which soft QCD corrections have been applied. The uncertainties on the data and theory are shown as described in Fig. 13

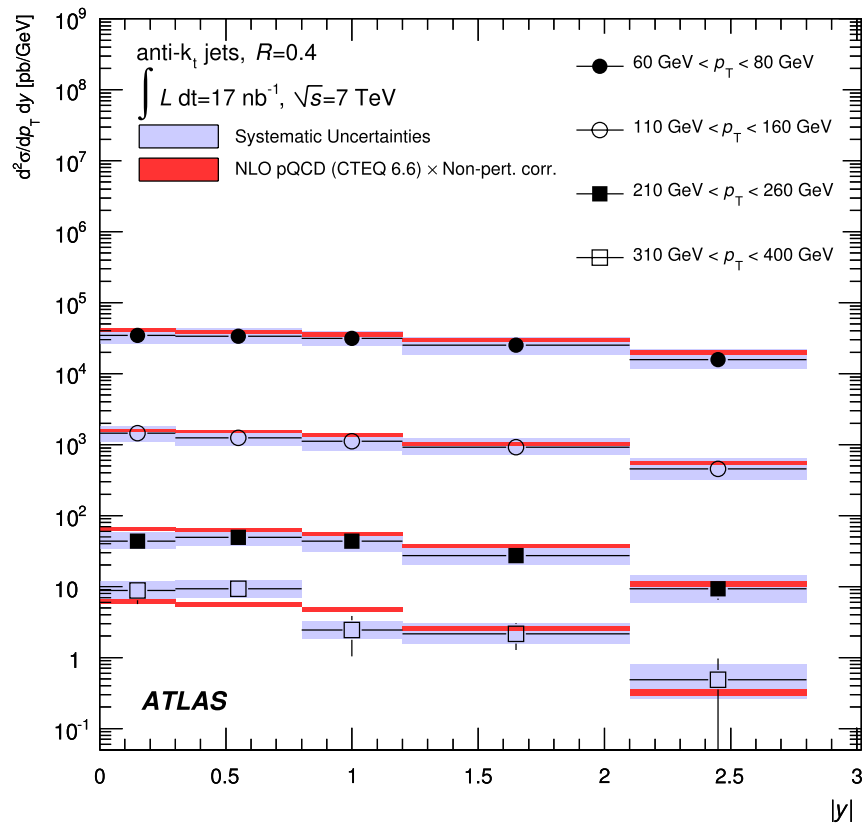


**Fig. 16** Inclusive jet double-differential cross section as a function of jet  $p_T$  in different regions of  $|y|$  for jets identified using the anti- $k_t$  algorithm with  $R = 0.6$ . The data are compared to NLO pQCD calculations to which soft QCD corrections have been applied. The uncertainties on the data and theory are shown as described in Fig. 13

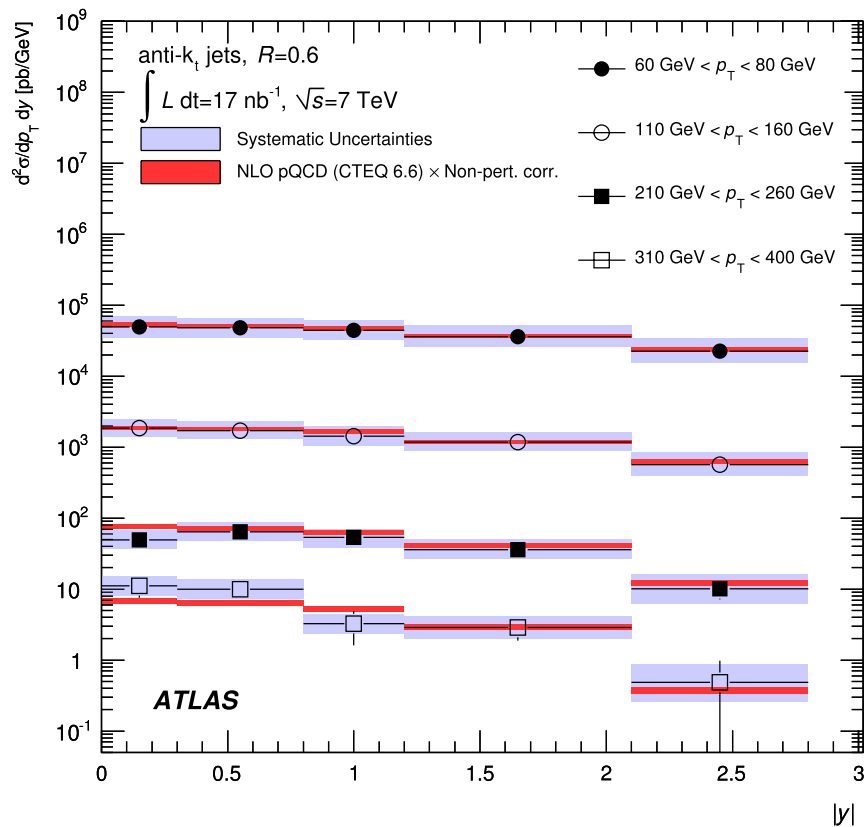




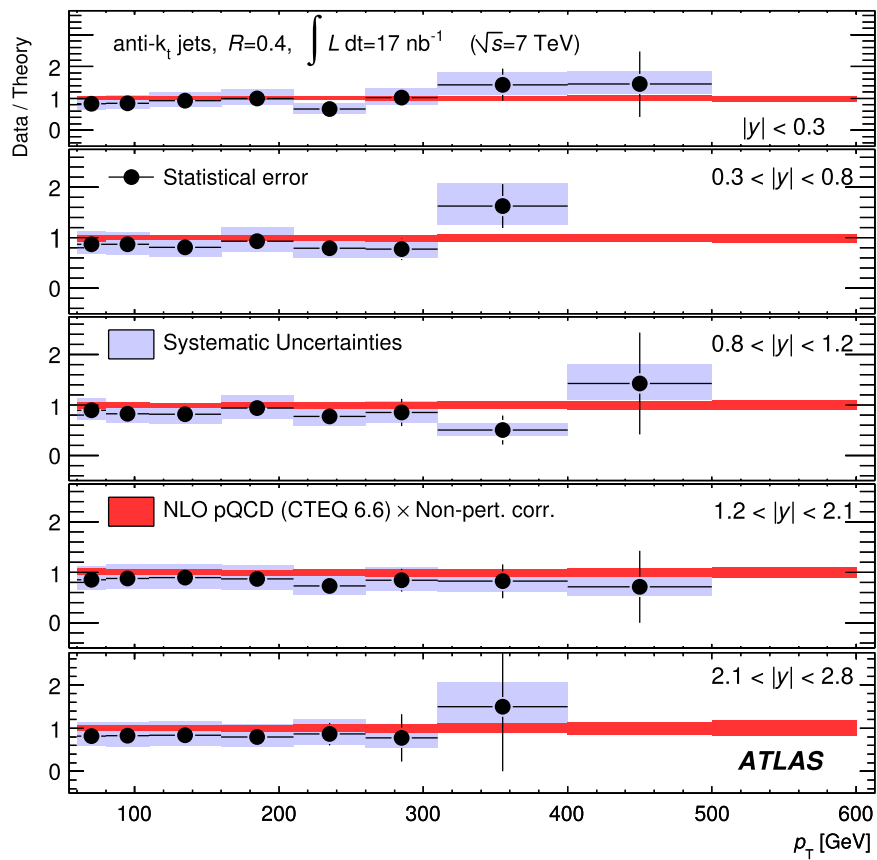
**Fig. 17** Inclusive jet double-differential cross section as a function of jet  $|y|$  in different regions of  $p_T$  for jets identified using the anti- $k_t$  algorithm with  $R = 0.4$ . The data are compared to NLO pQCD calculations to which soft QCD corrections have been applied. The uncertainties on the data and theory are shown as described in Fig. 13



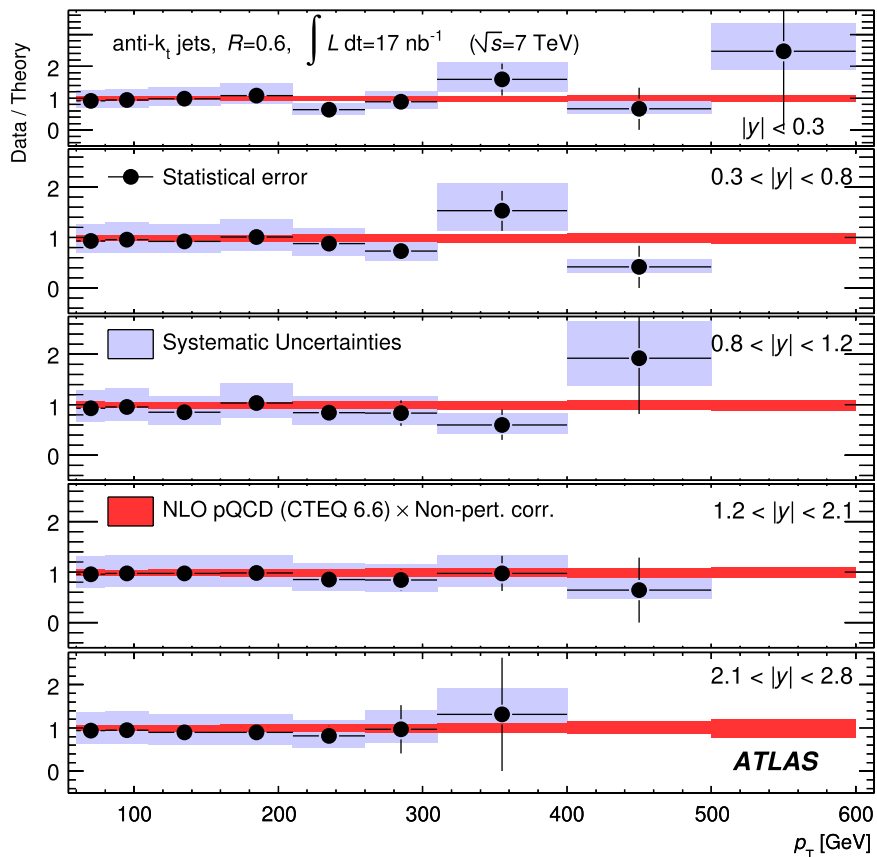
**Fig. 18** Inclusive jet double-differential cross section as a function of jet  $|y|$  in different regions of  $p_T$  for jets identified using the anti- $k_t$  algorithm with  $R = 0.6$ . The data are compared to NLO pQCD calculations to which soft QCD corrections have been applied. The uncertainties on the data and theory are shown as described in Fig. 13



**Fig. 19** Inclusive jet double-differential cross section as a function of jet  $p_T$  in different regions of  $|y|$  for jets identified using the anti- $k_T$  algorithm with  $R = 0.4$ . The ratio of the data to the theoretical prediction is shown, indicating the total systematic uncertainty on the measurement. The uncertainties on the data and theory are shown as described in Fig. 13



**Fig. 20** Inclusive jet double-differential cross section as a function of jet  $p_T$  in different regions of  $|y|$  for jets identified using the anti- $k_T$  algorithm with  $R = 0.6$ . The ratio of the data to the theoretical prediction is shown, indicating the total systematic uncertainty on the measurement. The uncertainties on the data and theory are shown as described in Fig. 13



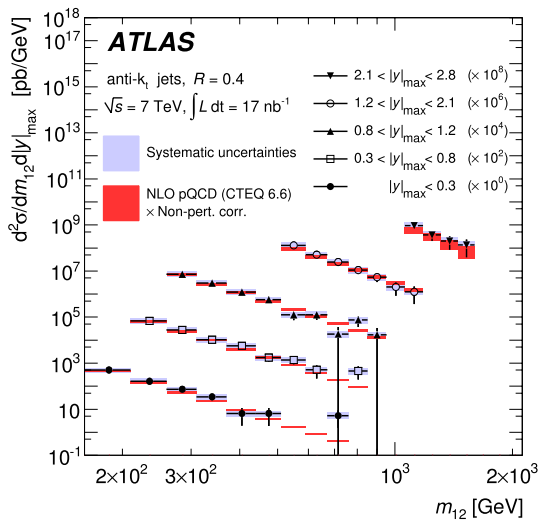


**Fig. 21** Dijet double-differential cross section as a function of dijet mass, binned in the maximum rapidity of the two leading jets,  $|y|_{\max}$ . The results are shown for jets identified using the anti- $k_T$  algorithm with  $R = 0.4$ . The data are compared to NLO pQCD calculations to which soft QCD corrections have been applied. The uncertainties on the data and theory are shown as described in Fig. 13

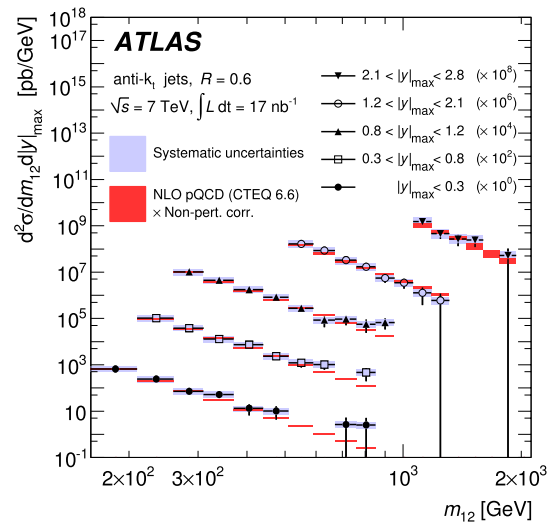


**Fig. 23** Dijet double-differential cross section as a function of dijet mass, binned in the maximum rapidity of the two leading jets,  $|y|_{\max}$ . The results are shown for jets identified using the anti- $k_T$  algorithm with  $R = 0.6$ . The data are compared to NLO pQCD calculations to which soft QCD corrections have been applied. The uncertainties on the data and theory are shown as described in Fig. 13

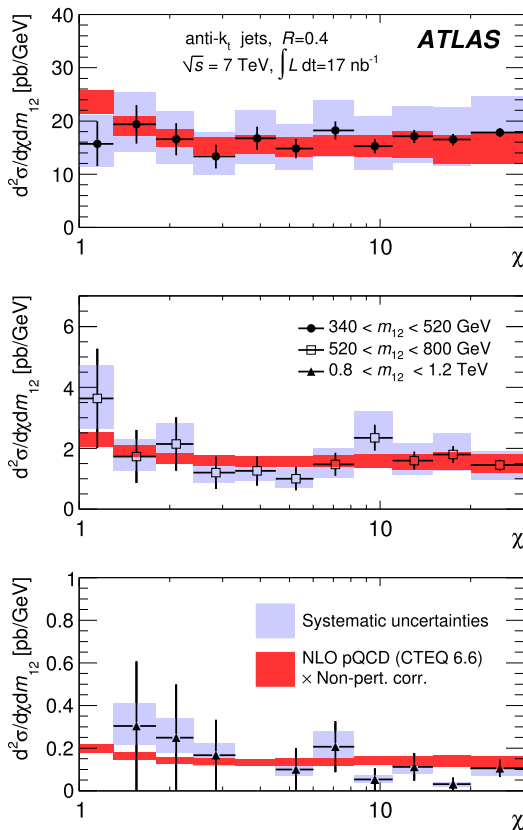


**Fig. 22** Dijet double-differential cross section as a function of angular variable  $\chi$  in different bins of dijet mass  $m_{12}$ , for jets identified using the anti- $k_T$  algorithm with  $R = 0.4$ . The data are compared to NLO pQCD calculations to which soft QCD corrections have been applied. The uncertainties on the data and theory are shown as described in Fig. 13

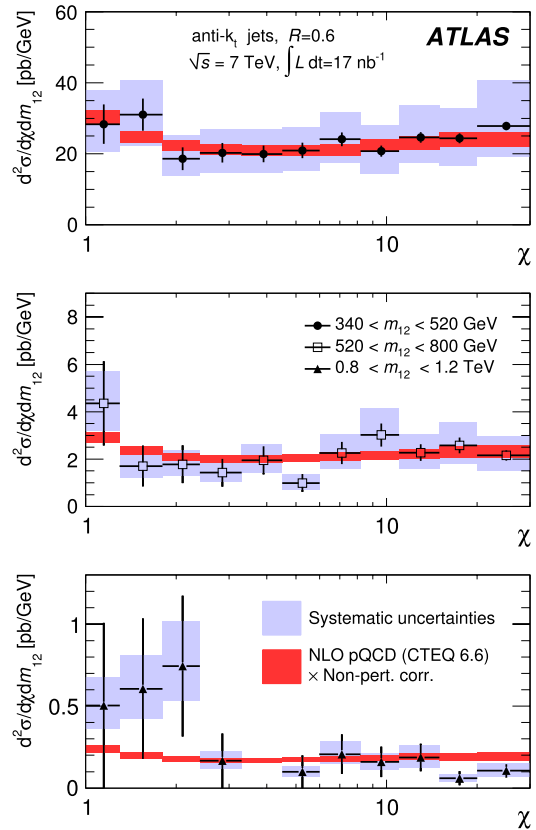


**Fig. 24** Dijet double-differential cross section as a function of angular variable  $\chi$  in different bins of dijet mass  $m_{12}$ , for jets identified using the anti- $k_T$  algorithm with  $R = 0.6$ . The data are compared to NLO pQCD calculations to which soft QCD corrections have been applied. The uncertainties on the data and theory are shown as described in Fig. 13

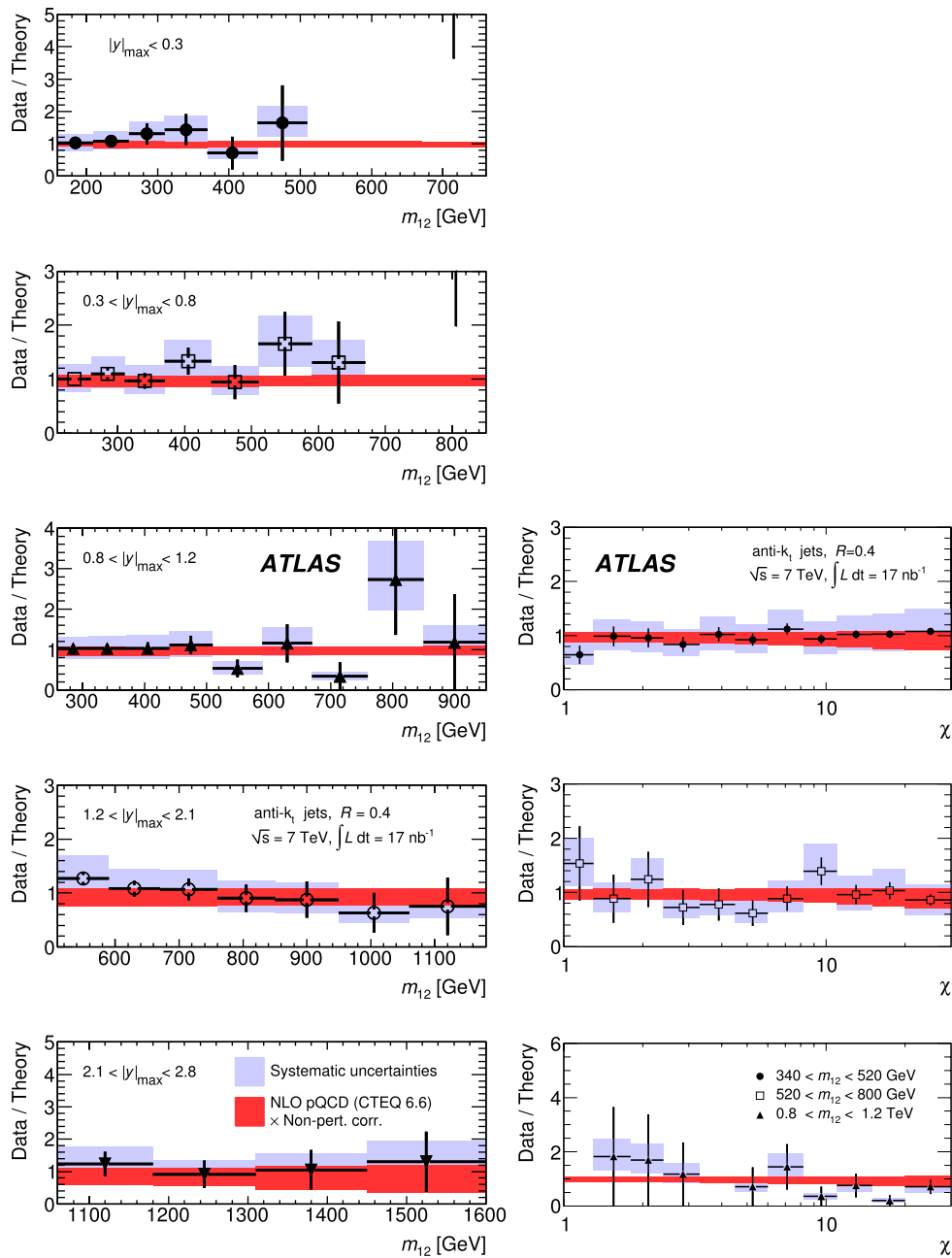


**Fig. 25** Dijet double-differential cross sections as a function of dijet mass  $m_{12}$  and  $\chi$  as shown in Fig. 21 and Fig. 22 respectively, expressed as a ratio to the theoretical prediction. These are shown for jets identified using the anti- $k_r$  algorithm with  $R = 0.4$ . The uncertainties on the

data and theory are displayed as described in Fig. 13. For each of the two lowest  $|y|_{\max}$  bins of the dijet mass spectrum, a data point with large statistical uncertainty at high mass lies outside the plotted range of the ratio (see Tables 7–11)

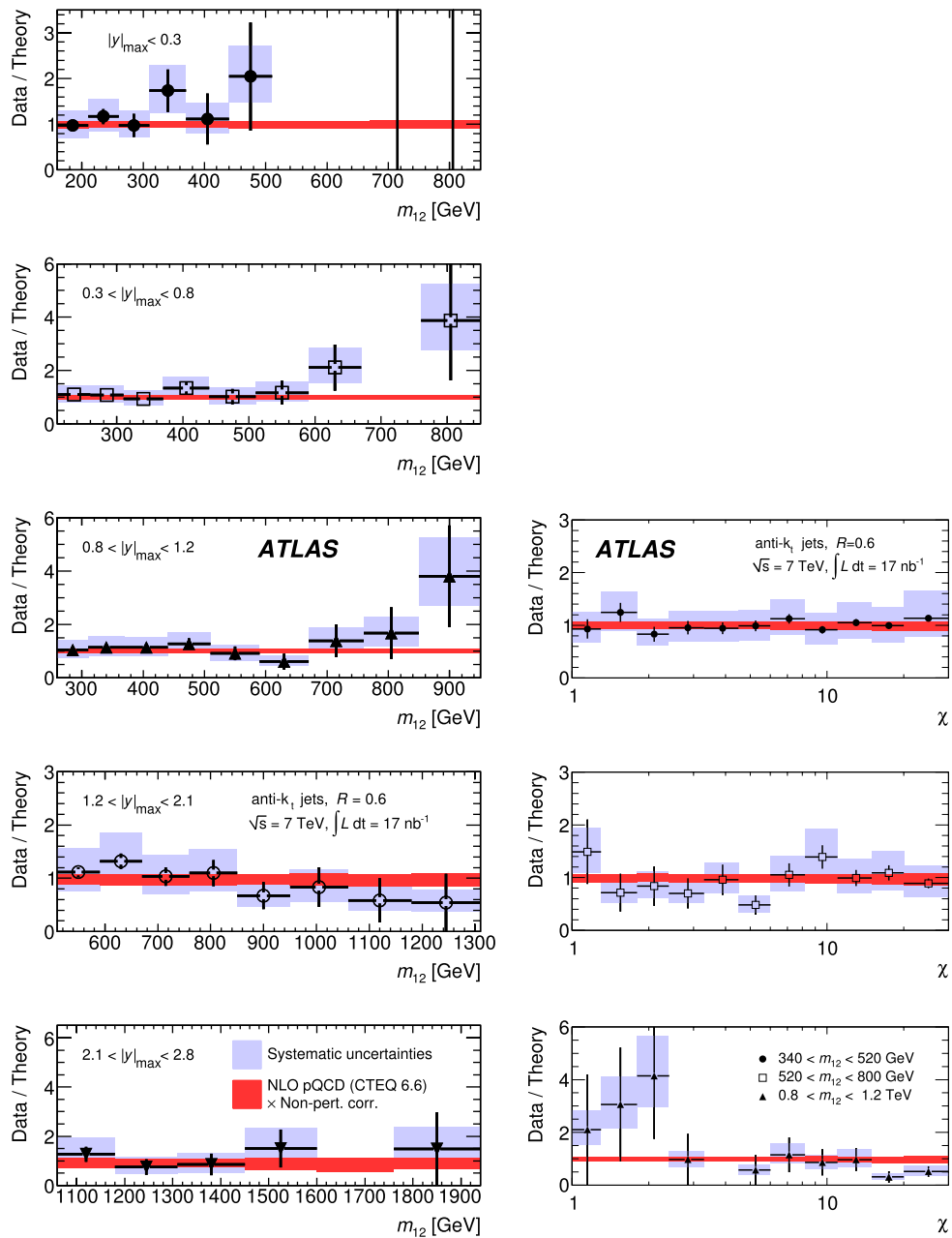


**Fig. 26** Di-jet double-differential cross sections as a function of dijet mass  $m_{12}$  and  $\chi$  as shown in Fig. 23 and Fig. 24 respectively, expressed as a ratio to the theoretical prediction. These are shown for jets identified using the anti- $k_r$  algorithm with  $R = 0.6$ . The uncertainties on the

data and theory are displayed as described in Fig. 13. For the lowest  $|y|_{\max}$  bin of the dijet mass spectrum, two data points with large statistical uncertainty at high mass lie outside the plotted range of the ratio (see Tables 12–16)

**Table 1** Measured inclusive jet double-differential cross section per GeV and per unit rapidity as a function of  $p_T$  for anti- $k_r$  jets with  $R = 0.4$ , compared to NLO pQCD calculations corrected for non-perturbative effects. All uncertainties listed are fractional uncertainties. There is an additional overall uncertainty of 11% due to the measurement of the integrated luminosity which is not included in the systematic uncertainties given above. The statistical uncertainty is calculated as  $1/\sqrt{N}$ , where  $N$  is the number of jets in a given bin

$0 <  y  < 0.3$	60–80	80–110	110–160	160–210	210–260	260–310	310–400	400–500	500–600
$p_T$ [GeV]									
Measured cross section [pb/GeV]	3.5e+04	7.9e+03	1.4e+03	2.7e+02	43	22	8.8	2.0	–
NLO pQCD (CTEQ 6.6) $\times$ non-pert. corr. [pb/GeV]	4.1e+04	9.3e+03	1.6e+03	2.7e+02	66	21	6.2	1.4	0.36
Non-perturbative correction	0.92	0.93	0.94	0.95	0.95	0.96	0.96	0.97	0.97
Statistical uncertainty	0.011	0.020	0.036	0.085	0.21	0.30	0.35	0.71	–
Absolute JES uncertainty	+0.25 –0.22	+0.29 –0.21	+0.27 –0.24	+0.30 –0.24	+0.31 –0.23	+0.29 –0.28	+0.35 –0.25	+0.32 –0.26	–
Unfolding uncertainty	0.04	0.03	0.02	0.02	0.02	0.02	0.02	0.02	–
Total systematic uncertainty	+0.3 –0.2	+0.3 –0.2	+0.3 –0.2	+0.3 –0.2	+0.3 –0.2	0.3	+0.3 –0.2	0.3	–
PDF uncertainty	+0.02 –0.03	0.02	0.02	0.02	0.03	0.03	0.04	0.05	+0.06 –0.05
Scale uncertainty	+0.008 –0.04	+0.007 –0.03	+0.006 –0.04	+0.004 –0.05	+0.003 –0.04	+0.003 –0.05	+0.005 –0.06	+0.007 –0.06	+0.01 –0.06
$\alpha_s$ uncertainty	0.02	0.03	0.03	0.03	0.04	0.04	0.04	0.04	0.04
Non-perturbative correction uncertainty	+0.06 –0	+0.05 –0	+0.04 –0	+0.04 –0	+0.03 –0	+0.03 –0	+0.03 –0	+0.03 –0	+0.02 –0
Total theory uncertainty	+0.07 –0.05	+0.06 –0.05	0.05	+0.05 –0.06	0.06	+0.06 –0.07	+0.07 –0.08	+0.07 –0.09	+0.08 –0.09
$0.3 <  y  < 0.8$									
$p_T$ [GeV]									
Measured cross section [pb/GeV]	3.4e+04	7.9e+03	1.2e+03	2.4e+02	49	15	9.3	–	–
NLO pQCD (CTEQ 6.6) $\times$ non-pert. corr. [pb/GeV]	3.9e+04	9.1e+03	1.5e+03	2.6e+02	63	20	5.7	1.3	0.32
Non-perturbative correction	0.94	0.95	0.95	0.96	0.96	0.96	0.96	0.97	0.97
Statistical uncertainty	0.0089	0.015	0.030	0.069	0.15	0.28	0.27	–	–
Absolute JES uncertainty	+0.27 –0.22	+0.28 –0.22	+0.28 –0.22	+0.27 –0.24	+0.31 –0.23	+0.29 –0.27	+0.34 –0.25	–	–
Unfolding uncertainty	0.04	0.03	0.02	0.02	0.02	0.02	0.02	–	–
Total systematic uncertainty	+0.3 –0.2	+0.3 –0.2	+0.3 –0.2	+0.3 –0.2	+0.3 –0.2	0.3	+0.3 –0.2	–	–
PDF uncertainty	+0.02 –0.03	0.02	0.02	0.02	0.03	0.03	0.04	0.05	+0.07 –0.05
Scale uncertainty	+0.009 –0.06	+0.007 –0.03	+0.006 –0.04	+0.005 –0.05	+0.004 –0.04	+0.003 –0.05	+0.004 –0.05	+0.006 –0.06	+0.007 –0.06
$\alpha_s$ uncertainty	0.02	0.03	0.03	0.03	0.04	0.04	0.04	0.04	0.04
Non-perturbative correction uncertainty	+0.05 –0	+0.03 –0.0004	+0.02 –0.002	+0.02 –0.001	+0.02 –0	+0.02 –0	+0.02 –0	+0.02 –0	+0.02 –0
Total theory uncertainty	+0.06 –0.07	+0.06 –0.05	+0.04 –0.05	+0.04 –0.06	+0.05 –0.06	+0.06 –0.07	+0.06 –0.08	+0.07 –0.09	+0.08 –0.09

**Table 2** Measured inclusive jet double-differential cross section per GeV and per unit rapidity as a function of  $p_T$  for anti- $k_r$  jets with  $R = 0.4$ , compared to NLO pQCD calculations corrected for non-perturbative effects. All uncertainties listed are fractional uncertainties. There is an additional overall uncertainty of 11% due to the measurement of the integrated luminosity which is not included in the systematic uncertainties given above. The statistical uncertainty is calculated as  $1/\sqrt{N}$ , where  $N$  is the number of jets in a given bin

$p_T$ [GeV]	60–80	80–110	110–160	160–210	210–260	260–310	310–400	400–500	500–600
Measured cross section [pb/GeV]	3.2e+04	6.8e+03	1.1e+03	2.1e+02	43	15	2.4	1.5	–
NLO pQCD (CTEQ 6.6) × non-pert. corr. [pb/GeV]	3.5e+04	8.3e+03	1.4e+03	2.2e+02	56	17	4.8	1.0	0.25
Non-perturbative correction	0.92	0.93	0.95	0.95	0.96	0.96	0.97	0.97	0.97
Statistical uncertainty	0.010	0.018	0.035	0.083	0.18	0.32	0.58	0.71	–
Absolute JES uncertainty	+0.27 –0.21	+0.26 –0.22	+0.29 –0.25	+0.32 –0.24	+0.29 –0.28	+0.38 –0.26	+0.34 –0.25	+0.35 –0.27	–
Unfolding uncertainty	0.04	0.03	0.02	0.02	0.02	0.02	0.02	0.03	–
Total systematic uncertainty	+0.3 –0.2	+0.3 –0.2	+0.3 –0.2	+0.3 –0.2	0.3	+0.4 –0.3	0.3	+0.4 –0.3	–
PDF uncertainty	0.02	0.02	+0.01 –0.02	0.02	0.03	+0.04 –0.03	+0.05 –0.04	+0.06 –0.05	+0.07 –0.05
Scale uncertainty	+0.01 –0.06	+0.007 –0.04	+0.005 –0.04	+0.004 –0.05	+0.005 –0.05	+0.004 –0.05	+0.007 –0.06	+0.01 –0.06	+0.01 –0.07
$\alpha_s$ uncertainty	0.02	0.03	0.03	0.03	0.04	0.04	0.04	0.04	0.04
Non-perturbative correction uncertainty	+0.06 –0	+0.04 –0	+0.03 –0	+0.03 –0	+0.03 –0.00004	+0.03 –0.003	+0.03 –0.005	+0.03 –0.007	+0.02 –0.009
Total theory uncertainty	0.07	0.05	0.05	+0.05 –0.06	+0.05 –0.07	+0.06 –0.07	+0.07 –0.08	+0.08 –0.09	+0.09 –0.1
$1.2 <  y  < 2.1$									
$p_T$ [GeV]	60–80	80–110	110–160	160–210	210–260	260–310	310–400	400–500	500–600
Measured cross section [pb/GeV]	2.5e+04	5.6e+03	9.2e+02	1.4e+02	27	9.0	2.2	0.32	–
NLO pQCD (CTEQ 6.6) × non-pert. corr. [pb/GeV]	3.0e+04	6.4e+03	1.0e+03	1.6e+02	37	11	2.6	0.45	0.086
Non-perturbative correction	0.92	0.93	0.94	0.95	0.96	0.96	0.96	0.97	0.97
Statistical uncertainty	0.0078	0.014	0.026	0.069	0.15	0.27	0.41	1.0	–
Absolute JES uncertainty	+0.29 –0.25	+0.30 –0.24	+0.31 –0.23	+0.31 –0.26	+0.34 –0.26	+0.33 –0.29	+0.40 –0.28	+0.43 –0.32	–
Unfolding uncertainty	0.03	0.03	0.02	0.02	0.02	0.02	0.02	0.02	–
Total systematic uncertainty	0.3	+0.3 –0.2	+0.3 –0.2	0.3	0.3	0.3	+0.4 –0.3	+0.4 –0.3	–
PDF uncertainty	0.01	0.01	+0.01 –0.02	+0.03 –0.02	0.03	0.04	+0.05 –0.04	+0.07 –0.05	+0.08 –0.06
Scale uncertainty	+0.01 –0.04	+0.008 –0.04	+0.006 –0.04	+0.003 –0.05	+0.005 –0.05	+0.006 –0.05	+0.006 –0.06	+0.007 –0.06	+0.009 –0.07
$\alpha_s$ uncertainty	0.03	0.03	0.03	0.04	0.04	0.04	0.04	0.04	0.04
Non-perturbative correction uncertainty	+0.06 –0	+0.04 –0	+0.03 –0	+0.03 –0	+0.03 –0	+0.02 –0	+0.02 –0	+0.02 –0	+0.02 –0
Total theory uncertainty	+0.07 –0.05	0.05	+0.05 –0.06	+0.05 –0.06	+0.06 –0.07	+0.06 –0.08	+0.07 –0.08	+0.08 –0.09	+0.1 –0.1

**Table 3** Measured inclusive jet double-differential cross section per GeV and per unit rapidity as a function of  $p_T$  for anti- $k_r$  jets with  $R = 0.4$ , compared to NLO pQCD calculations corrected for non-perturbative effects. All uncertainties listed are fractional uncertainties. There is an additional overall uncertainty of 11% due to the measurement of the integrated luminosity which is not included in the systematic uncertainties given above. The statistical uncertainty is calculated as  $1/\sqrt{N}$ , where  $N$  is the number of jets in a given bin

$p_T$ [GeV]	60–80	80–110	110–160	160–210	210–260	260–310	310–400	400–500	500–600
Measured cross section [pb/GeV]	1.6e+04	3.2e+03	4.6e+02	52	9.3	1.7	0.48	–	–
NLO pQCD (CTEQ 6.6) $\times$ non-pert. corr. [pb/GeV]	1.9e+04	3.9e+03	5.5e+02	66	11	2.2	0.32	0.021	0.00097
Non-perturbative correction	0.91	0.92	0.93	0.94	0.94	0.95	0.95	0.96	0.96
Statistical uncertainty	0.011	0.021	0.043	0.13	0.30	0.71	1.0	–	–
Absolute JES uncertainty	+0.37 –0.27	+0.38 –0.29	+0.39 –0.31	+0.45 –0.33	+0.56 –0.36	+0.58 –0.43	+0.70 –0.44	–	–
Unfolding uncertainty	0.03	0.03	0.02	0.03	0.03	0.03	0.03	–	–
Total systematic uncertainty	+0.4 –0.3	+0.4 –0.3	+0.4 –0.3	+0.4 –0.3	+0.6 –0.4	+0.6 –0.4	+0.7 –0.4	–	–
PDF uncertainty	+0.008 –0.009	0.02	+0.03 –0.02	+0.04 –0.03	+0.06 –0.05	+0.08 –0.06	+0.09 –0.06	+0.1 –0.08	+0.2 –0.1
Scale uncertainty	+0.008 –0.04	+0.005 –0.05	+0.004 –0.04	+0.004 –0.05	+0.0009 –0.07	+0	+0	+0	+0
$\alpha_s$ uncertainty	0.04	0.04	0.04	0.04	0.04	0.04	0.04	0.04	0.04
Non-perturbative correction uncertainty	+0.07 –0	+0.05 –0	+0.04 –0	+0.04 –0	+0.04 –0	+0.03 –0	+0.03 –0	+0.03 –0	+0.03 –0
Total theory uncertainty	+0.08 –0.05	0.06	0.06	0.07	+0.08 –0.1	+0.09 –0.1	0.1	+0.1 –0.2	0.2



**Table 4** Measured inclusive jet double-differential cross section per GeV and per unit rapidity as a function of  $p_T$  for anti- $k_r$  jets with  $R = 0.6$ , compared to NLO pQCD calculations corrected for non-perturbative effects. All uncertainties listed are fractional uncertainties. There is an additional overall uncertainty of 11% due to the measurement of the integrated luminosity which is not included in the systematic uncertainties given above. The statistical uncertainty is calculated as  $1/\sqrt{N}$ , where  $N$  is the number of jets in a given bin

$0 <  y  < 0.3$	60–80	80–110	110–160	160–210	210–260	260–310	310–400	400–500	500–600
$p_T$ [GeV]									
Measured cross section [pb/GeV]	5.0e+04	1.1e+04	1.9e+03	3.4e+02	49	22	11	1.0	1.0
NLO pQCD (CTEQ 6.6) $\times$ non-pert. corr. [pb/GeV]	5.4e+04	1.1e+04	1.9e+03	3.1e+02	78	25	7.0	1.5	0.41
Non-perturbative correction	1.0	1.0	1.0	1.0	0.99	0.99	0.99	0.99	0.99
Statistical uncertainty	0.0096	0.017	0.032	0.076	0.20	0.30	0.32	1.0	1.0
Absolute JES uncertainty	+0.41 -0.28	+0.35 -0.24	+0.30 -0.26	+0.33 -0.27	+0.36 -0.24	+0.31 -0.29	+0.37 -0.26	+0.35 -0.26	+0.34 -0.3
Unfolding uncertainty	0.04	0.03	0.03	0.03	0.02	0.02	0.02	0.02	0.03
Total systematic uncertainty	+0.4 -0.3	+0.4 -0.2	0.3	0.3	+0.4 -0.2	0.3	+0.4 -0.3	+0.4 -0.3	0.3
PDF uncertainty	+0.02 -0.03	0.02	0.02	0.02	0.03	0.03	0.04	0.05	+0.07 -0.05
Scale uncertainty	+0.03 -0.07	+0.02 -0.06	+0.02 -0.06	+0.02 -0.07	+0.02 -0.07	+0.03 -0.07	+0.03 -0.08	+0.02 -0.07	+0.04 -0.09
$\alpha_s$ uncertainty	0.03	0.03	0.03	0.03	0.04	0.04	0.04	0.04	0.05
Non-perturbative correction uncertainty	+0.06 -0	+0.05 -0	+0.04 -0	+0.03 -0	+0.03 -0	+0.02 -0.001	+0.02 -0.003	+0.02 -0.005	+0.01 -0.006
Total theory uncertainty	+0.07 -0.08	+0.06 -0.07	+0.06 -0.07	+0.06 -0.08	+0.06 -0.08	+0.06 -0.09	+0.07 -0.09	+0.08 -0.1	+0.09 -0.1
$0.3 <  y  < 0.8$									
$p_T$ [GeV]									
Measured cross section [pb/GeV]	4.8e+04	1.1e+04	1.7e+03	3.0e+02	64	17	10	0.60	-
NLO pQCD (CTEQ 6.6) $\times$ non-pert. corr. [pb/GeV]	5.2e+04	1.1e+04	1.8e+03	3.0e+02	73	23	6.5	1.4	0.36
Non-perturbative correction	1.1	1.0	1.0	1.0	1.0	0.99	0.99	0.99	0.99
Statistical uncertainty	0.0074	0.013	0.026	0.062	0.13	0.27	0.26	1.0	-
Absolute JES uncertainty	+0.39 -0.27	+0.35 -0.26	+0.33 -0.23	+0.29 -0.27	+0.36 -0.24	+0.32 -0.29	+0.37 -0.27	+0.37 -0.27	+0.37 -0.27
Unfolding uncertainty	0.04	0.03	0.03	0.02	0.02	0.03	0.02	0.02	-
Total systematic uncertainty	+0.4 -0.3	+0.4 -0.3	+0.3 -0.2	0.3	+0.4 -0.2	0.3	+0.4 -0.3	+0.4 -0.3	-
PDF uncertainty	+0.02 -0.03	0.02	0.02	0.02	0.03	0.03	0.04	+0.06 -0.05	+0.07 -0.05
Scale uncertainty	+0.02 -0.06	+0.01 -0.06	+0.02 -0.06	+0.02 -0.07	+0.02 -0.07	+0.02 -0.07	+0.03 -0.08	+0.03 -0.08	+0.03 -0.08
$\alpha_s$ uncertainty	0.03	0.03	0.03	0.03	0.04	0.04	0.04	0.04	0.04
Non-perturbative correction uncertainty	+0.04 -0.02	+0.02 -0.03	0.02	+0.02 -0.001	+0.02 -0.006	+0.02 -0.003	+0.02 -0	+0.02 -0	+0.02 -0
Total theory uncertainty	+0.07 -0.07	+0.06 -0.07	+0.05 -0.08	+0.05 -0.08	+0.06 -0.09	+0.06 -0.09	+0.07 -0.1	+0.08 -0.1	+0.09 -0.1

**Table 5** Measured inclusive jet double-differential cross section per GeV and per unit rapidity as a function of  $p_T$  for anti- $k_r$  jets with  $R = 0.6$ , compared to NLO pQCD calculations corrected for non-perturbative effects. All uncertainties listed are fractional uncertainties. There is an additional overall uncertainty of 11% due to the measurement of the integrated luminosity which is not included in the systematic uncertainties given above. The statistical uncertainty is calculated as  $1/\sqrt{N}$ , where  $N$  is the number of jets in a given bin

$p_T$ [GeV]	60–80	80–110	110–160	160–210	210–260	260–310	310–400	400–500	500–600
Measured cross section [pb/GeV]	4.5e+04	9.5e+03	1.4e+03	2.7e+02	53	16	3.2	2.2	–
NLO pQCD (CTEQ 6.6) $\times$ non-pert. corr. [pb/GeV]	4.8e+04	1.0e+04	1.7e+03	2.6e+02	63	19	5.4	1.1	0.27
Non-perturbative correction	1.1	1.0	1.0	1.0	0.99	0.99	0.99	0.99	0.99
Statistical uncertainty	0.0086	0.015	0.031	0.073	0.16	0.30	0.50	0.58	–
Absolute JES uncertainty	+0.37 –0.27	+0.38 –0.28	+0.37 –0.27	+0.36 –0.25	+0.33 –0.28	+0.38 –0.27	+0.35 –0.27	+0.38 –0.28	–
Unfolding uncertainty	0.04	0.04	0.03	0.02	0.02	0.03	0.02	0.02	–
Total systematic uncertainty	+0.4 –0.3	+0.4 –0.3	+0.4 –0.3	+0.4 –0.3	0.3	+0.4 –0.3	+0.4 –0.3	+0.4 –0.3	–
PDF uncertainty	0.02	0.02	+0.01 –0.02	0.02	0.03	+0.04 –0.03	+0.05 –0.04	+0.06 –0.05	+0.07 –0.06
Scale uncertainty	+0.02 –0.06	+0.02 –0.06	+0.03 –0.07	+0.02 –0.07	+0.03 –0.07	+0.02 –0.07	+0.03 –0.08	+0.03 –0.08	+0.03 –0.08
$\alpha_s$ uncertainty	0.03	0.03	0.03	0.04	0.04	0.04	0.04	0.04	0.04
Non-perturbative correction uncertainty	+0.05 –0	+0.03 –0.009	+0.03 –0.01	+0.03 –0.01	+0.02 –0.01	+0.02 –0.01	+0.02 –0.01	+0.02 –0.009	+0.02 –0.009
Total theory uncertainty	+0.06 –0.07	+0.05 –0.07	+0.06 –0.08	+0.05 –0.08	+0.06 –0.09	+0.06 –0.09	+0.07 –0.1	+0.08 –0.1	+0.09 –0.1
$1.2 <  y  < 2.1$									
$p_T$ [GeV]	60–80	80–110	110–160	160–210	210–260	260–310	310–400	400–500	500–600
Measured cross section [pb/GeV]	3.6e+04	7.6e+03	1.2e+03	1.8e+02	36	10	2.9	0.32	–
NLO pQCD (CTEQ 6.6) $\times$ non-pert. corr. [pb/GeV]	3.8e+04	7.8e+03	1.2e+03	1.8e+02	42	12	3.0	0.50	0.095
Non-perturbative correction	1.1	1.0	1.0	1.0	0.99	0.99	0.99	0.99	0.99
Statistical uncertainty	0.0065	0.012	0.023	0.060	0.13	0.25	0.35	1.0	–
Absolute JES uncertainty	+0.43 –0.29	+0.37 –0.27	+0.36 –0.25	+0.33 –0.29	+0.40 –0.27	+0.35 –0.32	+0.44 –0.30	+0.47 –0.33	–
Unfolding uncertainty	0.04	0.03	0.03	0.02	0.02	0.02	0.02	0.02	–
Total systematic uncertainty	+0.4 –0.3	+0.4 –0.3	+0.4 –0.3	0.3	+0.4 –0.3	0.3	+0.4 –0.3	+0.5 –0.3	–
PDF uncertainty	+0.01 –0.02	0.01	+0.01 –0.02	+0.03 –0.02	+0.04 –0.03	0.04	+0.06 –0.04	+0.07 –0.06	+0.09 –0.06
Scale uncertainty	+0.009 –0.06	+0.01 –0.06	+0.02 –0.07	+0.02 –0.07	+0.03 –0.07	+0.03 –0.08	+0.02 –0.08	+0.02 –0.08	+0.03 –0.09
$\alpha_s$ uncertainty	0.03	0.03	0.04	0.04	0.04	0.04	0.04	0.04	0.04
Non-perturbative correction uncertainty	+0.04 –0.008	+0.03 –0.01	+0.02 –0.007	+0.02 –0.004	+0.02 –0.002	+0.02 –0.002	+0.02 –0	+0.02 –0	+0.02 –0
Total theory uncertainty	+0.05 –0.07	+0.05 –0.07	+0.05 –0.07	+0.05 –0.08	+0.06 –0.09	+0.06 –0.1	+0.07 –0.1	+0.08 –0.1	+0.09 –0.1

**Table 6** Measured inclusive jet double-differential cross section per GeV and per unit rapidity as a function of  $p_T$  for anti- $k_r$  jets with  $R = 0.6$ , compared to NLO pQCD calculations corrected for non-perturbative effects. All uncertainties listed are fractional uncertainties. There is an additional overall uncertainty of 11% due to the measurement of the integrated luminosity which is not included in the systematic uncertainties given above. The statistical uncertainty is calculated as  $1/\sqrt{N}$ , where  $N$  is the number of jets in a given bin

$p_T$ [GeV]	60–80	80–110	110–160	160–210	210–260	260–310	310–400	400–500	500–600
Measured cross section [pb/GeV]	2.3e+04	4.3e+03	5.7e+02	68	10	2.5	0.49	–	–
NLO pQCD (CTEQ 6.6) $\times$ non-pert. corr. [pb/GeV]	2.4e+04	4.6e+03	6.3e+02	76	12	2.6	0.37	0.023	0.00096
Non-perturbative correction	1.0	1.0	1.0	0.99	0.99	0.99	0.99	0.99	0.99
Statistical uncertainty	0.0096	0.018	0.038	0.11	0.29	0.58	1.0	–	–
Absolute JES uncertainty	+0.49 –0.32	+0.46 –0.33	+0.45 –0.32	+0.47 –0.36	+0.60 –0.38	+0.62 –0.45	+0.78 –0.46	–	–
Unfolding uncertainty	0.03	0.03	0.03	0.03	0.03	0.04	0.03	–	–
Total systematic uncertainty	+0.5 –0.3	+0.5 –0.3	+0.5 –0.3	+0.5 –0.4	+0.6 –0.4	+0.6 –0.5	+0.8 –0.5	–	–
PDF uncertainty	+0.009 –0.01	0.02	+0.03 –0.02	+0.05 –0.04	+0.06 –0.05	+0.08 –0.06	+0.1 –0.07	+0.1 –0.09	+0.2 –0.1
Scale uncertainty	+0.02 –0.06	+0.01 –0.06	+0.01 –0.06	+0.02 –0.07	+0.01 –0.07	+0.02 –0.08	+0.02 –0.08	+0.01 –0.08	+0 –0.2
$\alpha_s$ uncertainty	0.04	0.04	0.04	0.04	0.04	0.04	0.05	0.05	0.05
Non-perturbative correction uncertainty	+0.04 –0	+0.03 –0	+0.03 –0	+0.03 –0	+0.02 –0.001	+0.02 –0.01	+0.02 –0.01	+0.02 –0.03	+0.02 –0.04
Total theory uncertainty	+0.06 –0.07	+0.05 –0.07	+0.06 –0.08	+0.07 –0.09	+0.08 –0.09	+0.09 –0.1	0.1	0.1	0.2

**Table 7** Measured dijet double-differential cross section per GeV and per unit absolute rapidity as a function of dijet mass  $m_{12}$  for anti- $k_r$  jets with  $R = 0.4$ , compared to NLO pQCD calculations corrected for non-perturbative effects. All uncertainties listed are fractional uncertainties. There is an additional overall uncertainty of 11% due to the measurement of the integrated luminosity which is not included in the systematic uncertainties given above. The statistical uncertainty is calculated as  $1/\sqrt{N}$ , where  $N$  is the number of events in a given bin

$ \eta _{\max} < 0.3$	160–210	210–260	260–310	310–370	370–440	440–510	510–590	590–670	670–760
$m_{12}$ [GeV]									
Measured cross section [pb/GeV]	500	170	73	34	6.6	6.5	–	–	5.2
NLO pQCD (CTEQ 6.6) $\times$ non-pert. corr. [pb/GeV]	480	150	56	24	9.2	4.0	1.8	0.87	0.42
Non-perturbative correction	0.98	0.99	0.97	0.98	0.96	0.97	0.99	0.98	0.98
Statistical uncertainty	0.094	0.17	0.25	0.33	0.71	0.71	–	–	0.71
Absolute JES uncertainty	+0.25 –0.22	+0.26 –0.23	+0.27 –0.23	+0.28 –0.24	+0.29 –0.24	+0.29 –0.24	–	–	+0.31 –0.25
Relative JES uncertainty	+0.0046 –0.0016	+0.0056 –0.0028	+0.0063 –0.0036	+0.0069 –0.0043	+0.0073 –0.0050	+0.0075 –0.0054	–	–	+0.0073 –0.0062
Unfolding uncertainty	0.1	0.1	0.1	0.1	0.1	0.1	–	–	0.1
Total systematic uncertainty	+0.3 –0.2	+0.3 –0.2	0.3	0.3	0.3	0.3	–	–	0.3
PDF uncertainty	+0.03 –0.04	0.03	0.03	+0.02 –0.03	+0.02 –0.03	0.03	0.03	0.03	0.04
Scale uncertainty	+0.01 –0.04	+0.02 –0.1	+0.02 –0.1	+0.01 –0.1	+0.01 –0.1	+0.01 –0.1	+0.01 –0.1	+0.01 –0.09	+0.009 –0.09
$\alpha_s$ uncertainty	0.02	0.02	0.02	0.03	0.03	0.03	0.03	0.04	0.04
Non-perturbative correction uncertainty	0.05	0.05	0.05	0.05	0.05	0.05	0.05	0.05	0.05
Total theory uncertainty	+0.06 –0.08	+0.07 –0.1	+0.06 –0.1	+0.06 –0.1	+0.06 –0.1	+0.07 –0.1	+0.07 –0.1	+0.07 –0.1	+0.07 –0.1

**Table 8** Measured dijet double-differential cross section per GeV and per unit absolute rapidity as a function of dijet mass  $m_{12}$  for anti- $k_r$  jets with  $R = 0.4$ , compared to NLO pQCD calculations corrected for non-perturbative effects. All uncertainties listed are fractional uncertainties. There is an additional overall uncertainty of 11% due to the measurement of the integrated luminosity which is not included in the systematic uncertainties given above. The statistical uncertainty is calculated as  $1/\sqrt{N}$ , where  $N$  is the number of events in a given bin

	$0.3 <  y _{\text{max}} < 0.8$	210–260	260–310	310–370	370–440	440–510	510–590	590–670	670–760	760–850
$m_{12}$ [GeV]										
Measured cross section [pb/GeV]	680	280	100	57	18	14	5.1	–	4.6	
NLO pQCD (CTEQ 6.6) $\times$ non-pert. corr. [pb/GeV]	680	250	110	43	18	8.3	3.9	2.0	0.99	
Non-perturbative correction	0.97	0.96	0.97	0.97	0.98	0.98	0.97	0.98	0.98	
Statistical uncertainty	0.063	0.098	0.15	0.19	0.33	0.35	0.58	–	0.58	
Absolute JES uncertainty	+0.26 –0.22	+0.26 –0.22	+0.27 –0.23	+0.28 –0.23	+0.29 –0.24	+0.30 –0.24	+0.30 –0.24	–	+0.32 –0.25	
Relative JES uncertainty	0.019	+0.019 –0.020	+0.020 –0.021	+0.020 –0.022	+0.021 –0.022	+0.022 –0.023	+0.023 –0.024	–	0.025	
Unfolding uncertainty	0.1	0.1	0.1	0.1	0.1	0.1	0.1	–	0.1	
Total systematic uncertainty	+0.3 –0.2	+0.3 –0.2	+0.3 –0.2	0.3	0.3	0.3	0.3	–	0.3	
PDF uncertainty	0.03	+0.02 –0.03	+0.02 –0.03	0.02	+0.02 –0.03	0.03	0.03	0.04	0.04	
Scale uncertainty	+0.03 –0.1	+0.02 –0.1	+0.02 –0.1	+0.02 –0.1	+0.02 –0.1	+0.01 –0.1	+0.01 –0.1	+0.01 –0.1	+0.01 –0.1	
$\alpha_s$ uncertainty	0.02	0.02	0.03	0.03	0.03	0.03	0.04	0.04	0.04	
Non-perturbative correction uncertainty	0.05	0.05	0.05	0.05	0.05	0.05	0.05	0.05	0.05	
Total theory uncertainty	+0.07 –0.1	+0.06 –0.1	+0.06 –0.1	+0.06 –0.1	+0.06 –0.1	+0.07 –0.1	+0.07 –0.1	+0.07 –0.1	+0.07 –0.1	+0.08 –0.1

**Table 9** Measured dijet double-differential cross section per GeV and per unit absolute rapidity as a function of dijet mass  $m_{12}$  for anti- $k_r$  jets with  $R = 0.4$ , compared to NLO pQCD calculations corrected for non-perturbative effects. All uncertainties listed are fractional uncertainties. There is an additional overall uncertainty of 11% due to the measurement of the integrated luminosity which is not included in the systematic uncertainties given above. The statistical uncertainty is calculated as  $1/\sqrt{N}$ , where  $N$  is the number of events in a given bin

	$0.8 <  y _{\max} < 1.2$									
$m_{12}$ [GeV]	260–310	310–370	370–440	440–510	510–590	590–670	670–760	760–850	850–950	
Measured cross section [pb/GeV]	730	300	120	57	12	13	1.8	7.5	1.7	
NLO pQCD (CTEQ 6.6) $\times$ non-pert. corr. [pb/GeV]	710	290	120	51	23	11	5.4	2.7	1.4	
Non-perturbative correction	0.98	0.97	0.97	0.98	0.97	0.99	0.98	0.99	0.98	
Statistical uncertainty	0.067	0.096	0.14	0.20	0.41	0.41	1.0	0.50	1.0	
Absolute JES uncertainty	+0.26 -0.22	+0.28 -0.23	+0.29 -0.24	+0.30 -0.24	+0.31 -0.25	+0.32 -0.25	+0.32 -0.26	+0.33 -0.26	+0.34 -0.26	
Relative JES uncertainty	+0.037 -0.036	+0.037 -0.036	0.037	0.038	0.039	+0.041 -0.040	+0.044 -0.041	+0.046 -0.043	+0.049 -0.044	
Unfolding uncertainty	0.1	0.1	0.1	0.1	0.1	0.1	0.1	0.1	0.1	
Total systematic uncertainty	+0.3 -0.2	0.3	0.3	0.3	0.3	0.3	0.3	0.3	+0.4 -0.3	
PDF uncertainty	+0.02 -0.03	0.02	0.02	0.02	0.03	0.03	+0.04 -0.03	0.04	+0.05 -0.04	
Scale uncertainty	+0.03 -0.2	+0.02 -0.2	+0.02 -0.1	+0.02 -0.1	+0.01 -0.1	+0.01 -0.1	+0.01 -0.1	+0.01 -0.1	+0.01 -0.1	
$\alpha_s$ uncertainty	0.02	0.03	0.03	0.03	0.03	0.04	0.04	0.04	0.04	
Non-perturbative correction uncertainty	0.05	0.05	0.05	0.05	0.05	0.05	0.05	0.05	0.05	
Total theory uncertainty	+0.07 -0.2	+0.06 -0.2	+0.06 -0.2	+0.07 -0.1	+0.07 -0.1	+0.07 -0.1	+0.07 -0.1	+0.08 -0.1	+0.08 -0.1	

**Table 10** Measured dijet double-differential cross section per GeV and per unit absolute rapidity as a function of dijet mass  $m_{12}$  for anti- $k_r$  jets with  $R = 0.4$ , compared to NLO pQCD calculations corrected for non-perturbative effects. All uncertainties listed are fractional uncertainties. There is an additional overall uncertainty of 11% due to the measurement of the integrated luminosity which is not included in the systematic uncertainties given above. The statistical uncertainty is calculated as  $1/\sqrt{N}$ , where  $N$  is the number of events in a given bin

$1.2 <  y _{\max} < 2.1$	510–590	590–670	670–760	760–850	850–950	950–1060	1060–1180
$m_{12}$ [GeV]							
Measured cross section [pb/GeV]	130	51	25	11	5.4	2.0	1.3
NLO pQCD (CTEQ 6.6) $\times$ non-pert. corr. [pb/GeV]	100	47	23	12	6.1	3.2	1.7
Non-perturbative correction	0.96	0.96	0.96	1.0	0.96	0.98	0.97
Statistical uncertainty	0.086	0.14	0.19	0.28	0.38	0.58	0.71
Absolute JES uncertainty	+0.30 -0.26	+0.31 -0.26	+0.32 -0.26	+0.32 -0.26	+0.33 -0.26	+0.34 -0.27	+0.35 -0.27
Relative JES uncertainty	+0.081 -0.083	+0.082 -0.081	+0.084 -0.080	+0.086 -0.080	+0.088 -0.080	+0.091 -0.081	+0.095 -0.082
Unfolding uncertainty	0.1	0.1	0.1	0.1	0.1	0.1	0.1
Total systematic uncertainty	0.3	0.3	0.3	+0.4 -0.3	+0.4 -0.3	+0.4 -0.3	+0.4 -0.3
PDF uncertainty	0.03	0.03	0.03	0.04	+0.05 -0.04	+0.05 -0.04	+0.06 -0.05
Scale uncertainty	+0.04 -0.2	+0.05 -0.2	+0.04 -0.2	+0.03 -0.2	+0.03 -0.2	+0.03 -0.2	+0.03 -0.2
$\alpha_s$ uncertainty	0.03	0.03	0.04	0.04	0.04	0.04	0.04
Non-perturbative correction uncertainty	0.05	0.05	0.05	0.05	0.05	0.05	0.05
Total theory uncertainty	+0.08 -0.3	+0.08 -0.3	+0.08 -0.2	+0.08 -0.2	+0.08 -0.2	+0.09 -0.2	+0.09 -0.2

**Table 11** Measured dijet double-differential cross section per GeV and per unit absolute rapidity as a function of dijet mass  $m_{12}$  for anti- $k_T$  jets with  $R = 0.4$ , compared to NLO pQCD calculations corrected for non-perturbative effects. All uncertainties listed are fractional uncertainties. There is an additional overall uncertainty of 11% due to the measurement of the integrated luminosity which is not included in the systematic uncertainties given above. The statistical uncertainty is calculated as  $1/\sqrt{N}$ , where  $N$  is the number of events in a given bin

$m_{12}$ [GeV]	1060–1180	1180–1310	1310–1450	1450–1600
Measured cross section [pb/GeV]	9.3	3.7	2.0	1.4
NLO pQCD (CTEQ 6.6) $\times$ non-pert. corr. [pb/GeV]	7.5	4.0	1.9	1.0
Non-perturbative correction	0.91	0.93	0.97	0.98
Statistical uncertainty	0.29	0.45	0.58	0.71
Absolute JES uncertainty	+0.41 -0.32	+0.43 -0.33	+0.45 -0.35	+0.47 -0.37
Relative JES uncertainty	+0.14 -0.15	+0.15 -0.16	+0.15 -0.16	0.16
Unfolding uncertainty	0.1	0.1	0.1	0.1
Total systematic uncertainty	0.4	+0.5 -0.4	+0.5 -0.4	+0.5 -0.4
PDF uncertainty	0.05	+0.06 -0.05	+0.07 -0.05	+0.08 -0.06
Scale uncertainty	+0.08 -0.4	+0.09 -0.4	+0.1 -0.5	+0.2 -0.7
$\alpha_s$ uncertainty	0.04	0.04	0.04	0.03
Non-perturbative correction uncertainty	0.05	0.05	0.05	0.05
Total theory uncertainty	+0.1 -0.4	+0.1 -0.4	+0.2 -0.6	+0.2 -0.7



**Table 12** Measured dijet double-differential cross section per GeV and per unit absolute rapidity as a function of dijet mass  $m_{12}$  for anti- $k_r$  jets with  $R = 0.6$ , compared to NLO pQCD calculations corrected for non-perturbative effects. All uncertainties listed are fractional uncertainties. There is an additional overall uncertainty of 11% due to the measurement of the integrated luminosity which is not included in the systematic uncertainties given above. The statistical uncertainty is calculated as  $1/\sqrt{N}$ , where  $N$  is the number of events in a given bin

$ y _{\max} < 0.3$	160–210	210–260	260–310	310–370	370–440	440–510	510–590	590–670	670–760	760–850
$m_{12}$ [GeV]	670	240	72	53	13	10	–	–	2.6	2.5
Measured cross section [pb/GeV]	690	210	74	30	12	5.0	2.2	1.1	0.51	0.26
NLO pQCD (CTEQ 6.6) $\times$ non-pert. corr. [pb/GeV]	1.1	1.1	1.0	1.0	1.0	1.0	1.0	1.0	1.0	1.0
Non-perturbative correction										
Statistical uncertainty	0.081	0.14	0.26	0.27	0.50	0.58	–	–	1.0	1.0
Absolute JES uncertainty	+0.32 –0.25	+0.32 –0.25	+0.31 –0.26	+0.31 –0.26	+0.31 –0.26	+0.31 –0.26	–	–	+0.33 –0.27	+0.33 –0.27
Relative JES uncertainty	+0.0012 –0.0023	+0.0023 –0.0039	+0.0032 –0.0051	+0.0040 –0.0060	+0.0049 –0.0067	+0.0058 –0.0072	–	–	+0.0083 –0.0075	+0.0091 –0.0072
Unfolding uncertainty	0.1	0.1	0.1	0.1	0.1	0.1	–	–	0.1	0.1
Total systematic uncertainty	0.3	0.3	0.3	0.3	0.3	0.3	–	–	0.3	0.3
PDF uncertainty	+0.03 –0.04	0.03	0.03	+0.02 –0.03	+0.02 –0.03	0.03	0.03	0.03	0.04	0.04
Scale uncertainty	+0.03 –0.06	+0.01 –0.06	+0.008 –0.05	+0.006 –0.04	+0.003 –0.05	+0.004 –0.05	+0.003 –0.05	+0.003 –0.05	+0.005 –0.06	+0.01 –0.06
$\alpha_s$ uncertainty	0.02	0.02	0.02	0.03	0.03	0.03	0.04	0.04	0.04	0.04
Non-perturbative correction uncertainty	0.05	0.05	0.05	0.05	0.05	0.05	0.05	0.05	0.05	0.05
Total theory uncertainty	+0.07 –0.09	+0.06 –0.09	+0.06 –0.08	+0.06 –0.07	+0.06 –0.08	+0.07 –0.08	+0.07 –0.08	+0.07 –0.09	+0.08 –0.09	+0.08 –0.1

**Table 13** Measured dijet double-differential cross section per GeV and per unit absolute rapidity as a function of dijet mass  $m_{12}$  for anti- $k_r$  jets with  $R = 0.6$ , compared to NLO pQCD calculations corrected for non-perturbative effects. All uncertainties listed are fractional uncertainties. There is an additional overall uncertainty of 11% due to the measurement of the integrated luminosity which is not included in the systematic uncertainties given above. The statistical uncertainty is calculated as  $1/\sqrt{N}$ , where  $N$  is the number of events in a given bin

	$0.3 <  y _{\max} < 0.8$									
$m_{12}$ [GeV]	210–260	260–310	310–370	370–440	440–510	510–590	590–670	670–760	760–850	
Measured cross section [pb/GeV]	1000	380	130	73	24	12	10	–	4.6	
NLO pQCD (CTEQ 6.6) $\times$ non-pert. corr. [pb/GeV]	940	350	140	55	23	10	4.9	2.4	1.2	
Non-perturbative correction	1.1	1.0	1.0	1.0	1.0	1.0	1.0	1.0	1.0	
Statistical uncertainty	0.051	0.085	0.13	0.16	0.29	0.38	0.41	–	0.58	
Absolute JES uncertainty	+0.30 –0.25	+0.31 –0.25	+0.31 –0.25	+0.32 –0.26	+0.32 –0.26	+0.33 –0.26	+0.33 –0.26	–	+0.34 –0.27	
Relative JES uncertainty	+0.020 –0.021	0.021	+0.021 –0.022	0.022	0.023	+0.024 –0.023	0.024	–	+0.026 –0.024	
Unfolding uncertainty	0.1	0.1	0.1	0.1	0.1	0.1	0.1	–	0.1	
Total systematic uncertainty	0.3	0.3	0.3	0.3	0.3	0.3	0.3	–	+0.4 –0.3	
PDF uncertainty	0.03	0.03	+0.02 –0.03	0.02	+0.02 –0.03	0.03	0.03	0.04	0.04	
Scale uncertainty	+0.01 –0.05	+0.007 –0.04	+0.005 –0.04	+0.004 –0.04	+0.003 –0.04	+0.002 –0.04	+0.003 –0.05	+0.005 –0.05	+0.006 –0.06	
$\alpha_s$ uncertainty	0.02	0.02	0.03	0.03	0.03	0.04	0.04	0.04	0.04	
Non-perturbative correction uncertainty	0.05	0.05	0.05	0.05	0.05	0.05	0.05	0.05	0.05	
Total theory uncertainty	+0.06 –0.08	+0.06 –0.08	+0.06 –0.08	+0.06 –0.08	+0.06 –0.08	+0.07 –0.08	+0.07 –0.09	+0.07 –0.09	+0.08 –0.1	

**Table 14** Measured dijet double-differential cross section per GeV and per unit absolute rapidity as a function of dijet mass  $m_{12}$  for anti- $k_r$  jets with  $R = 0.6$ , compared to NLO pQCD calculations corrected for non-perturbative effects. All uncertainties listed are fractional uncertainties. There is an additional overall uncertainty of 11% due to the measurement of the integrated luminosity which is not included in the systematic uncertainties given above. The statistical uncertainty is calculated as  $1/\sqrt{N}$ , where  $N$  is the number of events in a given bin

$0.8 <  y _{\max} < 1.2$	260–310	310–370	370–440	440–510	510–590	590–670	670–760	760–850	850–950
$m_{12}$ [GeV]									
Measured cross section [pb/GeV]	1000	450	180	83	27	8.5	9.3	5.6	6.7
NLO pQCD (CTEQ 6.6) $\times$ non-pert. corr. [pb/GeV]	980	390	150	65	30	14	6.7	3.4	1.8
Non-perturbative correction	1.1	1.1	1.0	1.0	1.0	1.0	1.0	1.0	1.0
Statistical uncertainty	0.057	0.079	0.12	0.17	0.28	0.50	0.45	0.58	0.50
Absolute JES uncertainty	+0.34 -0.26	+0.33 -0.26	+0.33 -0.26	+0.33 -0.26	+0.33 -0.26	+0.34 -0.27	+0.34 -0.27	+0.35 -0.27	+0.36 -0.27
Relative JES uncertainty	+0.038 -0.036	+0.040 -0.037	+0.041 -0.038	+0.042 -0.039	+0.043 -0.040	+0.044 -0.041	+0.045 -0.042	+0.046 -0.043	+0.047 -0.044
Unfolding uncertainty	0.1	0.1	0.1	0.1	0.1	0.1	0.1	0.1	0.1
Total systematic uncertainty	+0.4 -0.3	+0.4 -0.3	0.3	0.3	+0.4 -0.3	+0.4 -0.3	+0.4 -0.3	+0.4 -0.3	+0.4 -0.3
PDF uncertainty	+0.02 -0.03	0.02	0.02	0.02	0.03	0.03	+0.04 -0.03	0.04	+0.05 -0.04
Scale uncertainty	+0.009 -0.06	+0.008 -0.06	+0.005 -0.04	+0.003 -0.04	+0.003 -0.04	+0.003 -0.05	+0.004 -0.05	+0.004 -0.05	+0.003 -0.05
$\alpha_s$ uncertainty	0.03	0.03	0.03	0.03	0.04	0.04	0.04	0.04	0.04
Non-perturbative correction uncertainty	0.05	0.05	0.05	0.05	0.05	0.05	0.05	0.05	0.05
Total theory uncertainty	+0.06 -0.09	+0.06 -0.08	+0.06 -0.08	+0.06 -0.08	+0.07 -0.08	+0.07 -0.08	+0.07 -0.09	+0.08 -0.09	+0.08 -0.09

**Table 15** Measured dijet double-differential cross section per GeV and per unit absolute rapidity as a function of dijet mass  $m_{12}$  for anti- $k_T$  jets with  $R = 0.6$ , compared to NLO pQCD calculations corrected for non-perturbative effects. All uncertainties listed are fractional uncertainties. There is an additional overall uncertainty of 11% due to the measurement of the integrated luminosity which is not included in the systematic uncertainties given above. The statistical uncertainty is calculated as  $1/\sqrt{N}$ , where  $N$  is the number of events in a given bin

$1.2 <  y _{\max} < 2.1$	510–590	590–670	670–760	760–850	850–950	950–1060	1060–1180	1180–1310
$m_{12}$ [GeV]								
Measured cross section [pb/GeV]	160	86	33	17	5.6	3.5	1.3	0.6
NLO pQCD (CTEQ 6.6) $\times$ non-pert. corr. [pb/GeV]	150	66	32	16	8.3	4.2	2.2	1.1
Non-perturbative correction	1.1	1.1	1.0	1.0	1.0	1.0	1.1	1.0
Statistical uncertainty	0.076	0.11	0.16	0.22	0.38	0.45	0.71	1.0
Absolute JES uncertainty	+0.38 –0.29	+0.38 –0.29	+0.38 –0.29	+0.38 –0.29	+0.38 –0.29	+0.39 –0.29	+0.39 –0.30	+0.40 –0.30
Relative JES uncertainty	0.080	+0.082 –0.080	+0.084 –0.081	+0.086 –0.081	+0.089 –0.083	+0.091 –0.084	+0.094 –0.086	+0.098 –0.089
Unfolding uncertainty	0.1	0.1	0.1	0.1	0.1	0.1	0.1	0.1
Total systematic uncertainty	+0.4 –0.3	+0.4 –0.3	+0.4 –0.3	+0.4 –0.3	+0.4 –0.3	+0.4 –0.3	+0.4 –0.3	+0.4 –0.3
PDF uncertainty	+0.02 –0.03	0.03	0.03	0.04	0.04	0.05	0.05	+0.06 –0.05
Scale uncertainty	+0.01 –0.1	+0.01 –0.1	+0.009 –0.1	+0.006 –0.1	+0.004 –0.09	+0.005 –0.1	+0.008 –0.1	+0.007 –0.1
$\alpha_s$ uncertainty	0.04	0.04	0.04	0.04	0.04	0.05	0.04	0.04
Non-perturbative correction uncertainty	0.05	0.05	0.05	0.05	0.05	0.05	0.05	0.05
Total theory uncertainty	+0.07 –0.1	+0.07 –0.1	+0.07 –0.1	+0.08 –0.1	+0.08 –0.1	+0.09 –0.1	+0.09 –0.1	+0.09 –0.2

**Table 16** Measured dijet double-differential cross section per GeV and per unit absolute rapidity as a function of dijet mass  $m_{12}$  for anti- $k_T$  jets with  $R = 0.6$ , compared to NLO pQCD calculations corrected for non-perturbative effects. All uncertainties listed are fractional uncertainties. There is an additional overall uncertainty of 11% due to the measurement of the integrated luminosity which is not included in the systematic uncertainties given above. The statistical uncertainty is calculated as  $1/\sqrt{N}$ , where  $N$  is the number of events in a given bin

$m_{12}$ [GeV]	1060–1180	1180–1310	1310–1450	1450–1600	1600–1760	1760–1940
Measured cross section [pb/GeV]	15	4.6	2.7	2.4	–	0.52
NLO pQCD (CTEQ 6.6) $\times$ non-pert. corr. [pb/GeV]	12	6.1	3.1	1.6	0.79	0.35
Non-perturbative correction	1.0	1.1	1.1	1.0	1.2	0.93
Statistical uncertainty	0.22	0.41	0.50	0.50	–	1.0
Absolute JES uncertainty	+0.49 –0.35	+0.50 –0.36	+0.50 –0.37	+0.52 –0.37	–	+0.57 –0.40
Relative JES uncertainty	+0.15 –0.14	+0.15 –0.14	+0.16 –0.15	+0.17 –0.15	–	+0.19 –0.15
Unfolding uncertainty	0.1	0.1	0.1	0.1	–	0.1
Total systematic uncertainty	+0.5 –0.4	+0.5 –0.4	+0.5 –0.4	+0.6 –0.4	–	+0.6 –0.4
PDF uncertainty	+0.06 –0.05	+0.06 –0.05	+0.07 –0.05	+0.08 –0.06	+0.08 –0.06	+0.09 –0.07
Scale uncertainty	+0.04 –0.3	+0.02 –0.2	+0.02 –0.2	+0.06 –0.4	+0.08 –0.4	+0.04 –0.3
$\alpha_s$ uncertainty	0.04	0.05	0.05	0.05	0.03	0.06
Non-perturbative correction uncertainty	0.05	0.05	0.05	0.05	0.05	0.05
Total theory uncertainty	+0.1 –0.3	+0.1 –0.2	+0.1 –0.2	+0.1 –0.4	+0.1 –0.4	+0.1 –0.3

$2.1 < |y|_{\text{max}} < 2.8$

**Table 17** Measured dijet double-differential cross section per GeV and per unit  $\chi$  as a function of the dijet angular variable  $\chi$  for anti- $k_r$  jets with  $R = 0.4$ , compared to NLO pQCD calculations corrected for non-perturbative effects. All uncertainties listed are fractional uncertainties. There is an additional overall uncertainty of 11% due to the measurement of the integrated luminosity which is not included in the systematic uncertainties given above. The statistical uncertainty is calculated as  $1/\sqrt{N}$ , where  $N$  is the number of events in a given bin

$340 < m_{12} < 520$ GeV		1–1.3	1.3–1.8	1.8–2.4	2.4–3.3	3.3–4.5	4.5–6	6–8.2	8.2–11	11–15	15–20	20–30
$\chi$		16	19	17	13	17	15	18	15	17	16	18
Measured cross section [pb/GeV]		24	20	17	16	16	16	16	16	17	16	17
NLO pQCD (CTEQ 6.6) $\times$ non-pert. corr. [pb/GeV]		0.98	0.98	0.97	0.97	0.97	0.97	0.98	0.98	0.97	0.95	0.97
Non-perturbative correction												
Statistical uncertainty		0.27	0.19	0.18	0.17	0.13	0.12	0.091	0.088	0.070	0.063	0.044
Absolute JES uncertainty		+0.32	+0.29	+0.30	+0.32	+0.30	+0.29	+0.29	+0.34	+0.32	+0.34	+0.36
Relative JES uncertainty		-0.26	-0.25	-0.27	-0.24	-0.25	-0.24	-0.25	-0.27	-0.26	-0.27	-0.28
Unfolding uncertainty		+0.027	+0.028	+0.026	+0.030	+0.035	+0.043	+0.049	+0.051	+0.065	+0.092	+0.079
Total systematic uncertainty		-0.025	-0.026	-0.034	-0.028	-0.040	-0.040	-0.040	-0.052	-0.067	-0.058	-0.074
PDF uncertainty		0.1	0.1	0.1	0.1	0.1	0.1	0.1	0.1	0.1	0.1	0.1
Scale uncertainty		0.3	0.3	0.3	0.3	0.3	0.3	0.3	+0.4	0.3	+0.4	+0.4
$\alpha_s$ uncertainty		0.02	0.02	0.02	0.02	0.02	0.02	0.02	0.02	0.02	0.02	0.02
Non-perturbative correction uncertainty		+0.01	+0.01	+0.01	+0.02	+0.02	+0.02	+0.02	+0.03	+0.04	+0.06	+0.06
Total theory uncertainty		-0.1	-0.1	-0.1	-0.1	-0.1	-0.2	-0.2	-0.2	-0.2	-0.2	-0.3

**Table 18** Measured dijet double-differential cross section per GeV and per unit  $\chi$  as a function of the dijet angular variable  $\chi$  for anti- $k_r$  jets with  $R = 0.4$ , compared to NLO pQCD calculations corrected for non-perturbative effects. All uncertainties listed are fractional uncertainties. There is an additional overall uncertainty of 11% due to the measurement of the integrated luminosity which is not included in the systematic uncertainties given above. The statistical uncertainty is calculated as  $1/\sqrt{N}$ , where  $N$  is the number of events in a given bin

	1-1.3	1.3-1.8	1.8-2.4	2.4-3.3	3.3-4.5	4.5-6	6-8.2	8.2-11	11-15	15-20	20-30
$\chi$											
Measured cross section [pb/GeV]	3.6	1.7	2.1	1.2	1.3	1.0	1.5	2.3	1.6	1.8	1.4
NLO pQCD (CTEQ 6.6) $\times$ non-pert. corr. [pb/GeV]	2.4	2.0	1.7	1.7	1.6	1.6	1.7	1.7	1.7	1.7	1.7
Non-perturbative correction	0.99	0.99	0.98	0.98	0.97	0.98	0.98	0.98	0.98	0.98	0.95
Statistical uncertainty	0.45	0.50	0.41	0.45	0.38	0.38	0.26	0.18	0.19	0.15	0.12
Absolute JES uncertainty	+0.29 -0.25	+0.31 -0.26	+0.30 -0.25	+0.29 -0.25	+0.30 -0.23	+0.33 -0.26	+0.34 -0.26	+0.35 -0.27	+0.35 -0.27	+0.37 -0.26	+0.31 -0.30
Relative JES uncertainty	0.028	+0.026 -0.029	+0.030 -0.020	+0.032 -0.031	+0.031 -0.035	+0.047 -0.041	+0.049 -0.054	+0.063 -0.058	+0.072 -0.056	+0.060 -0.082	+0.073 -0.080
Unfolding uncertainty	0.1	0.1	0.1	0.1	0.1	0.1	0.1	0.1	0.1	0.1	0.1
Total systematic uncertainty	0.3	0.3	0.3	0.3	0.3	+0.4 -0.3	+0.4 -0.3	+0.4 -0.3	+0.4 -0.3	+0.4 -0.3	0.3
PDF uncertainty	0.03	0.03	0.03	0.03	0.03	0.03	0.03	0.03	0.03	0.03	0.03
Scale uncertainty	+0.01 -0.1	+0.01 -0.1	+0.01 -0.1	+0.01 -0.1	+0.01 -0.1	+0.02 -0.1	+0.02 -0.2	+0.02 -0.2	+0.04 -0.2	+0.05 -0.2	+0.06 -0.3
$\alpha_s$ uncertainty	0.03	0.03	0.03	0.03	0.03	0.03	0.03	0.03	0.03	0.03	0.03
Non-perturbative correction uncertainty	0.05	0.05	0.05	0.05	0.05	0.05	0.05	0.05	0.05	0.05	0.05
Total theory uncertainty	+0.07 -0.1	+0.07 -0.1	+0.07 -0.1	+0.07 -0.1	+0.07 -0.1	+0.07 -0.2	+0.07 -0.2	+0.07 -0.2	+0.08 -0.2	+0.08 -0.3	+0.09 -0.3

**Table 19** Measured dijet double-differential cross section per GeV and per unit  $\chi$  as a function of the dijet angular variable  $\chi$  for anti- $t_t$  jets with  $R = 0.4$ , compared to NLO pQCD calculations corrected for non-perturbative effects. All uncertainties listed are fractional uncertainties. There is an additional overall uncertainty of 11% due to the measurement of the integrated luminosity which is not included in the systematic uncertainties given above. The statistical uncertainty is calculated as  $1/\sqrt{N}$ , where  $N$  is the number of events in a given bin

$800 < m_{12} < 1200$ GeV	1–1.3	1.3–1.8	1.8–2.4	2.4–3.3	3.3–4.5	4.5–6	6–8.2	8.2–11	11–15	15–20	20–30
$\chi$											
Measured cross section [pb/GeV]	–	0.30	0.25	0.17	–	0.10	0.21	0.053	0.11	0.031	0.11
NLO pQCD (CTEQ 6.6) $\times$ non-pert. corr. [pb/GeV]	0.20	0.17	0.15	0.14	0.14	0.14	0.14	0.15	0.15	0.15	0.15
Non-perturbative correction	0.98	0.98	0.98	0.99	0.98	0.97	0.98	0.99	0.99	0.99	0.96
Statistical uncertainty	–	1.0	1.0	1.0	–	1.0	0.58	1.0	0.58	1.0	0.38
Absolute JES uncertainty	–	+0.34 –0.26	+0.35 –0.26	+0.32 –0.27	–	+0.38 –0.27	+0.33 –0.27	+0.34 –0.27	+0.37 –0.28	+0.37 –0.32	+0.36 –0.29
Relative JES uncertainty	–	+0.032 –0.030	+0.035 –0.032	+0.038 –0.031	–	+0.048 –0.054	+0.066 –0.043	+0.064 –0.063	+0.078 –0.064	+0.11 –0.098	+0.11 –0.10
Unfolding uncertainty	–	0.1	0.1	0.1	–	0.1	0.1	0.1	0.1	0.1	0.1
Total systematic uncertainty	–	+0.4 –0.3	+0.4 –0.3	0.3	–	+0.4 –0.3	+0.4 –0.3	+0.4 –0.3	+0.4 –0.3	+0.4 –0.3	+0.4 –0.3
PDF uncertainty	+0.05 –0.04	+0.05 –0.04	+0.05 –0.04	+0.05 –0.04	+0.05 –0.04	+0.05 –0.04	+0.05 –0.04	+0.05 –0.04	+0.05 –0.04	+0.05 –0.04	+0.05 –0.04
Scale uncertainty	+0.006 –0.008	+0.007 –0.009	+0.007 –0.1	+0.009 –0.1	+0.01 –0.1	+0.02 –0.1	+0.02 –0.2	+0.02 –0.2	+0.03 –0.2	+0.04 –0.2	+0.06 –0.3
$\alpha_s$ uncertainty	0.04	0.04	0.04	0.04	0.04	0.04	0.04	0.04	0.04	0.04	0.04
Non-perturbative correction uncertainty	0.05	0.05	0.05	0.05	0.05	0.05	0.05	0.05	0.05	0.05	0.05
Total theory uncertainty	+0.08 –0.1	+0.08 –0.1	+0.08 –0.1	+0.08 –0.1	+0.08 –0.1	+0.08 –0.2	+0.08 –0.2	+0.08 –0.2	+0.08 –0.2	+0.09 –0.3	+0.1 –0.3



**Table 20** Measured dijet double-differential cross section per GeV and per unit  $\chi$  as a function of the dijet angular variable  $\chi$  for anti- $k_r$  jets with  $R = 0.6$ , compared to NLO pQCD calculations corrected for non-perturbative effects. All uncertainties listed are fractional uncertainties. There is an additional overall uncertainty of 11% due to the measurement of the integrated luminosity which is not included in the systematic uncertainties given above. The statistical uncertainty is calculated as  $1/\sqrt{N}$ , where  $N$  is the number of events in a given bin

	340 < $m_{12}$ < 520 GeV										
$\chi$	1-1.3	1.3-1.8	1.8-2.4	2.4-3.3	3.3-4.5	4.5-6	6-8.2	8.2-11	11-15	15-20	20-30
Measured cross section [pb/GeV]	28	31	19	20	20	21	24	21	25	24	28
NLO pQCD (CTEQ 6.6) $\times$ non-pert. corr. [pb/GeV]	30	25	22	21	21	21	21	23	23	24	25
Non-perturbative correction	1.0	1.0	1.0	1.0	1.0	1.0	1.0	1.1	1.1	1.1	1.1
Statistical uncertainty	0.20	0.15	0.17	0.13	0.12	0.10	0.079	0.075	0.058	0.052	0.035
Absolute JES uncertainty	+0.32 -0.26	+0.30 -0.26	+0.33 -0.25	+0.31 -0.26	+0.33 -0.24	+0.29 -0.25	+0.30 -0.25	+0.32 -0.29	+0.35 -0.27	+0.33 -0.29	+0.44 -0.28
Relative JES uncertainty	0.027	+0.026 -0.024	+0.031 -0.023	+0.032 -0.034	+0.036 -0.034	+0.037 -0.038	+0.046 -0.048	+0.056 -0.062	+0.065 -0.072	+0.064 -0.069	+0.097 -0.076
Unfolding uncertainty	0.1	0.1	0.1	0.1	0.1	0.1	0.1	0.1	0.1	0.1	0.1
Total systematic uncertainty	0.3	0.3	0.3	0.3	0.3	0.3	0.3	0.3	+0.4 -0.3	+0.4 -0.3	+0.5 -0.3
PDF uncertainty	0.02	0.02	0.02	0.02	0.02	0.02	0.02	0.02	0.02	0.02	0.02
Scale uncertainty	+0.004 -0.04	+0.005 -0.04	+0.005 -0.04	+0.005 -0.04	+0.005 -0.04	+0.006 -0.05	+0.007 -0.06	+0.008 -0.07	+0.009 -0.08	+0.009 -0.09	+0.009 -0.09
$\alpha_s$ uncertainty	0.03	0.03	0.03	0.03	0.03	0.03	0.03	0.03	0.03	0.03	0.03
Non-perturbative correction uncertainty	0.05	0.05	0.05	0.05	0.05	0.05	0.05	0.05	0.05	0.05	0.05
Total theory uncertainty	+0.06 -0.08	+0.06 -0.07	+0.06 -0.07	+0.06 -0.07	+0.06 -0.08	+0.06 -0.08	+0.06 -0.09	+0.06 -0.09	+0.06 -0.1	+0.06 -0.1	+0.06 -0.1

**Table 21** Measured dijet double-differential cross section per GeV and per unit  $\chi$  as a function of the dijet angular variable  $\chi$  for anti- $k_t$  jets with  $R = 0.6$ , compared to NLO pQCD calculations corrected for non-perturbative effects. All uncertainties listed are fractional uncertainties. There is an additional overall uncertainty of 11% due to the measurement of the integrated luminosity which is not included in the systematic uncertainties given above. The statistical uncertainty is calculated as  $1/\sqrt{N}$ , where  $N$  is the number of events in a given bin

	1-1.3	1.3-1.8	1.8-2.4	2.4-3.3	3.3-4.5	4.5-6	6-8.2	8.2-11	11-15	15-20	20-30
$\chi$											
Measured cross section [pb/GeV]	4.3	1.7	1.8	1.4	2.0	0.99	2.3	3.0	2.3	2.6	2.2
NLO pQCD (CTEQ 6.6) $\times$ non-pert. corr. [pb/GeV]	2.9	2.4	2.1	2.0	2.0	2.1	2.1	2.2	2.3	2.4	2.4
Non-perturbative correction	1.0	1.0	1.0	1.0	1.0	1.0	1.0	1.0	1.1	1.0	1.1
Statistical uncertainty	0.41	0.50	0.45	0.41	0.30	0.38	0.21	0.16	0.15	0.13	0.10
Absolute JES uncertainty	+0.30 -0.25	+0.33 -0.25	+0.31 -0.24	+0.33 -0.25	+0.31 -0.25	+0.35 -0.27	+0.33 -0.27	+0.36 -0.26	+0.33 -0.27	+0.36 -0.27	+0.36 -0.27
Relative JES uncertainty	+0.016 -0.021	+0.025 -0.031	+0.025 -0.026	+0.029 -0.036	+0.034 -0.040	+0.050 -0.040	+0.057 -0.051	+0.070 -0.055	+0.070 -0.058	+0.074 -0.085	+0.088 -0.072
Unfolding uncertainty	0.1	0.1	0.1	0.1	0.1	0.1	0.1	0.1	0.1	0.1	0.1
Total systematic uncertainty	0.3	0.3	0.3	0.3	0.3	+0.4 -0.3	+0.4 -0.3	+0.4 -0.3	+0.4 -0.3	+0.4 -0.3	+0.4 -0.3
PDF uncertainty	0.03	0.03	0.03	0.03	0.03	0.03	0.03	0.03	0.03	0.03	0.03
Scale uncertainty	+0.004 -0.05	+0.004 -0.05	+0.004 -0.05	+0.003 -0.05	+0.002 -0.04	+0.002 -0.05	+0.003 -0.06	+0.005 -0.07	+0.007 -0.09	+0.01 -0.1	+0.01 -0.1
$\alpha_s$ uncertainty	0.04	0.04	0.04	0.04	0.04	0.04	0.04	0.04	0.04	0.04	0.04
Non-perturbative correction uncertainty	0.05	0.05	0.05	0.05	0.05	0.05	0.05	0.05	0.05	0.05	0.05
Total theory uncertainty	+0.07 -0.08	+0.07 -0.08	+0.07 -0.08	+0.07 -0.08	+0.07 -0.08	+0.07 -0.08	+0.07 -0.09	+0.07 -0.1	+0.07 -0.1	+0.07 -0.1	+0.07 -0.2

**Table 22** Measured dijet double-differential cross section per GeV and per unit  $\chi$  as a function of the dijet angular variable  $\chi$  for anti- $t_t$  jets with  $R = 0.6$ , compared to NLO pQCD calculations corrected for non-perturbative effects. All uncertainties listed are fractional uncertainties. There is an additional overall uncertainty of 11% due to the measurement of the integrated luminosity which is not included in the systematic uncertainties given above. The statistical uncertainty is calculated as  $1/\sqrt{N}$ , where  $N$  is the number of events in a given bin

$\chi$	1–1.3	1.3–1.8	1.8–2.4	2.4–3.3	3.3–4.5	4.5–6	6–8.2	8.2–11	11–15	15–20	20–30
Measured cross section [pb/GeV]	0.50	0.61	0.74	0.17	–	0.099	0.21	0.16	0.19	0.061	0.11
NLO pQCD (CTEQ 6.6) $\times$ non-pert. corr. [pb/GeV]	0.24	0.20	0.18	0.17	0.17	0.17	0.18	0.19	0.19	0.20	0.21
Non-perturbative correction	1.0	1.0	1.0	1.0	1.0	1.0	1.0	1.0	1.0	1.0	1.0
Statistical uncertainty	1.0	0.71	0.58	1.0	–	1.0	0.58	0.58	0.45	0.71	0.38
Absolute JES uncertainty	+0.33 –0.26	+0.33 –0.28	+0.35 –0.26	+0.33 –0.28	–	+0.35 –0.27	+0.34 –0.27	+0.32 –0.27	+0.39 –0.29	+0.35 –0.32	+0.41 –0.30
Relative JES uncertainty	+0.028 –0.032	+0.029 –0.033	+0.041 –0.035	+0.032 –0.033	–	+0.046 –0.049	+0.064 –0.052	+0.062 –0.070	+0.081 –0.068	+0.083 –0.087	+0.096 –0.083
Unfolding uncertainty	0.1	0.1	0.1	0.1	–	0.1	0.1	0.1	0.1	0.1	0.1
Total systematic uncertainty	0.3	0.3	+0.4 –0.3	0.3	–	+0.4 –0.3	+0.4 –0.3	0.3	+0.4 –0.3	+0.4 –0.3	+0.4 –0.3
PDF uncertainty	+0.05 –0.04	+0.05 –0.04	+0.05 –0.04	+0.05 –0.04	+0.05	+0.05 –0.04	+0.05 –0.04	+0.05 –0.04	+0.05 –0.04	+0.05 –0.04	+0.05 –0.04
Scale uncertainty	+0.008 –0.006	+0.009 –0.006	+0.007 –0.006	+0.006 –0.006	+0.005 –0.005	+0.003 –0.005	+0.002 –0.006	+0.0005 –0.007	+0.004 –0.009	+0.0005 –0.009	+0.01 –0.02
$\alpha_s$ uncertainty	0.04	0.04	0.04	0.04	0.04	0.04	0.04	0.04	0.04	0.04	0.04
Non-perturbative correction uncertainty	0.05	0.05	0.05	0.05	0.05	0.05	0.05	0.05	0.05	0.05	0.05
Total theory uncertainty	+0.08 –0.1	+0.08 –0.1	+0.08 –0.1	+0.08 –0.1	+0.08 –0.09	+0.08 –0.09	+0.08 –0.09	+0.08 –0.1	+0.08 –0.1	+0.08 –0.1	+0.08 –0.2

**Open Access** This article is distributed under the terms of the Creative Commons Attribution Noncommercial License which permits any noncommercial use, distribution, and reproduction in any medium, provided the original author(s) and source are credited.

## References

- G. Aronson et al. (UA1 Collaboration), Angular distributions and structure functions from two jet events at the CERN SPS  $p\bar{p}$  collider. *Phys. Lett. B* **136**, 294 (1984)
- J. Alitti et al. (UA2 Collaboration), Inclusive jet cross-section and a search for quark compositeness at the CERN  $p\bar{p}$  collider. *Phys. Lett. B* **257**, 232–240 (1991)
- B. Adeva et al. (L3 Collaboration), Determination of  $\alpha_s$  from jet multiplicities measured on the Z resonance. *Phys. Lett. B* **248**, 464–472 (1990)
- S. Chekanov et al. (ZEUS Collaboration), Dijet photoproduction at HERA and the structure of the photon. *Eur. Phys. J. C* **23**, 615–631 (2002). [arXiv:hep-ex/0112029](#)
- A. Heister et al. (ALEPH Collaboration), Measurements of the strong coupling constant and the QCD colour factors using four-jet observables from hadronic Z decays. *Eur. Phys. J. C* **27**, 1–17 (2003)
- S. Chekanov et al. (ZEUS Collaboration), Inclusive jet cross sections in the Breit frame in neutral current deep inelastic scattering at HERA and determination of  $\alpha_s$ . *Phys. Lett. B* **547**, 164–180 (2002). [arXiv:hep-ex/0208037](#)
- J. Abdallah et al. (DELPHI Collaboration), Measurement of the energy dependence of hadronic jet rates and the strong coupling  $\alpha_s$  from the four-jet rate with the DELPHI detector at LEP. *Eur. Phys. J. C* **38**, 413–426 (2005). [arXiv:hep-ex/0410071](#)
- G. Abbiendi et al. (OPAL Collaboration), Measurement of the strong coupling  $\alpha_s$  from four-jet observables in  $e^+e^-$  annihilation. *Eur. Phys. J. C* **47**, 295–307 (2006). [arXiv:hep-ex/0601048](#)
- S. Chekanov et al. (ZEUS Collaboration), An NLO QCD analysis of inclusive cross-section and jet-production data from the ZEUS experiment. *Eur. Phys. J. C* **42**, 1–16 (2005). [arXiv:hep-ph/0503274](#)
- A. Abulencia et al. (CDF Collaboration), Measurement of the inclusive jet cross section using the  $k_T$  algorithm in  $p\bar{p}$  collisions at  $\sqrt{s} = 1.96$  TeV with the CDF II detector. *Phys. Rev. D* **75**, 092006 (2007). [hep-ex/0701051](#)
- G. Abbiendi et al. (OPAL Collaboration), Inclusive jet production in photon-photon collisions at  $\sqrt{s_{ee}}$  from 189 to 209 GeV. *Phys. Lett. B* **658**, 185–192 (2008). [arXiv:0706.4382](#) [hep-ex]
- V.M. Abazov et al. (D0 Collaboration), Measurement of the inclusive jet cross-section in  $p\bar{p}$  collisions at  $\sqrt{s} = 1.96$  TeV. *Phys. Rev. Lett.* **101**, 062001 (2008). [arXiv:0802.2400](#) [hep-ex]
- T. Aaltonen et al. (CDF Collaboration), Measurement of the inclusive jet cross section at the Fermilab Tevatron  $p\bar{p}$  collider using a cone-based jet algorithm. *Phys. Rev. D* **78**, 052006 (2008). [arXiv:0807.2204](#) [hep-ex]
- V.M. Abazov et al. (D0 Collaboration), Determination of the strong coupling constant from the inclusive jet cross section in  $p\bar{p}$  collisions at  $\sqrt{s} = 1.96$  TeV. *Phys. Rev. D* **80**, 111107 (2009). [arXiv:0911.2710](#) [hep-ex]
- F.D. Aaron et al. (H1 Collaboration), Jet production in ep collisions at low  $Q^2$  and determination of  $\alpha_s$ . *Eur. Phys. J. C* **67**, 1–24 (2010). [arXiv:0911.5678](#) [hep-ex]
- F.D. Aaron et al. (H1 Collaboration), Jet production in ep collisions at high  $Q^2$  and determination of  $\alpha_s$ . *Eur. Phys. J. C* **65** (2009). [arXiv:0904.3870](#) [hep-ex]. DESY-09-032
- V.M. Abazov et al. (D0 Collaboration), Measurement of dijet angular distributions at  $\sqrt{s} = 1.96$  TeV and searches for quark compositeness and extra spatial dimensions. *Phys. Rev. Lett.* **103**, 191803 (2009). [arXiv:0906.4819](#) [hep-ex]
- H. Abramowicz et al. (ZEUS Collaboration), Inclusive-jet cross sections in NC DIS at HERA and a comparison of the  $k_T$ , anti- $k_T$  and SIScone jet algorithms. *Phys. Lett. B* **691**, 127–137 (2010). [arXiv:1003.2923](#) [hep-ex]
- V.M. Abazov et al. (D0 Collaboration), Measurement of the dijet invariant mass cross section in  $p\bar{p}$  collisions at  $\sqrt{s} = 1.96$  TeV. *Phys. Lett. B* (submitted). [arXiv:1002.4594](#) [hep-ex]
- ATLAS Collaboration, Search for new particles in two-jet final states in 7 TeV proton-proton collisions with the ATLAS detector at the LHC. *Phys. Rev. Lett.* **105**, 161801 (2010). [arXiv:1008.2461](#) [hep-ex]
- ATLAS Collaboration, Search for quark contact interactions in dijet angular distributions in  $pp$  collisions at  $\sqrt{s} = 7$  TeV measured with the ATLAS detector. *Phys. Lett. B* **694**, 327–345 (2011). [arXiv:1009.5069](#) [hep-ex]
- ATLAS Collaboration, The ATLAS experiment at the CERN large hadron collider. *J. Instrum.* **3**, S08003 (2008)
- ATLAS Collaboration, Charged-particle multiplicities in  $pp$  interactions at  $\sqrt{s} = 900$  GeV measured with the ATLAS detector at the LHC. *Phys. Lett. B* **688**, 21–42 (2010). [arXiv:1003.3124](#) [hep-ex]
- M. Cacciari, G. Salam, G. Soyez, The anti- $k_T$  jet clustering algorithm. *J. High Energy Phys.* **0804**, 063 (2008). [arXiv:0802.1189](#)
- M. Cacciari, G.P. Salam, Dispelling the  $N^3$  myth for the  $k_T$  jet-finder. *Phys. Lett. B* **641**, 57–61 (2006). [hep-ph/0512210](#)
- G.P. Salam, M. Cacciari, G. Soyez, <http://www.lpthe.jussieu.fr/~salam/fastjet/>
- C. Buttar et al., Standard model handles and candles working group: tools and jets summary report, [arXiv:0803.0678](#) [hep-ph]
- S. Frixione, G. Ridolfi, Jet photoproduction at HERA. *Nucl. Phys. B* **507**, 315–333 (1997). [arXiv:hep-ph/9707345](#)
- T. Sjöstrand, S. Mrenna, P. Skands, PYTHIA 6.4 physics and manual. *J. High Energy Phys.* **05**, 026 (2006). [hep-ph/0603175](#)
- G. Corcella et al., HERWIG 6.5: An event generator for hadron emission reactions with interfering gluons (including supersymmetric processes). *J. High Energy Phys.* **01**, 010 (2001). [hep-ph/0011363](#)
- J.M. Butterworth, J.R. Forshaw, M.H. Seymour, Multiparton interactions in photoproduction at HERA. *Z. Phys. C* **72**, 637–646 (1996). [arXiv:hep-ph/9601371](#)
- M. Bahr et al., Herwig++ physics and manual. *Eur. Phys. J. C* **58**, 639–707 (2008). [arXiv:0803.0883](#) [hep-ph]
- M.L. Mangano, M. Moretti, F. Piccinini, R. Pittau, A.D. Polosa, ALPGEN, a generator for hard multiparton processes in hadronic collisions. *J. High Energy Phys.* **07**, 001 (2003). [hep-ph/0206293](#)
- T. Gleisberg et al., Event generation with SHERPA 1.1. *J. High Energy Phys.* **02**, 007 (2009). [arXiv:0811.4622](#) [hep-ph]
- A.D. Martin, W.J. Stirling, R.S. Thorne, G. Watt, Parton distributions for the LHC. *Eur. Phys. J. C* **63**, 189–285 (2009). [arXiv:0901.0002](#) [hep-ph]
- A. Sherstnev, R.S. Thorne, Parton distributions for LO generators. *Eur. Phys. J. C* **55**, 553–575 (2008). [arXiv:0711.2473](#) [hep-ph]
- ATLAS Collaboration, ATLAS Monte Carlo tunes for MC09, ATL-PHYS-PUB-2010-002, 2010
- ATLAS Collaboration, The ATLAS simulation infrastructure. *Eur. Phys. J.* **70**, 787 (2010). [arXiv:1005.4568](#)
- S. Agostinelli et al. (GEANT4 Collaboration), GEANT4: a simulation toolkit. *Nucl. Instrum. Methods A* **506**, 250–303 (2003)
- G. Folger, J.P. Wellisch, String parton models in Geant4. [arXiv:nucl-th/0306007](#)
- H. Bertini, Intranuclear cascade calculation of the secondary nucleon spectra from nucleon nucleus interactions in the energy range 340 to 2900 MeV and comparisons with experiment. *Phys. Rev.* **188**, 1711–1730 (1969)
- A. Ribon et al., Status of Geant4 hadronic physics for the simulation of LHC experiments at the LHC physics program. Tech. Rep. CERN-LCGAPP-2010-02, CERN, Geneva, May 2010

43. E. Abat et al., Study of the response of the ATLAS central calorimeter to pions of energies from 3 to 9 GeV. Nucl. Instrum. Methods A **607**, 372–386 (2009)
44. E. Abat et al., Study of energy response and resolution of the ATLAS barrel calorimeter to hadrons of energies from 20 to 350 GeV. Nucl. Instrum. Methods A **621**, 134–150 (2010)
45. J. Pinfold et al., Performance of the ATLAS liquid argon endcap calorimeter in the pseudorapidity region 2.5 to 4.0 in beam tests. Nucl. Instrum. Methods A **593**, 324–342 (2008)
46. D.M. Gingrich et al., Construction, assembly and testing of the ATLAS hadronic end-cap calorimeter. J. Instrum. **2**(05), P05005 (2007)
47. Z. Nagy, Next-to-leading order calculation of three jet observables in hadron hadron collision. Phys. Rev. D **68**, 094002 (2003). [arXiv:hep-ph/0307268](#)
48. W.T. Giele, E.W.N. Glover, D.A. Kosower, Higher order corrections to jet cross-sections in hadron colliders. Nucl. Phys. B **403**, 633–670 (1993). [arXiv:hep-ph/9302225](#)
49. P.M. Nadolsky et al., Implications of CTEQ global analysis for collider observables. Phys. Rev. D **78**, 013004 (2008). [arXiv:0802.0007](#) [hep-ph]
50. R.D. Ball et al. (NNPDF Collaboration), A determination of parton distributions with faithful uncertainty estimation. Nucl. Phys. B **809**, 1–63 (2009). [arXiv:0808.1231](#) [hep-ph]
51. The H1 and ZEUS Collaborations, Combined measurement and QCD analysis of the inclusive  $e^{\pm}p$  scattering cross sections at HERA. J. High Energy Phys. **1001**, 109 (2010). [arXiv:0911.0884](#) [hep-ex]
52. T. Carli et al., A posteriori inclusion of parton density functions in NLO QCD final-state calculations at hadron colliders: the AP-PLGRID project. Eur. Phys. J. C **66**, 503–524 (2010). [arXiv:0911.2985](#) [hep-ph]
53. P.Z. Skands, The Perugia tunes. [arXiv:0905.3418](#) [hep-ph]
54. A. Buckley, H. Hoeth, H. Lacker, H. Schulz, J.E. von Seggern, Systematic event generator tuning for the LHC. Eur. Phys. J. C **65**, 331–357 (2010). [arXiv:0907.2973](#) [hep-ph]
55. A. Buckley et al., Rivet user manual. [arXiv:1003.0694](#) [hep-ph]
56. M. Aharrouche et al. (ATLAS Collaboration), Readiness of the ATLAS liquid argon calorimeter for LHC collisions. [arXiv:0912.2642](#)
57. M. Aharrouche et al., Readiness of the ATLAS tile calorimeter for LHC collisions. [arXiv:1007.5423](#) [physics.ins-det]. ATLAS-TCAL-2010-01-006, CERN-PH-EP-2010-024
58. M. Aharrouche et al., Measurement of the response of the ATLAS liquid argon barrel calorimeter to electrons at the 2004 combined test-beam. Nucl. Instrum. Methods A **614**, 400–432 (2010)
59. ATLAS Collaboration, Performance of the ATLAS detector using first collision data. J. High Energy Phys. **1009**, 056 (2010). [arXiv:1005.5254](#) [hep-ex]
60. M. Aharrouche et al., Time resolution of the ATLAS barrel liquid argon electromagnetic calorimeter. Nucl. Instrum. Methods A **597**, 178–188 (2008)
61. B. Andersson, G. Gustafson, B. Nilsson-Almqvist, A model for low- $p_T$  hadronic reactions with generalizations to hadron-nucleus and nucleus-nucleus collisions. Nucl. Phys. B **281**(1–2), 289–309 (1987)
62. ATLAS Collaboration, Properties of jets and inputs to jet reconstruction and calibration with the ATLAS detector using proton-proton collisions at  $\sqrt{s} = 7$  TeV, ATLAS-CONF-2010-053, 2010
63. ATLAS Collaboration, Luminosity determination in  $pp$  collisions at  $\sqrt{s} = 7$  TeV using the ATLAS detector at the LHC. Eur. Phys. J. C (submitted). [arXiv:1101.2185](#) [hep-ex]

## The ATLAS Collaboration

G. Aad<sup>48</sup>, B. Abbott<sup>111</sup>, J. Abdallah<sup>11</sup>, A.A. Abdelalim<sup>49</sup>, A. Abdesselam<sup>118</sup>, O. Abdinov<sup>10</sup>, B. Abi<sup>112</sup>, M. Abolins<sup>88</sup>, H. Abramowicz<sup>153</sup>, H. Abreu<sup>115</sup>, E. Acerbi<sup>89a,89b</sup>, B.S. Acharya<sup>164a,164b</sup>, M. Ackers<sup>20</sup>, D.L. Adams<sup>24</sup>, T.N. Addy<sup>56</sup>, J. Adelman<sup>175</sup>, M. Aderholz<sup>99</sup>, S. Adomeit<sup>98</sup>, C. Adorisio<sup>36a,36b</sup>, P. Adragna<sup>75</sup>, T. Adye<sup>129</sup>, S. Aefsky<sup>22</sup>, J.A. Aguilar-Saavedra<sup>124b,a</sup>, M. Aharrouche<sup>81</sup>, S.P. Ahlen<sup>21</sup>, F. Ahles<sup>48</sup>, A. Ahmad<sup>148</sup>, H. Ahmed<sup>2</sup>, M. Ahsan<sup>40</sup>, G. Aielli<sup>133a,133b</sup>, T. Akdogan<sup>18a</sup>, T.P.A. Åkesson<sup>79</sup>, G. Akimoto<sup>155</sup>, A.V. Akimov<sup>94</sup>, A. Aktas<sup>48</sup>, M.S. Alam<sup>1</sup>, M.A. Alam<sup>76</sup>, S. Albrand<sup>55</sup>, M. Aleksa<sup>29</sup>, I.N. Aleksandrov<sup>65</sup>, M. Aleppo<sup>89a,89b</sup>, F. Alessandria<sup>89a</sup>, C. Alexa<sup>25a</sup>, G. Alexander<sup>153</sup>, G. Alexandre<sup>49</sup>, T. Alexopoulos<sup>9</sup>, M. Alhroob<sup>20</sup>, M. Aliev<sup>15</sup>, G. Alimonti<sup>89a</sup>, J. Alison<sup>120</sup>, M. Aliyev<sup>10</sup>, P.P. Allport<sup>73</sup>, S.E. Allwood-Spiers<sup>53</sup>, J. Almond<sup>82</sup>, A. Aloisio<sup>102a,102b</sup>, R. Alon<sup>171</sup>, A. Alonso<sup>79</sup>, J. Alonso<sup>14</sup>, M.G. Alvigi<sup>102a,102b</sup>, K. Amako<sup>66</sup>, P. Amaral<sup>29</sup>, G. Ambrosio<sup>89a,b</sup>, C. Amelung<sup>22</sup>, V.V. Ammosov<sup>128</sup>, A. Amorim<sup>124a,c</sup>, G. Amorós<sup>167</sup>, N. Amram<sup>153</sup>, C. Anastopoulos<sup>139</sup>, T. Andeen<sup>34</sup>, C.F. Anders<sup>20</sup>, K.J. Anderson<sup>30</sup>, A. Andreazza<sup>89a,89b</sup>, V. Andrei<sup>58a</sup>, M.-L. Andrieux<sup>55</sup>, X.S. Anduaga<sup>70</sup>, A. Angerami<sup>34</sup>, F. Anghinolfi<sup>29</sup>, N. Anjos<sup>124a</sup>, A. Annovi<sup>47</sup>, A. Antonaki<sup>8</sup>, M. Antonelli<sup>47</sup>, S. Antonelli<sup>19a,19b</sup>, J. Antos<sup>144b</sup>, B. Antunovic<sup>41</sup>, F. Anulli<sup>132a</sup>, S. Aoun<sup>83</sup>, G. Arabidze<sup>8</sup>, I. Aracena<sup>143</sup>, Y. Arai<sup>66</sup>, A.T.H. Arce<sup>44</sup>, J.P. Archambault<sup>28</sup>, S. Arfaoui<sup>29,d</sup>, J.-F. Arguin<sup>14</sup>, T. Argyropoulos<sup>9</sup>, E. Arik<sup>18a,\*</sup>, M. Arik<sup>18a</sup>, A.J. Armbruster<sup>87</sup>, K.E. Arms<sup>109</sup>, S.R. Armstrong<sup>24</sup>, O. Arnaez<sup>4</sup>, C. Arnault<sup>115</sup>, A. Artamonov<sup>95</sup>, D. Arutinov<sup>20</sup>, M. Asai<sup>143</sup>, S. Asai<sup>155</sup>, R. Asfandiyarov<sup>172</sup>, S. Ask<sup>27</sup>, B. Åsman<sup>146a,146b</sup>, D. Asner<sup>28</sup>, L. Asquith<sup>5</sup>, K. Assamagan<sup>24</sup>, A. Astbury<sup>169</sup>, A. Astvatsatourov<sup>52</sup>, G. Atoian<sup>175</sup>, B. Aubert<sup>4</sup>, B. Auerbach<sup>175</sup>, E. Auge<sup>115</sup>, K. Augsten<sup>127</sup>, M. Aurousseau<sup>4</sup>, N. Austin<sup>73</sup>, G. Avolio<sup>163</sup>,

















vic<sup>12a</sup>, V. Vrba<sup>125</sup>, M. Vreeswijk<sup>105</sup>, T.Vu Anh<sup>81</sup>, D. Vudragovic<sup>12a</sup>, R. Vuillermet<sup>29</sup>, I. Vukotic<sup>115</sup>, W. Wagner<sup>174</sup>, P. Wagner<sup>120</sup>, H. Wahlen<sup>174</sup>, J. Walbersloh<sup>42</sup>, J. Walder<sup>71</sup>, R. Walker<sup>98</sup>, W. Walkowiak<sup>141</sup>, R. Wall<sup>175</sup>, P. Waller<sup>73</sup>, C. Wang<sup>44</sup>, H. Wang<sup>172</sup>, J. Wang<sup>32d</sup>, J.C. Wang<sup>138</sup>, S.M. Wang<sup>151</sup>, A. Warburton<sup>85</sup>, C.P. Ward<sup>27</sup>, M. Warsinsky<sup>48</sup>, R. Wastie<sup>118</sup>, P.M. Watkins<sup>17</sup>, A.T. Watson<sup>17</sup>, M.F. Watson<sup>17</sup>, G. Watts<sup>138</sup>, S. Watts<sup>82</sup>, A.T. Waugh<sup>150</sup>, B.M. Waugh<sup>77</sup>, M. Webel<sup>48</sup>, J. Weber<sup>42</sup>, M. Weber<sup>129</sup>, M.S. Weber<sup>16</sup>, P. Weber<sup>54</sup>, A.R. Weidberg<sup>118</sup>, J. Weingarten<sup>54</sup>, C. Weiser<sup>48</sup>, H. Wellenstein<sup>22</sup>, P.S. Wells<sup>29</sup>, M. Wen<sup>47</sup>, T. Wenaus<sup>24</sup>, S. Wendler<sup>123</sup>, Z. Weng<sup>151.at</sup>, T. Wengler<sup>29</sup>, S. Wenig<sup>29</sup>, N. Vermes<sup>20</sup>, M. Werner<sup>48</sup>, P. Werner<sup>29</sup>, M. Werth<sup>163</sup>, U. Werthenbach<sup>141</sup>, M. Wessels<sup>58a</sup>, K. Whalen<sup>28</sup>, S.J. Wheeler-Ellis<sup>163</sup>, S.P. Whitaker<sup>21</sup>, A. White<sup>7</sup>, M.J. White<sup>27</sup>, S. White<sup>24</sup>, S.R. Whitehead<sup>118</sup>, D. Whiteson<sup>163</sup>, D. Whittington<sup>61</sup>, F. Wicke<sup>115</sup>, D. Wicke<sup>81</sup>, F.J. Wickens<sup>129</sup>, W. Wiedenmann<sup>172</sup>, M. Wielers<sup>129</sup>, P. Wienemann<sup>20</sup>, C. Wiglesworth<sup>73</sup>, L.A.M. Wiik<sup>48</sup>, A. Wildauer<sup>167</sup>, M.A. Wildt<sup>41.x</sup>, I. Wilhelm<sup>126</sup>, H.G. Wilkens<sup>29</sup>, J.Z. Will<sup>98</sup>, E. Williams<sup>34</sup>, H.H. Williams<sup>120</sup>, W. Willis<sup>34</sup>, S. Willocq<sup>84</sup>, J.A. Wilson<sup>17</sup>, M.G. Wilson<sup>143</sup>, A. Wilson<sup>87</sup>, I. Wingerter-Seez<sup>4</sup>, S. Winkelmann<sup>48</sup>, F. Winklmeier<sup>29</sup>, M. Wittgen<sup>143</sup>, M.W. Wolter<sup>38</sup>, H. Wolters<sup>124a.i</sup>, B.K. Wosiek<sup>38</sup>, J. Wotschack<sup>29</sup>, M.J. Woudstra<sup>84</sup>, K. Wraight<sup>53</sup>, C. Wright<sup>53</sup>, D. Wright<sup>143</sup>, B. Wrona<sup>73</sup>, S.L. Wu<sup>172</sup>, X. Wu<sup>49</sup>, J. Wuestenfeld<sup>42</sup>, E. Wulf<sup>34</sup>, R. Wunstorff<sup>42</sup>, B.M. Wynne<sup>45</sup>, L. Xaplanteris<sup>9</sup>, S. Xella<sup>35</sup>, S. Xie<sup>48</sup>, Y. Xie<sup>32a</sup>, C. Xu<sup>32b</sup>, D. Xu<sup>139</sup>, G. Xu<sup>32a</sup>, N. Xu<sup>172</sup>, B. Yabsley<sup>150</sup>, M. Yamada<sup>66</sup>, A. Yamamoto<sup>66</sup>, K. Yamamoto<sup>64</sup>, S. Yamamoto<sup>155</sup>, T. Yamamura<sup>155</sup>, J. Yamaoka<sup>44</sup>, T. Yamazaki<sup>155</sup>, Y. Yamazaki<sup>67</sup>, Z. Yan<sup>21</sup>, H. Yang<sup>87</sup>, S. Yang<sup>118</sup>, U.K. Yang<sup>82</sup>, Y. Yang<sup>61</sup>, Y. Yang<sup>32a</sup>, Z. Yang<sup>146a,146b</sup>, S. Yanush<sup>91</sup>, W.-M. Yao<sup>14</sup>, Y. Yao<sup>14</sup>, Y. Yasu<sup>66</sup>, J. Ye<sup>39</sup>, S. Ye<sup>24</sup>, M. Yilmaz<sup>3c</sup>, R. Yoosoo miya<sup>123</sup>, K. Yorita<sup>170</sup>, R. Yoshida<sup>5</sup>, C. Young<sup>143</sup>, S.P. Youssef<sup>21</sup>, D. Yu<sup>24</sup>, J. Yu<sup>7</sup>, J. Yu<sup>32c.au</sup>, J. Yuan<sup>99</sup>, L. Yuan<sup>32a.av</sup>, A. Yurkewicz<sup>148</sup>, V.G. Zaets<sup>128</sup>, R. Zaidan<sup>63</sup>, A.M. Zaitsev<sup>128</sup>, Z. Zajacova<sup>29</sup>, Yo.K. Zalite<sup>121</sup>, V. Zambrano<sup>47</sup>, L. Zanello<sup>132a,132b</sup>, P. Zarzhitsky<sup>39</sup>, A. Zaytsev<sup>107</sup>, M. Zdrzil<sup>14</sup>, C. Zeitnitz<sup>174</sup>, M. Zeller<sup>175</sup>, P.F. Zema<sup>29</sup>, A. Zemla<sup>38</sup>, C. Zender<sup>20</sup>, A.V. Zenin<sup>128</sup>, O. Zenin<sup>128</sup>, T. Zenis<sup>144a</sup>, Z. Zenonos<sup>122a,122b</sup>, S. Zenz<sup>14</sup>, D. Zerwas<sup>115</sup>, G.Zevi della Porta<sup>57</sup>, Z. Zhan<sup>32d</sup>, H. Zhang<sup>83</sup>, J. Zhang<sup>5</sup>, Q. Zhang<sup>5</sup>, X. Zhang<sup>32d</sup>, L. Zhao<sup>108</sup>, T. Zhao<sup>138</sup>, Z. Zhao<sup>32b</sup>, A. Zhemchugov<sup>65</sup>, S. Zheng<sup>32a</sup>, J. Zhong<sup>151.aw</sup>, B. Zhou<sup>87</sup>, N. Zhou<sup>163</sup>, Y. Zhou<sup>151</sup>, C.G. Zhu<sup>32d</sup>, H. Zhu<sup>41</sup>, Y. Zhu<sup>172</sup>, X. Zhuang<sup>98</sup>, V. Zhuravlov<sup>99</sup>, B. Zilka<sup>144a</sup>, R. Zimmermann<sup>20</sup>, S. Zimmermann<sup>20</sup>, S. Zimmermann<sup>48</sup>, M. Ziolkowski<sup>141</sup>, R. Zitoun<sup>4</sup>, L. Živković<sup>34</sup>, V.V. Zmouchko<sup>128.\*</sup>, G. Zobernig<sup>172</sup>, A. Zoccoli<sup>19a,19b</sup>, Y. Zolnierowski<sup>4</sup>, A. Zsenei<sup>29</sup>, M. zur Nedden<sup>15</sup>, V. Zutshi<sup>106</sup>

<sup>1</sup>University at Albany, 1400 Washington Ave, Albany, NY 12222, United States of America

<sup>2</sup>University of Alberta, Department of Physics, Centre for Particle Physics, Edmonton, AB T6G 2G7, Canada

<sup>3</sup>Ankara University<sup>(a)</sup>, Faculty of Sciences, Department of Physics, TR 061000 Tandogan, Ankara; Dumlupinar University<sup>(b)</sup>, Faculty of Arts and Sciences, Department of Physics, Kutahya; Gazi University<sup>(c)</sup>, Faculty of Arts and Sciences, Department of Physics, 06500, Teknikokullar, Ankara; TOBB University of Economics and Technology<sup>(d)</sup>, Faculty of Arts and Sciences, Division of Physics, 06560, Sogutozu, Ankara; Turkish Atomic Energy Authority<sup>(e)</sup>, 06530, Lodumlu, Ankara, Turkey

<sup>4</sup>LAPP, Université de Savoie, CNRS/IN2P3, Annecy-le-Vieux, France

<sup>5</sup>Argonne National Laboratory, High Energy Physics Division, 9700 S. Cass Avenue, Argonne, IL 60439, United States of America

<sup>6</sup>University of Arizona, Department of Physics, Tucson, AZ 85721, United States of America

<sup>7</sup>The University of Texas at Arlington, Department of Physics, Box 19059, Arlington, TX 76019, United States of America

<sup>8</sup>University of Athens, Nuclear & Particle Physics, Department of Physics, Panepistimiopouli, Zografou, GR 15771 Athens, Greece

<sup>9</sup>National Technical University of Athens, Physics Department, 9-Iroon Polytechniou, GR 15780 Zografou, Greece

<sup>10</sup>Institute of Physics, Azerbaijan Academy of Sciences, H. Javid Avenue 33, AZ 143 Baku, Azerbaijan

<sup>11</sup>Institut de Física d'Altes Energies, IFAE, Edifici Cn, Universitat Autònoma de Barcelona, ES - 08193 Bellaterra (Barcelona), Spain

<sup>12</sup>University of Belgrade<sup>(a)</sup>, Institute of Physics, P.O. Box 57, 11001 Belgrade; Vinca Institute of Nuclear Sciences<sup>(b)</sup>, M. Petrovica Alasa 12-14, 11000 Belgrade, Serbia

<sup>13</sup>University of Bergen, Department for Physics and Technology, Allegaten 55, NO - 5007 Bergen, Norway

<sup>14</sup>Lawrence Berkeley National Laboratory and University of California, Physics Division, MS50B-6227, 1 Cyclotron Road, Berkeley, CA 94720, United States of America

<sup>15</sup>Humboldt University, Institute of Physics, Berlin, Newtonstr. 15, D-12489 Berlin, Germany

<sup>16</sup>University of Bern, Albert Einstein Center for Fundamental Physics, Laboratory for High Energy Physics, Sidlerstrasse 5, CH - 3012 Bern, Switzerland

<sup>17</sup>University of Birmingham, School of Physics and Astronomy, Edgbaston, Birmingham B15 2TT, United Kingdom

- <sup>18</sup>Bogazici University<sup>(a)</sup>, Faculty of Sciences, Department of Physics, TR - 80815 Bebek-Istanbul; Dogus University<sup>(b)</sup>, Faculty of Arts and Sciences, Department of Physics, 34722, Kadikoy, Istanbul; <sup>(c)</sup>Gaziantep University, Faculty of Engineering, Department of Physics Engineering, 27310, Sehirkamil, Gaziantep; Istanbul Technical University<sup>(d)</sup>, Faculty of Arts and Sciences, Department of Physics, 34469, Maslak, Istanbul, Turkey
- <sup>19</sup>INFN Sezione di Bologna<sup>(a)</sup>; Università di Bologna, Dipartimento di Fisica<sup>(b)</sup>, viale C. Berti Pichat, 6/2, IT - 40127 Bologna, Italy
- <sup>20</sup>University of Bonn, Physikalisches Institut, Nussallee 12, D - 53115 Bonn, Germany
- <sup>21</sup>Boston University, Department of Physics, 590 Commonwealth Avenue, Boston, MA 02215, United States of America
- <sup>22</sup>Brandeis University, Department of Physics, MS057, 415 South Street, Waltham, MA 02454, United States of America
- <sup>23</sup>Universidade Federal do Rio De Janeiro, COPPE/EE/IF<sup>(a)</sup>, Caixa Postal 68528, Ilha do Fundao, BR - 21945-970 Rio de Janeiro; <sup>(b)</sup>Universidade de Sao Paulo, Instituto de Fisica, R.do Matao Trav. R.187, Sao Paulo - SP, 05508 - 900, Brazil
- <sup>24</sup>Brookhaven National Laboratory, Physics Department, Bldg. 510A, Upton, NY 11973, United States of America
- <sup>25</sup>National Institute of Physics and Nuclear Engineering<sup>(a)</sup>, Str. Atomistilor 407, P.O. Box MG-6, R-077125, Bucharest-Magurele; University Politehnica Bucharest<sup>(b)</sup>, Rectorat - AN 001, 313 Splaiul Independentei, sector 6, 060042 Bucuresti; West University of Timisoara<sup>(c)</sup>, Bd. Vasile Parvan 4, Timisoara, Romania
- <sup>26</sup>Universidad de Buenos Aires, FCEyN, Dto. Fisica, Pab I - C. Universitaria, 1428 Buenos Aires, Argentina
- <sup>27</sup>University of Cambridge, Cavendish Laboratory, J J Thomson Avenue, Cambridge CB3 0HE, United Kingdom
- <sup>28</sup>Carleton University, Department of Physics, 1125 Colonel By Drive, Ottawa ON K1S 5B6, Canada
- <sup>29</sup>CERN, CH - 1211 Geneva 23, Switzerland
- <sup>30</sup>University of Chicago, Enrico Fermi Institute, 5640 S. Ellis Avenue, Chicago, IL 60637, United States of America
- <sup>31</sup>Pontificia Universidad Católica de Chile, Facultad de Fisica, Departamento de Fisica<sup>(a)</sup>, Avda. Vicuna Mackenna 4860, San Joaquin, Santiago; Universidad Técnica Federico Santa María, Departamento de Física<sup>(b)</sup>, Avda. España 1680, Casilla 110-V, Valparaíso, Chile
- <sup>32</sup>Institute of High Energy Physics, Chinese Academy of Sciences<sup>(a)</sup>, P.O. Box 918, 19 Yuquan Road, Shijing Shan District, CN - Beijing 100049; University of Science & Technology of China (USTC), Department of Modern Physics<sup>(b)</sup>, Hefei, CN - Anhui 230026; Nanjing University, Department of Physics<sup>(c)</sup>, Nanjing, CN - Jiangsu 210093; Shandong University, High Energy Physics Group<sup>(d)</sup>, Jinan, CN - Shandong 250100, China
- <sup>33</sup>Laboratoire de Physique Corpusculaire, Clermont Université, Université Blaise Pascal, CNRS/IN2P3, FR - 63177 Aubiere Cedex, France
- <sup>34</sup>Columbia University, Nevis Laboratory, 136 So. Broadway, Irvington, NY 10533, United States of America
- <sup>35</sup>University of Copenhagen, Niels Bohr Institute, Blegdamsvej 17, DK - 2100 Kobenhavn 0, Denmark
- <sup>36</sup>INFN Gruppo Collegato di Cosenza<sup>(a)</sup>; Università della Calabria, Dipartimento di Fisica<sup>(b)</sup>, IT-87036 Arcavacata di Rende, Italy
- <sup>37</sup>Faculty of Physics and Applied Computer Science of the AGH-University of Science and Technology, (FPACS, AGH-UST), al. Mickiewicza 30, PL-30059 Cracow, Poland
- <sup>38</sup>The Henryk Niewodniczanski Institute of Nuclear Physics, Polish Academy of Sciences, ul. Radzikowskiego 152, PL - 31342 Krakow, Poland
- <sup>39</sup>Southern Methodist University, Physics Department, 106 Fondren Science Building, Dallas, TX 75275-0175, United States of America
- <sup>40</sup>University of Texas at Dallas, 800 West Campbell Road, Richardson, TX 75080-3021, United States of America
- <sup>41</sup>DESY, Notkestr. 85, D-22603 Hamburg and Platanenallee 6, D-15738 Zeuthen, Germany
- <sup>42</sup>TU Dortmund, Experimentelle Physik IV, DE - 44221 Dortmund, Germany
- <sup>43</sup>Technical University Dresden, Institut für Kern- und Teilchenphysik, Zellescher Weg 19, D-01069 Dresden, Germany
- <sup>44</sup>Duke University, Department of Physics, Durham, NC 27708, United States of America
- <sup>45</sup>University of Edinburgh, School of Physics & Astronomy, James Clerk Maxwell Building, The Kings Buildings, Mayfield Road, Edinburgh EH9 3JZ, United Kingdom
- <sup>46</sup>Fachhochschule Wiener Neustadt; Johannes Gutenbergstrasse 3, AT - 2700 Wiener Neustadt, Austria
- <sup>47</sup>INFN Laboratori Nazionali di Frascati, via Enrico Fermi 40, IT-00044 Frascati, Italy
- <sup>48</sup>Albert-Ludwigs-Universität, Fakultät für Mathematik und Physik, Hermann-Herder Str. 3, D - 79104 Freiburg i.Br., Germany
- <sup>49</sup>Université de Genève, Section de Physique, 24 rue Ernest Ansermet, CH - 1211 Geneve 4, Switzerland
- <sup>50</sup>INFN Sezione di Genova<sup>(a)</sup>; Università di Genova, Dipartimento di Fisica<sup>(b)</sup>, via Dodecaneso 33, IT - 16146 Genova, Italy

- <sup>51</sup>Institute of Physics of the Georgian Academy of Sciences, 6 Tamarashvili St., GE - 380077 Tbilisi; Tbilisi State University, HEP Institute, University St. 9, GE - 380086 Tbilisi, Georgia
- <sup>52</sup>Justus-Liebig-Universität Giessen, II Physikalisches Institut, Heinrich-Buff Ring 16, D-35392 Giessen, Germany
- <sup>53</sup>University of Glasgow, Department of Physics and Astronomy, Glasgow G12 8QQ, United Kingdom
- <sup>54</sup>Georg-August-Universität, II. Physikalisches Institut, Friedrich-Hund Platz 1, D-37077 Göttingen, Germany
- <sup>55</sup>Laboratoire de Physique Subatomique et de Cosmologie, CNRS/IN2P3, Université Joseph Fourier, INPG, 53 avenue des Martyrs, FR - 38026 Grenoble Cedex, France
- <sup>56</sup>Hampton University, Department of Physics, Hampton, VA 23668, United States of America
- <sup>57</sup>Harvard University, Laboratory for Particle Physics and Cosmology, 18 Hammond Street, Cambridge, MA 02138, United States of America
- <sup>58</sup>Ruprecht-Karls-Universität Heidelberg, Kirchhoff-Institut für Physik<sup>(a)</sup>, Im Neuenheimer Feld 227, D-69120 Heidelberg; Physikalisches Institut<sup>(b)</sup>, Philosophenweg 12, D-69120 Heidelberg; ZITI Ruprecht-Karls-Universität Heidelberg<sup>(c)</sup>, Lehrstuhl für Informatik V, B6, 23-29, DE - 68131 Mannheim, Germany
- <sup>59</sup>Hiroshima University, Faculty of Science, 1-3-1 Kagamiyama, Higashihiroshima-shi, JP - 739-8526 Hiroshima, Japan
- <sup>60</sup>Hiroshima Institute of Technology, Faculty of Applied Information Science, 2-1-1 Miyake Saeki-ku, Hiroshima-shi, JP - 731-5193 Hiroshima, Japan
- <sup>61</sup>Indiana University, Department of Physics, Swain Hall West 117, Bloomington, IN 47405-7105, United States of America
- <sup>62</sup>Institut für Astro- und Teilchenphysik, Technikerstrasse 25, A - 6020 Innsbruck, Austria
- <sup>63</sup>University of Iowa, 203 Van Allen Hall, Iowa City, IA 52242-1479, United States of America
- <sup>64</sup>Iowa State University, Department of Physics and Astronomy, Ames High Energy Physics Group, Ames, IA 50011-3160, United States of America
- <sup>65</sup>Joint Institute for Nuclear Research, JINR, Dubna, RU - 141 980 Moscow Region, Russia
- <sup>66</sup>KEK, High Energy Accelerator Research Organization, 1-1 Oho, Tsukuba-shi, Ibaraki-ken 305-0801, Japan
- <sup>67</sup>Kobe University, Graduate School of Science, 1-1 Rokkodai-cho, Nada-ku, JP 657-8501 Kobe, Japan
- <sup>68</sup>Kyoto University, Faculty of Science, Oiwake-cho, Kitashirakawa, Sakyou-ku, Kyoto-shi, JP - 606-8502 Kyoto, Japan
- <sup>69</sup>Kyoto University of Education, 1 Fukakusa, Fujimori, fushimi-ku, Kyoto-shi, JP - 612-8522 Kyoto, Japan
- <sup>70</sup>Universidad Nacional de La Plata, FCE, Departamento de Física, IFLP (CONICET-UNLP), C.C. 67, 1900 La Plata, Argentina
- <sup>71</sup>Lancaster University, Physics Department, Lancaster LA1 4YB, United Kingdom
- <sup>72</sup>INFN Sezione di Lecce<sup>(a)</sup>; Università del Salento, Dipartimento di Fisica<sup>(b)</sup> Via Arnesano, IT - 73100 Lecce, Italy
- <sup>73</sup>University of Liverpool, Oliver Lodge Laboratory, P.O. Box 147, Oxford Street, Liverpool L69 3BX, United Kingdom
- <sup>74</sup>Jožef Stefan Institute and University of Ljubljana, Department of Physics, SI-1000 Ljubljana, Slovenia
- <sup>75</sup>Queen Mary University of London, Department of Physics, Mile End Road, London E1 4NS, United Kingdom
- <sup>76</sup>Royal Holloway, University of London, Department of Physics, Egham Hill, Egham, Surrey TW20 0EX, United Kingdom
- <sup>77</sup>University College London, Department of Physics and Astronomy, Gower Street, London WC1E 6BT, United Kingdom
- <sup>78</sup>Laboratoire de Physique Nucléaire et de Hautes Energies, Université Pierre et Marie Curie (Paris 6), Université Denis Diderot (Paris-7), CNRS/IN2P3, Tour 33, 4 place Jussieu, FR - 75252 Paris Cedex 05, France
- <sup>79</sup>Lunds Universitet, Naturvetenskapliga Fakulteten, Fysiska Institutionen, Box 118, SE - 221 00 Lund, Sweden
- <sup>80</sup>Universidad Autonoma de Madrid, Facultad de Ciencias, Departamento de Física Teorica, ES - 28049 Madrid, Spain
- <sup>81</sup>Universität Mainz, Institut für Physik, Staudinger Weg 7, DE - 55099 Mainz, Germany
- <sup>82</sup>University of Manchester, School of Physics and Astronomy, Manchester M13 9PL, United Kingdom
- <sup>83</sup>CPPM, Aix-Marseille Université, CNRS/IN2P3, Marseille, France
- <sup>84</sup>University of Massachusetts, Department of Physics, 710 North Pleasant Street, Amherst, MA 01003, United States of America
- <sup>85</sup>McGill University, High Energy Physics Group, 3600 University Street, Montreal, Quebec H3A 2T8, Canada
- <sup>86</sup>University of Melbourne, School of Physics, Parkville, Victoria AU - 3010, Australia
- <sup>87</sup>The University of Michigan, Department of Physics, 2477 Randall Laboratory, 500 East University, Ann Arbor, MI 48109-1120, United States of America
- <sup>88</sup>Michigan State University, Department of Physics and Astronomy, High Energy Physics Group, East Lansing, MI 48824-2320, United States of America
- <sup>89</sup>INFN Sezione di Milano<sup>(a)</sup>; Università di Milano, Dipartimento di Fisica<sup>(b)</sup>, via Celoria 16, IT - 20133 Milano, Italy

- <sup>90</sup>B.I. Stepanov Institute of Physics, National Academy of Sciences of Belarus, Independence Avenue 68, Minsk 220072, Republic of Belarus
- <sup>91</sup>National Scientific & Educational Centre for Particle & High Energy Physics, NC PHEP BSU, M. Bogdanovich St. 153, Minsk 220040, Republic of Belarus
- <sup>92</sup>Massachusetts Institute of Technology, Department of Physics, Room 24-516, Cambridge, MA 02139, United States of America
- <sup>93</sup>University of Montreal, Group of Particle Physics, C.P. 6128, Succursale Centre-Ville, Montreal, Quebec, H3C 3J7, Canada
- <sup>94</sup>P.N. Lebedev Institute of Physics, Academy of Sciences, Leninsky pr. 53, RU - 117 924 Moscow, Russia
- <sup>95</sup>Institute for Theoretical and Experimental Physics (ITEP), B. Cheremushkinskaya ul. 25, RU 117 218 Moscow, Russia
- <sup>96</sup>Moscow Engineering & Physics Institute (MEPhI), Kashirskoe Shosse 31, RU - 115409 Moscow, Russia
- <sup>97</sup>Lomonosov Moscow State University Skobeltsyn Institute of Nuclear Physics (MSU SINP), 1(2), Leninskie gory, GSP-1, Moscow 119991, Russia
- <sup>98</sup>Ludwig-Maximilians-Universität München, Fakultät für Physik, Am Coulombwall 1, DE - 85748 Garching, Germany
- <sup>99</sup>Max-Planck-Institut für Physik, Werner-Heisenberg-Institut, Föhringer Ring 6, 80805 München, Germany
- <sup>100</sup>Nagasaki Institute of Applied Science, 536 Aba-machi, JP 851-0193 Nagasaki, Japan
- <sup>101</sup>Nagoya University, Graduate School of Science, Furo-Cho, Chikusa-ku, Nagoya, 464-8602, Japan
- <sup>102</sup>INFN Sezione di Napoli<sup>(a)</sup>; Università di Napoli, Dipartimento di Scienze Fisiche<sup>(b)</sup>, Complesso Universitario di Monte Sant'Angelo, via Cinthia, IT - 80126 Napoli, Italy
- <sup>103</sup>University of New Mexico, Department of Physics and Astronomy, MSC07 4220, Albuquerque, NM 87131, United States of America
- <sup>104</sup>Radboud University Nijmegen/NIKHEF, Department of Experimental High Energy Physics, Heyendaalseweg 135, NL-6525 AJ, Nijmegen, Netherlands
- <sup>105</sup>Nikhef National Institute for Subatomic Physics and University of Amsterdam, Science Park 105, 1098 XG Amsterdam, Netherlands
- <sup>106</sup>Department of Physics, Northern Illinois University, LaTourette Hall Normal Road, DeKalb, IL 60115, United States of America
- <sup>107</sup>Budker Institute of Nuclear Physics (BINP), RU - 630 090 Novosibirsk, Russia
- <sup>108</sup>New York University, Department of Physics, 4 Washington Place, New York, NY 10003, United States of America
- <sup>109</sup>Ohio State University, 191 West Woodruff Ave, Columbus, OH 43210-1117, United States of America
- <sup>110</sup>Okayama University, Faculty of Science, Tsushima-naka 3-1-1, Okayama 700-8530, Japan
- <sup>111</sup>University of Oklahoma, Homer L. Dodge Department of Physics and Astronomy, 440 West Brooks, Room 100, Norman, OK 73019-0225, United States of America
- <sup>112</sup>Oklahoma State University, Department of Physics, 145 Physical Sciences Building, Stillwater, OK 74078-3072, United States of America
- <sup>113</sup>Palacký University, 17.listopadu 50a, 772 07 Olomouc, Czech Republic
- <sup>114</sup>University of Oregon, Center for High Energy Physics, Eugene, OR 97403-1274, United States of America
- <sup>115</sup>LAL, Univ. Paris-Sud, IN2P3/CNRS, Orsay, France
- <sup>116</sup>Osaka University, Graduate School of Science, Machikaneyama-machi 1-1, Toyonaka, Osaka 560-0043, Japan
- <sup>117</sup>University of Oslo, Department of Physics, P.O. Box 1048, Blindern, NO - 0316 Oslo 3, Norway
- <sup>118</sup>Oxford University, Department of Physics, Denys Wilkinson Building, Keble Road, Oxford OX1 3RH, United Kingdom
- <sup>119</sup>INFN Sezione di Pavia<sup>(a)</sup>; Università di Pavia, Dipartimento di Fisica Nucleare e Teorica<sup>(b)</sup>, Via Bassi 6, IT-27100 Pavia, Italy
- <sup>120</sup>University of Pennsylvania, Department of Physics, High Energy Physics Group, 209 S. 33rd Street, Philadelphia, PA 19104, United States of America
- <sup>121</sup>Petersburg Nuclear Physics Institute, RU - 188 300 Gatchina, Russia
- <sup>122</sup>INFN Sezione di Pisa<sup>(a)</sup>; Università di Pisa, Dipartimento di Fisica E. Fermi<sup>(b)</sup>, Largo B. Pontecorvo 3, IT - 56127 Pisa, Italy
- <sup>123</sup>University of Pittsburgh, Department of Physics and Astronomy, 3941 O'Hara Street, Pittsburgh, PA 15260, United States of America
- <sup>124</sup>Laboratorio de Instrumentacao e Fisica Experimental de Particulas - LIP<sup>(a)</sup>, Avenida Elias Garcia 14-1, PT - 1000-149 Lisboa, Portugal; Universidad de Granada, Departamento de Fisica Teorica y del Cosmos and CAFPE<sup>(b)</sup>, E-18071 Granada, Spain



- <sup>125</sup>Institute of Physics, Academy of Sciences of the Czech Republic, Na Slovance 2, CZ - 18221 Praha 8, Czech Republic
- <sup>126</sup>Charles University in Prague, Faculty of Mathematics and Physics, Institute of Particle and Nuclear Physics, V Holesovickach 2, CZ - 18000 Praha 8, Czech Republic
- <sup>127</sup>Czech Technical University in Prague, Zikova 4, CZ - 166 35 Praha 6, Czech Republic
- <sup>128</sup>State Research Center Institute for High Energy Physics, Moscow Region, 142281, Protvino, Pobeda street, 1, Russia
- <sup>129</sup>Rutherford Appleton Laboratory, Science and Technology Facilities Council, Harwell Science and Innovation Campus, Didcot OX11 0QX, United Kingdom
- <sup>130</sup>University of Regina, Physics Department, Regina, Canada
- <sup>131</sup>Ritsumeikan University, Noji Higashi 1 chome 1-1, JP - 525-8577 Kusatsu, Shiga, Japan
- <sup>132</sup>INFN Sezione di Roma I<sup>(a)</sup>; Università La Sapienza, Dipartimento di Fisica<sup>(b)</sup>, Piazzale A. Moro 2, IT- 00185 Roma, Italy
- <sup>133</sup>INFN Sezione di Roma Tor Vergata<sup>(a)</sup>; Università di Roma Tor Vergata, Dipartimento di Fisica<sup>(b)</sup>, via della Ricerca Scientifica, IT-00133 Roma, Italy
- <sup>134</sup>INFN Sezione di Roma Tre<sup>(a)</sup>; Università Roma Tre, Dipartimento di Fisica<sup>(b)</sup>, via della Vasca Navale 84, IT-00146 Roma, Italy
- <sup>135</sup>Réseau Universitaire de Physique des Hautes Energies (RUPHE): Université Hassan II, Faculté des Sciences Ain Chock<sup>(a)</sup>, B.P. 5366, MA - Casablanca; Centre National de l'Energie des Sciences Techniques Nucleaires (CNESTEN)<sup>(b)</sup>, B.P. 1382 R.P. 10001 Rabat 10001; Université Mohamed Premier<sup>(c)</sup>, LPTPM, Faculté des Sciences, B.P.717. Bd. Mohamed VI, 60000, Oujda; Université Mohammed V, Faculté des Sciences<sup>(d)</sup>, 4 Avenue Ibn Battouta, BP 1014 RP, 10000 Rabat, Morocco
- <sup>136</sup>CEA, DSM/IRFU, Centre d'Etudes de Saclay, FR - 91191 Gif-sur-Yvette, France
- <sup>137</sup>University of California Santa Cruz, Santa Cruz Institute for Particle Physics (SCIPP), Santa Cruz, CA 95064, United States of America
- <sup>138</sup>University of Washington, Seattle, Department of Physics, Box 351560, Seattle, WA 98195-1560, United States of America
- <sup>139</sup>University of Sheffield, Department of Physics & Astronomy, Hounsfield Road, Sheffield S3 7RH, United Kingdom
- <sup>140</sup>Shinshu University, Department of Physics, Faculty of Science, 3-1-1 Asahi, Matsumoto-shi, JP - 390-8621 Nagano, Japan
- <sup>141</sup>Universität Siegen, Fachbereich Physik, D 57068 Siegen, Germany
- <sup>142</sup>Simon Fraser University, Department of Physics, 8888 University Drive, Burnaby, BC V5A 1S6, Canada
- <sup>143</sup>SLAC National Accelerator Laboratory, Stanford, California 94309, United States of America
- <sup>144</sup>Comenius University, Faculty of Mathematics, Physics & Informatics<sup>(a)</sup>, Mlynska dolina F2, SK - 84248 Bratislava; Institute of Experimental Physics of the Slovak Academy of Sciences, Dept. of Subnuclear Physics<sup>(b)</sup>, Watsonova 47, SK - 04353 Kosice, Slovak Republic
- <sup>145</sup><sup>(a)</sup>University of Johannesburg, Department of Physics, PO Box 524, Auckland Park, Johannesburg 2006; <sup>(b)</sup>School of Physics, University of the Witwatersrand, Private Bag 3, Wits 2050, Johannesburg, South Africa
- <sup>146</sup>Stockholm University, Department of Physics<sup>(a)</sup>; The Oskar Klein Centre<sup>(b)</sup>, AlbaNova, SE - 106 91 Stockholm, Sweden
- <sup>147</sup>Royal Institute of Technology (KTH), Physics Department, SE - 106 91 Stockholm, Sweden
- <sup>148</sup>Stony Brook University, Department of Physics and Astronomy, Nicolls Road, Stony Brook, NY 11794-3800, United States of America
- <sup>149</sup>University of Sussex, Department of Physics and Astronomy Pevensey, 2 Building, Falmer, Brighton BN1 9QH, United Kingdom
- <sup>150</sup>University of Sydney, School of Physics, AU - 2006 Sydney NSW, Australia
- <sup>151</sup>Institute of Physics, Academia Sinica, TW - 11529 Taipei, Taiwan
- <sup>152</sup>Technion, Israel Inst. of Technology, Department of Physics, Technion City, IL - 32000 Haifa, Israel
- <sup>153</sup>Tel Aviv University, Raymond and Beverly Sackler School of Physics and Astronomy, Ramat Aviv, IL - 69978 Tel Aviv, Israel
- <sup>154</sup>Aristotle University of Thessaloniki, Faculty of Science, Department of Physics, Division of Nuclear & Particle Physics, University Campus, GR - 54124, Thessaloniki, Greece
- <sup>155</sup>The University of Tokyo, International Center for Elementary Particle Physics and Department of Physics, 7-3-1 Hongo, Bunkyo-ku, JP - 113-0033 Tokyo, Japan
- <sup>156</sup>Tokyo Metropolitan University, Graduate School of Science and Technology, 1-1 Minami-Osawa, Hachioji, Tokyo 192-0397, Japan

- <sup>157</sup>Tokyo Institute of Technology, 2-12-1-H-34 O-Okayama, Meguro, Tokyo 152-8551, Japan
- <sup>158</sup>University of Toronto, Department of Physics, 60 Saint George Street, Toronto M5S 1A7, Ontario, Canada
- <sup>159</sup>TRIUMF<sup>(a)</sup>, 4004 Wesbrook Mall, Vancouver, B.C. V6T 2A3; <sup>(b)</sup>York University, Department of Physics and Astronomy, 4700 Keele St., Toronto, Ontario, M3J 1P3, Canada
- <sup>160</sup>University of Tsukuba, Institute of Pure and Applied Sciences, 1-1-1 Tennoudai, Tsukuba-shi, JP - 305-8571 Ibaraki, Japan
- <sup>161</sup>Tufts University, Science & Technology Center, 4 Colby Street, Medford, MA 02155, United States of America
- <sup>162</sup>Universidad Antonio Narino, Centro de Investigaciones, Cra 3 Este No.47A-15, Bogota, Colombia
- <sup>163</sup>University of California, Department of Physics & Astronomy, Irvine, CA 92697-4575, United States of America
- <sup>164</sup>INFN Gruppo Collegato di Udine<sup>(a)</sup>, IT - 33100 Udine; ICTP<sup>(b)</sup>, Strada Costiera 11, IT-34014, Trieste; Università di Udine, Dipartimento di Fisica<sup>(c)</sup>, via delle Scienze 208, IT - 33100 Udine, Italy
- <sup>165</sup>University of Illinois, Department of Physics, 1110 West Green Street, Urbana, Illinois 61801, United States of America
- <sup>166</sup>University of Uppsala, Department of Physics and Astronomy, P.O. Box 516, SE -751 20 Uppsala, Sweden
- <sup>167</sup>Instituto de Física Corpuscular (IFIC) Centro Mixto UVEG-CSIC, Apdo. 22085 ES-46071 Valencia, Dept. Física At. Mol. y Nuclear; Dept. Ing. Electrónica; Univ. of Valencia, and Inst. de Microelectrónica de Barcelona (IMB-CNM-CSIC), 08193 Bellaterra, Spain
- <sup>168</sup>University of British Columbia, Department of Physics, 6224 Agricultural Road, Vancouver, B.C. V6T 1Z1, Canada
- <sup>169</sup>University of Victoria, Department of Physics and Astronomy, P.O. Box 3055, Victoria B.C., V8W 3P6, Canada
- <sup>170</sup>Waseda University, WISE, 3-4-1 Okubo, Shinjuku-ku, Tokyo, 169-8555, Japan
- <sup>171</sup>The Weizmann Institute of Science, Department of Particle Physics, P.O. Box 26, IL - 76100 Rehovot, Israel
- <sup>172</sup>University of Wisconsin, Department of Physics, 1150 University Avenue, Madison, WI 53706, United States of America
- <sup>173</sup>Julius-Maximilians-University of Würzburg, Physikalisches Institute, Am Hubland, 97074 Würzburg, Germany
- <sup>174</sup>Bergische Universität, Fachbereich C, Physik, Postfach 100127, Gauss-Strasse 20, D- 42097 Wuppertal, Germany
- <sup>175</sup>Yale University, Department of Physics, PO Box 208121, New Haven, CT, 06520-8121, United States of America
- <sup>176</sup>Yerevan Physics Institute, Alikhanian Brothers Street 2, AM - 375036 Yerevan, Armenia
- <sup>177</sup>ATLAS-Canada Tier-1 Data Centre, TRIUMF, 4004 Wesbrook Mall, Vancouver, BC, V6T 2A3, Canada
- <sup>178</sup>GridKA Tier-1 FZK, Forschungszentrum Karlsruhe GmbH, Steinbuch Centre for Computing (SCC), Hermann-von-Helmholtz-Platz 1, 76344 Eggenstein-Leopoldshafen, Germany
- <sup>179</sup>Port d'Informació Científica (PIC), Universitat Autònoma de Barcelona (UAB), Edifici D, E-08193 Bellaterra, Spain
- <sup>180</sup>Centre de Calcul CNRS/IN2P3, Domaine scientifique de la Doua, 27 bd du 11 Novembre 1918, 69622 Villeurbanne Cedex, France
- <sup>181</sup>INFN-CNAF, Viale Berti Pichat 6/2, 40127 Bologna, Italy
- <sup>182</sup>Nordic Data Grid Facility, NORDUnet A/S, Kastruplundgade 22, 1, DK-2770 Kastrup, Denmark
- <sup>183</sup>SARA Reken- en Netwerkdiensten, Science Park 121, 1098 XG Amsterdam, Netherlands
- <sup>184</sup>Academia Sinica Grid Computing, Institute of Physics, Academia Sinica, No.128, Sec. 2, Academia Rd., Nankang, Taipei, Taiwan 11529, Taiwan
- <sup>185</sup>UK-T1-RAL Tier-1, Rutherford Appleton Laboratory, Science and Technology Facilities Council, Harwell Science and Innovation Campus, Didcot OX11 0QX, United Kingdom
- <sup>186</sup>RHIC and ATLAS Computing Facility, Physics Department, Building 510, Brookhaven National Laboratory, Upton, New York 11973, United States of America
- <sup>a</sup>Also at LIP, Portugal
- <sup>b</sup>Present address FermiLab, USA
- <sup>c</sup>Also at Faculdade de Ciências, Universidade de Lisboa, Portugal
- <sup>d</sup>Also at CPPM, Marseille, France
- <sup>e</sup>Also at TRIUMF, Vancouver, Canada
- <sup>f</sup>Also at FPACS, AGH-UST, Cracow, Poland
- <sup>g</sup>Now at Università dell'Insubria, Dipartimento di Fisica e Matematica
- <sup>h</sup>Also at TRIUMF, Vancouver, Canada
- <sup>i</sup>Also at Department of Physics, University of Coimbra, Portugal
- <sup>j</sup>Now at CERN
- <sup>k</sup>Also at Università di Napoli Parthenope, Napoli, Italy
- <sup>l</sup>Also at Institute of Particle Physics (IPP), Canada

- <sup>m</sup>Also at Università di Napoli Parthenope, via A. Acton 38, IT - 80133 Napoli, Italy
- <sup>n</sup>Louisiana Tech University, 305 Wisteria Street, P.O. Box 3178, Ruston, LA 71272, United States of America
- <sup>o</sup>Also at Universidade de Lisboa, Portugal
- <sup>p</sup>At California State University, Fresno, USA
- <sup>q</sup>Also at TRIUMF, 4004 Wesbrook Mall, Vancouver, B.C. V6T 2A3, Canada
- <sup>r</sup>Currently at Istituto Universitario di Studi Superiori IUSS, Pavia, Italy
- <sup>s</sup>Also at Faculdade de Ciências, Universidade de Lisboa, Portugal and at Centro de Física Nuclear da Universidade de Lisboa, Portugal
- <sup>t</sup>Also at FPACS, AGH-UST, Cracow, Poland
- <sup>u</sup>Also at California Institute of Technology, Pasadena, USA
- <sup>v</sup>Louisiana Tech University, Ruston, USA
- <sup>w</sup>Also at University of Montreal, Montreal, Canada
- <sup>x</sup>Also at Institut für Experimentalphysik, Universität Hamburg, Hamburg, Germany
- <sup>y</sup>Now at Chonnam National University, Chonnam, Korea 500-757
- <sup>z</sup>Also at Petersburg Nuclear Physics Institute, Gatchina, Russia
- <sup>aa</sup>Also at Institut für Experimentalphysik, Universität Hamburg, Luruper Chaussee 149, 22761 Hamburg, Germany
- <sup>ab</sup>Also at School of Physics and Engineering, Sun Yat-sen University, China
- <sup>ac</sup>Also at School of Physics, Shandong University, Jinan, China
- <sup>ad</sup>Also at California Institute of Technology, Pasadena, USA
- <sup>ae</sup>Also at Rutherford Appleton Laboratory, Didcot, UK
- <sup>af</sup>Also at school of physics, Shandong University, Jinan
- <sup>ag</sup>Also at Rutherford Appleton Laboratory, Didcot, UK
- <sup>ah</sup>Now at KEK
- <sup>ai</sup>Also at Departamento de Física, Universidade de Minho, Portugal
- <sup>aj</sup>University of South Carolina, Columbia, USA
- <sup>ak</sup>Also at KFKI Research Institute for Particle and Nuclear Physics, Budapest, Hungary
- <sup>al</sup>University of South Carolina, Dept. of Physics and Astronomy, 700 S. Main St, Columbia, SC 29208, United States of America
- <sup>am</sup>Now at TRIUMF, Vancouver, Canada
- <sup>an</sup>Also at Institute of Physics, Jagiellonian University, Cracow, Poland
- <sup>ao</sup>Louisiana Tech University, Ruston, USA
- <sup>ap</sup>Also at Centro de Física Nuclear da Universidade de Lisboa, Portugal
- <sup>aq</sup>Also at School of Physics and Engineering, Sun Yat-sen University, Taiwan
- <sup>ar</sup>University of South Carolina, Columbia, USA
- <sup>as</sup>Also at Oxford University, Department of Physics, Denys Wilkinson Building, Keble Road, Oxford OX1 3RH, United Kingdom
- <sup>at</sup>Also at school of physics and engineering, Sun Yat-sen University
- <sup>au</sup>Also at CEA
- <sup>av</sup>Also at LPNHE, Paris, France
- <sup>aw</sup>Also at Nanjing University, China
- \* Deceased